A Comprehensive Entry, Descent, Landing, and Locomotion (EDLL) Vehicle for Planetary Exploration

Kevin Schroeder

Dissertation submitted to the Faculty of the
Virginia Polytechnic Institute and State University
in partial fulfillment of the requirements for the degree of

Doctor of Philosophy
in
Mechanical Engineering

Javid Bayandor, Chair
Jamshid Samareh
Sasan Armand
Francine Battaglia
Walter O'Brien
Wayne Scales

July 18th, 2017
Blacksburg, Virginia

Keywords: Entry Descent Landing (EDL), Tensegrity, Venus Rover, Deployable Heat Shield

A Comprehensive Entry, Descent, Landing, and Locomotion (EDLL) Vehicle for Planetary Exploration

Kevin Schroeder

Abstract

The 2012 Decadal Survey has stated that there is a critical role for a Venus In-situ Explore (VISE) missions to a variety of important sites, specifically the Tessera terrain. This work aims to answer the Decadal Survey's call by developing a new comprehensive Entry, Descent, Landing, and Locomotion (EDLL) vehicle for in-situ exploration of Venus, especially in the Tessera regions.

TANDEM, the Tension Adjustable Network for Deploying Entry Membrane, is a new planetary probe concept in which all of EDLL is achieved by a single multifunctional tensegrity structure. The concept uses same fundamental concept as the ADEPT (Adaptable Deployable Entry and Placement Technology) deployable heat shield but replaces the standard internal structure with the structure from the tensegrity-actuated rover to provide a combined aeroshell and rover design. The tensegrity system implemented by TANDEM reduces the mass of the overall system while enabling surface locomotion and mitigating risk associated with landing in the rough terrain of Venus's Tessera regions, which is otherwise nearly inaccessible to surface missions.

TANDEM was compared to other state-of-the-art lander designs for an in-situ mission to Venus. It was shown that TANDEM provides the same scientific experimentation capabilities that were proposed for the VITaL mission, with a combined mass reduction for the aeroshell and lander of 52% (1445 *kg*), while eliminating the identified risks associated with entry loads and very rough terrain. Additionally, TANDEM provides locomotion when on the surface as well as a host of other maneuvers during entry and descent, which was not present in the VITaL design. Based on its unique multifunctional infrastructure and excellent crashworthiness for impact on rough surfaces, TANDEM presents a robust system to address some of the Decadal Survey's most pressing questions about Venus.

A Comprehensive Entry, Descent, Landing, and Locomotion (EDLL) Vehicle for Planetary Exploration

Kevin Schroeder

General Audience Abstract

NASA has proposed the possibility of performing a robotic mission to Venus in this upcoming decade. This could be NASA's first attempt to design a robot that is capable of landing on the surface of our solar systems hottest planet. Venus presents a great exploration opportunity, as it is our closest planetary neighbor. Venus is similar to Earth in both size and location in the solar system, yet it is profoundly different in many other aspects regarding habitability. There is a significant scientific interest in exploring the mysteries of the greenhouse gases and runaway climate change present in the Venusian atmosphere. Understanding Venus' atmosphere will help us to increase our knowledge of Earth's atmosphere. Exploring the difference in these two planets will greatly further our intuition of other planetary systems and will aid in our search for life in the universe. Yet, exploring Venus presents a number of severe engineering challenges: the extreme temperature and pressure at the planet's surface, the highly corrosive atmosphere, and lack of terrain resolution caused by the dense permanent cloud layer.

In order to address these engineering challenges, a new ultra-lightweight planetary probe has been invented. TANDEM, the Tension Adjustable Network for Deploying Entry Membrane, is unique in its design as it has combined all of the subsystems in needs to safely land on the surface into a single lightweight, multifunctional structure. This enables the design to be nearly 1.5 metric tons lighter than the same mission that was proposed in 2010 using the current state-of-the-art technologies. Based on this and other unique capabilities that are provided, TANDEM presents a robust system to address some of NASA's most pressing questions about Venus.

Contents of Report

List of Tables

List of Figures

Acknowledgements

I would like to first off thank my wife for supporting me in my studies and for being as enthusiastic about TANDEM as I am. Thank you for sharing in this doctoral experience with me. I'd also like to express my deep gratitude for the guidance and council of Dr. Javid Bayandor and Dr. Jamshid Samareh. You both helped me so much in this work; it would not have been a success without your contributions. Additionally, I would like to thank all of my PhD Committee members. Your advice and feedback is always welcome and has been very valuable to me in this process. I look forward to working with all of you again in the future.

This work was supported by the Vehicle Analysis Branch at NASA Langley as well as by the NASA Innovative Advanced Concepts Program through NASA Headquarters. I'd also like to thank my collaborators that contributed to this body of work. From Virginia Tech: Jeffery Feaster, Christopher Peterson, George Boggs, and Theo Long even though things didn't always pan out, you were a big help and I appreciate it. I'd also like to express my appreciation of NASA Ames' Dynamic Tensegrity Robotics Lab, especially to Dawn Hustig-Schultz and Vytas SunSpiral and for their continued support and enthusiasm for this research.

Finally, I would like to thank all of the members of Virginia Tech's *CRashworthiness for Aerospace Structures and Hybrids Lab* (*CRASH* Lab) for their collaboration, support, and friendship, but specifically Yangkun Song, Jeffrey Feaster, Brandon Horton, and Brittany Gater. You each generously and frequently donated your time when I needed it. Thank you.

Preface

The demand to explore where we have never explored requires the development of new technologies that enable landed science in hard to reach locations. As a result, contemporary Entry, Descent, Landing, (EDL) and additional locomotion (EDLL) profiles are becoming increasingly more complex, with the introduction of lifting/guided entries, hazard avoidance on descent, and a plethora of landing techniques including airbags and the skycrane maneuver. The inclusion of each of these subsystems into a mission profile is associated in many cases with a substantial mass penalty.

The objective of this research was to develop and examine an alternative concept for planetary Entry, Descent, and Landing for future missions to Venus, and compare it to the current state of the art EDL systems. In order to evaluate the merit of the any alternative method, it was decided that a study of previous missions to the Venusian surface as well as contemporary mission concepts should be performed. From this investigation a Baseline mission design should be developed to measure the alternative design against. The Baseline mission discussion was based on work submitted to the Journal of Spacecraft and Rockets [1].

This dissertation explores the new all-in-one entry vehicle concept known as the Tension Adjustable Network for Deploying Entry Membrane (TANDEM). This work was initiated as a phase I NIAC study [2] and was reported in a manuscript submitted the Journal of Spacecraft and Rockets [3]. The proposed system is lightweight and collapsible and provides the capacity for lifting/guided entry, guided descent, hazard avoidance, omnidirectional impact protection and surface locomotion without the aid of any additional subsystems.

To the author's knowledge, TANDEM is the first in a new class of planetary probes, which will be referred to in this dissertation as an EDLL vehicle. The EDLL vehicle is a single comprehensive vehicle that combines the infrastructure used for the EDL as well as on-the-ground Locomotion into a single multifunctional system. Reusing the same active infrastructure for every segment of the mission makes TANDEM an efficient and versatile systems for medium to large size payloads. This efficiency translates directly to longer mission lives, increased scientific payload, and/or a reduction in mission cost and total mass of the whole mission.

TANDEM is a tensegrity rover designed to also be the frame of a deployable heat shield. TANDEM uses the same TPS material as the well-established concept, ADEPT [4–8], but replaces the internal umbrella-style rib structure with an active tensegrity-actuation. This provides the same benefits as ADEPT (i.e. low ballistic coefficient, lower entry g's, smaller launch vehicle (LV), larger payloads, etc.) while seamlessly integrating the multifunctional tensegrity infrastructure. Coupling these two innovative ideas in a single design produces significantly more advantages than either concept has separately.

Tensegrity actuated deployable heat shields have been proposed before [9,10] as have tensegrity lander/rovers [11–13]. But to date no one has presented a unified vehicle where one underlining tensegrity structure is capable of handling all of entry, decent, landing, and locomotion (EDLL). The systems level design approach to the EDLL sequence is what makes TANDEM unique. In most planetary probe concepts, each leg of the sequence is handled by a separate system; the heat shield is unrelated to the landing mechanism and the payload (i.e. the rover or the lander) is typically considered dead mass until it has actually landed on the surface. In TANDEM, everything is connected to an actively controlled tensegrity frame so that the systems used for landing and locomotion are also utilized in entry and descent. This frame brings a new level of controllability to the EDLL sequence without increasing complexity or mass by introducing multiple subsystems for each step in the EDLL sequence. Figure 1 depicts the vehicle in a stowed (a) and deployed (b) configuration.

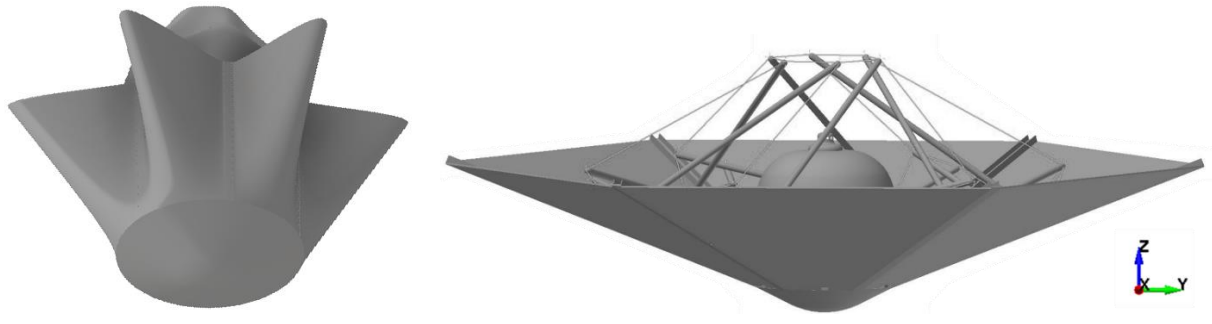

(a) (b)

Figure 1 The TANDEM Concept (a) stowed vehicle with entry membrane and backshell (b) deployed vehicle with the carbon fabric of the backshell hidden

This work will include investigations from each of segment of the EDLL sequence, with a heavier focus applied to the impact analysis and crashworthiness of the vehicle, as that is the mission critical design feature required to perform landed science in the Tessera region. In order to show the merit of the TANDEM concept a direct comparison will be made between it and the heritage design of the Venera Landers. The following summarizes the primary objectives for this research

1. Performed investigation of the mechanical design of the original Venera Landers and provided insight into the design
2. Developed a methodology for the rapid design of a Venera Class Lander for future missions to Venus
3. Explored the capabilities and feasibility of the TANDEM concept as an EDLL vehicle

4. Performed extensive impact analysis to ensure mission success in unfavorable landing conditions (i.e. safe landing in Tessera regions)
5. Developed a detailed design of TANDEM for a conceptual mission to Venus

Dissertation Map

The present dissertation aims to provide an overview of the progress made, results found, and methodologies used in to develop the TANDEM concept. A thorough description of each step in the investigation is presented. The work is organized as follows:

Chapter 1 – Introduction of the fundamental technologies that enable the TANDEM concept or will be used as a benchmark to compare against. Past missions to Venus as well as two proposed mission architectures are discussed. Tensegrity structures are defined and introduced.

Chapter 2 – An up-to-date investigation of the design of the USSR's Venera Landers and the development of a new Baseline Venera Class lander design to compare the newly invented TANDEM concept against

Chapter 3 – An introduction of the fundamentals of the TANDEM concept is provided. The fundamental technologies that are desired for an extended in-situ mission on the surface of Venus.

Chapter 4 – The development of a Systems Analysis Tool for the rapid investigation of the EDLL design space is discussed. An overview of the implementation of a 3-DOF flight mechanics code with incorporated modules for hypersonic aerodynamics, aerothermodynamics, and vehicle configuration control is provided.

Chapter 5 – The development of impact modeling methodology is discussed. A series of physical drop test are described and their results are used to validate the developed modelling methodology. With the model validated a large parametric impact analysis was performed to demonstrate TANDEM's omnidirectional protection.

Chapter 6 – Description of three types of control strategies used and a discussion of the selected methodology for advanced gait development

Chapter 7 – Overview of a detail design of a TANDEM vehicle for a conceptual mission to a Tessera region on Venus is discussed. The detailed design is compare against 3 alternative

designs using the current state of the art technologies to measure the merit of TANDEM as a planetary probe.

Conclusions, Contributions, and Continuing Work

Chapter 1
Introduction and Background

The 2012 decadal survey has listed Venus as a candidate for a New Frontiers missions [14]. This marked a new increase in interest in sending a mission to Venus. Venus presents a great exploration opportunity, as it is our closest planetary neighbor. Venus is similar to Earth in both size and location in the solar system, yet it is profoundly different in many other aspects regarding habitability. The Venusian atmosphere is considerably thicker than that of Earth. While the pressures and temperatures above its dense cloud layers are relatively benign, beneath them the temperatures and pressures begin to spike. In the last 100 km to the surface, the temperatures jump from approximately 100 K to 750 K. At the surface the atmospheric pressure is approximately 92 bars. The extreme temperature raise is caused in part by a phenomena know as runaway green house. There is a significant scientific interest in exploring the mysteries of the greenhouse gases and runaway climate change present in the Venusian atmosphere. Understanding how Venus' atmosphere came to be the way that it is will help us to understand our own atmosphere better. Understanding the difference in these two planets will greatly assist our understanding of other planetary systems and will aid in our search for life in the universe. Figure 2 shows the basic structure of Venus' atmosphere with a temperature versus altitude relationship.

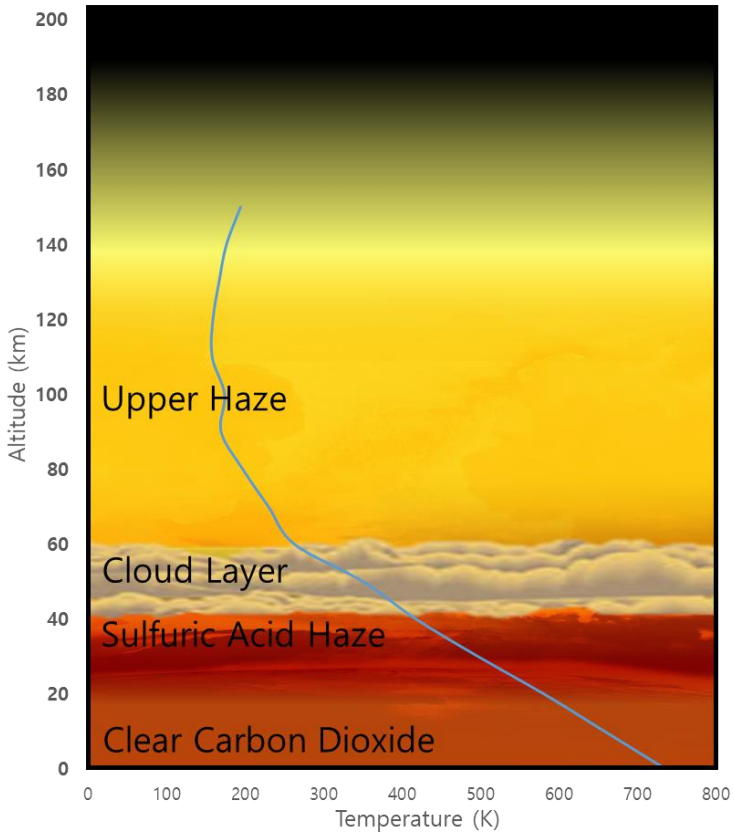

Figure 2 Fundamental atmospheric structure of Venus overlaid with a temperature versus altitude plot

However, Venus' atmosphere also presents a number of severe engineering challenges. The extreme temperature and pressure at the planet's surface drastically complicate the design of a lander as very few electrical and electro-mechanical devices can operate at these conditions. Additionally, the atmosphere of Venus is highly corrosive. On top of the trace elements in the atmosphere, such as SO_2, HF, and HCl, over 96% of the atmosphere near the surface is comprised of supercritical CO_2 which is itself a powerful solvent [15]. Finally, although nearly the whole surface of Venus was mapped in the Magellen mission, the dense permanent cloud layer of Venus has drastically limited the topology resolution. The data from Magellan's Synthetic Aperture Radar (SAR) has a resolution of only 2 km [16]. Despite these challenges the Decadal Survey has stated, "There is a critical future role for additional [Venus In-Situ Explorer type] missions to a variety of important sites, such as Tessera terrain."

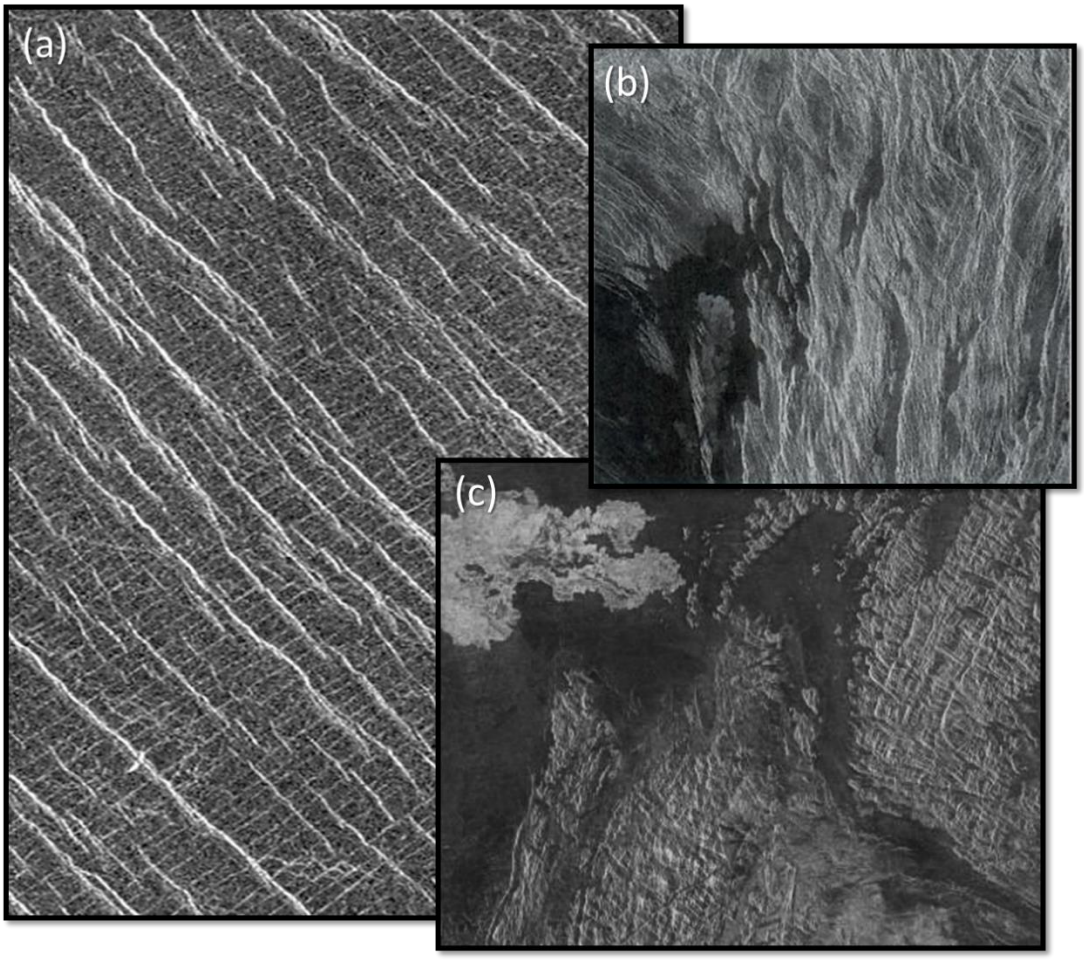

Figure 3 Samples of Venus' Tessera Terrain (a) Lakshmi Region 30°N, 333.3°E [17] **(b) Alpha Regio 25°S, 357°E** [18] **(c) Eistla Regio 1°S, 37°E** [19]

The Tessera regions are an unexplored mountainous regions scattered throughout Venus. The Tessera regions, which comprise approximately 8% of the total surface of the planet, are believed to be the oldest regions on the planet and can provide insight into the first 80% of the planet's history [20]. Due to the current resolution of Venusian maps, it can be hard to predict to the roughness of these landscapes at the meter scale, but on the kilometer scale a clear grid or tiled pattern can be seen. The tiled landscape is seen in its most iconic form in Fig. 3(a), but other Tessera regions exist which are more "chaotic" in shape as seen in in Fig. 3(b) and (c). This tiled patterned is what gave the landscape its name, Tessera, which is also the name of an individual tile of a mosaic.

This work aims to answer the Decadal Survey's call by developing a new comprehensive Entry, Descent, Landing, and Locomotion (EDLL) vehicle for in-situ exploration of Venus, especially in the Tessera regions. A new in-situ explorer would be the first planetary probe designed to preform experiments on the surface of Venus since the Soviet Union's Vega mission 1985 [21]. A brief sampling of the broad scope of these concepts are presented at the start of Chapter 2, while a more in-depth overview of the most applicable architectures will be the focus of the remainder of this chapter.

The Venera Missions

The Soviet Union had 18 mission to take on the title, "Venera" including the two VeGa (Venera & Galileo) missions [22,23]. Despite these significant challenges, the Soviet's Venus campaign, Venera, continued to send probes to Venus [24] (see Fig. 4). In 1970 the Venera 7 became the first spacecraft to successfully land on the surface of Venus [25]. The data from Venera 7 was used to inform a number of improvements made to the probe design for future missions. When the Venera 9 and 10 missions were launched in 1975 and entirely new lander had been designed [26]. Unlike the previous probes from the Venera campaign which were focused on analyzing the atmospheric properties as they descended, the new Venera lander was designed to perform various additional scientific experiment on the surface. Of the 18 Venera missions, Venera 9-14 and VeGa 1 & 2 all used the same basic architecture that was developed for Venera 9 and 10 missions, albeit with some minor alterations.

The probe entered the atmosphere at 10.7 km/s, encapsulated in a 2.4 m spherical heat shield. After a series of parachutes, the lander was extracted from its heat shield and its speed was reduced to below 50 m/s. At this point, the lander and its payload became exposed to ambient condition and although the temperature at this altitude is several hundred degrees less that the temperature at the surface, it was important to get the lander to the surface quickly before the payload was compromised by the high temperatures. A three-domed parachute was deployed to slow the descent through the cloud sheet for atmospheric readings but was released as soon as the lander had fully passed through cloud layer. Because

there was a significant increase of the atmospheric density in the last 50 km to the surface, the lander was able to quickly decelerate in free fall to approximately 7 m/s [27].

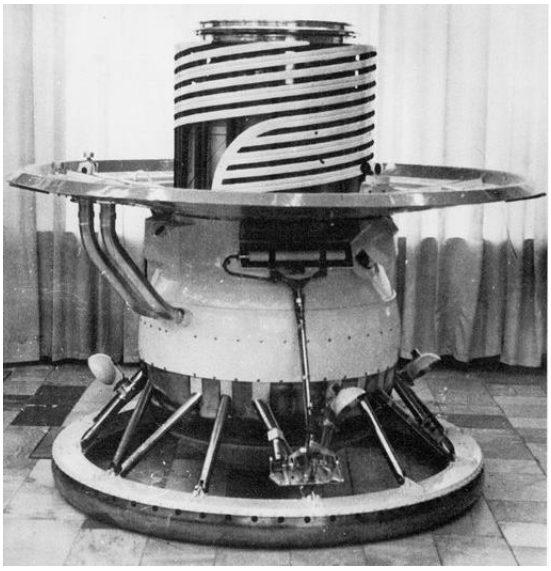

Figure 4 Venera 9 lander [24]

Despite some technical difficulties, the 9 Venera Landers (the in-situ probes from Venera 7-14 and VeGa 1 and 2) were very successful. From this campaign the landers were able to sample and analyze the soil composition, inspect the surface hardness, and photograph the landscape [28–31]. However, due to technology limitations from the 60's 70's and 80's when these missions were flown, the quantity and quality of the data collected leaves many scientific questions unanswered. Additional in-situ missions will be required to provide a more complete understanding Venus and its history.

Venus Intrepid Tessera Lander

The 2012 Decadal Survey had a mission developed by NASA Goddard's Architecture Design Lab (ADL) to show the feasibility of exploring the Tessera Region. This New Frontier's sized mission concept, known as the Venus Intrepid Tessera Lander (VITaL) [20], was designed for a launch in November of 2021. The VITaL is a Venera Class design, meaning that its lander geometry uses the same fundamental design utilized by the latter Venera and VeGa missions. The VITaL design is shown in Fig. 5.

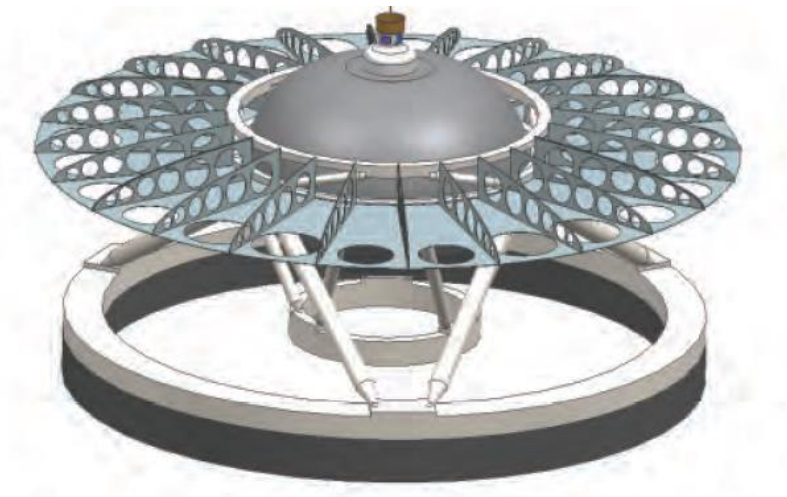

Figure 5 The Venus Intrepid Tessera Lander (VITaL) design [20]

The probe's science suite was equipped to address the key science objectives presented by the Decadal Survey for a mission to Venus and specifically for a Venus In-Situ Explorer (VISE) mission. The science goals of the VITaL mission, as reported by Gilmore et al., are as follows [20]:

1. Characterize chemistry and mineralogy of the surface
2. Place constraints on the size and temporal extent of a possible ocean in Venus's past
3. Characterize the morphology and relative stratigraphy of surface units
4. Determine the rates of exchange of key chemical species (e.g., S, C, O) between the surface and atmosphere
5. Determine whether Venus has a secondary atmosphere resulting from late bombardment and the introduction of significant outer-solar system materials, including volatiles
6. Characterize variability in physical parameters of the near surface atmosphere (pressure, temperature, winds, radiation)
7. Place constraints on current levels of volcanism
8. Measure ambient magnetic field from low and near-surface elevations

To achieve these diverse scientific goals, VITaL used primarily high TRL instruments most of which leverage heritage from various exploration missions. These instruments, how they relate to the science objectives, and their TRL estimate reported by from Gilmore et al. [20] are summarized below in Table 1.

Table 1 Instrumentation on the VITaL lander [20]

Instrument	Abbr.	Mass (*kg*)	Objective Contribution	Reported TRL
Neutral Mass Spectrometer	NMS	11	2,4,5,7	High
Tunable Laser Spectrometer	TLS	4.5	2,4,7	High
RAMAN/Laser Induced Breakdown Spectroscopy	LIBS	13	1,2,4	Medium
Descent Imager	-	2	1,3	High
Magnetometer	-	1	8	High
Atmosphere Structure Investigation	ASI	2	5	High
Panoramic Imager	-	3	3	High
Context Imager	-	2	1,2,4	High

The instrument of interest is the Raman-LIBS spectrometer. This instrument has the lowest TRL of any of the other instruments selected for this mission. The Raman-LIBS is a two stage laser with a telescope that enables it to take in-situ mineralogy measurements of samples 2.5 m away from the lander. The optics of this laser are very sensitive and would require notable development and test to certify them for the 200 *g* ballistic entry that was planned for the VITaL mission. For this reason the Decadal Survey listed the development of a high TRL Raman/LIBS instrument as one of the most significant challenges to the mission [14].

The prime objective of VITaL was to sample and analyze the composition of the Tessera terrain [20]. The VITaL mission was designed to land near the equator in the Ovda Regio. Measurements from the Magellan mission have shown that the Tessera regions generally have slopes that range primarily from 5°-10° at the kilometer scale [32,33]. However, this does not include smaller scale fault scarps and other ridges which are expected to be approximately 35° [34] or the local scale surface roughness which is expected to be on the order of 0.1 *m* [35].

Data collected from the Magellan mission was used to identify the primary structures of the Ovda Regio. It was found that the geological formations of this region is largely dominated by a criss-crossing of shallow, yet steep-walled troughs, known as ribbons, and geological folds. The ribbon pattern of the Ovda Regio is expected to be abrupt with wall heights on the order of 100 *km* and fault dip angles ranging from 75° to 90° [36]. The geological folds in this region are more distributed on the order of 25 to 50 *km* wide with a spacing between peak from 5 to 15 *km*. It was predicted that the maximum crest to trough altitude

difference is 1 *km*. The sharpness of the peaks can be characterized by the interlimb angle which ranges from 157–172° [36].

In order to increase mission reliability, the 50 *km* by 150 *km* landing ellipse for the mission was selected to be in a relatively flat location, as seen in Fig. 6. This region has an average slope less than 5° [20] and contains fewer ribbon structures than many other areas in the Ovda Regio. The slopes presented in Fig. 6 are based on measurements taken from Magellan's Synthetic Aperture Radar (SAR) which has a resolution of 75 *m/pixel* [20]. As a result, these values are dominated by the macro-scale slopes of the geological folds and largely do not represent the steep, abrupt slopes of the ribbon structure, though the ribbon slopes present a larger risk to the mission.

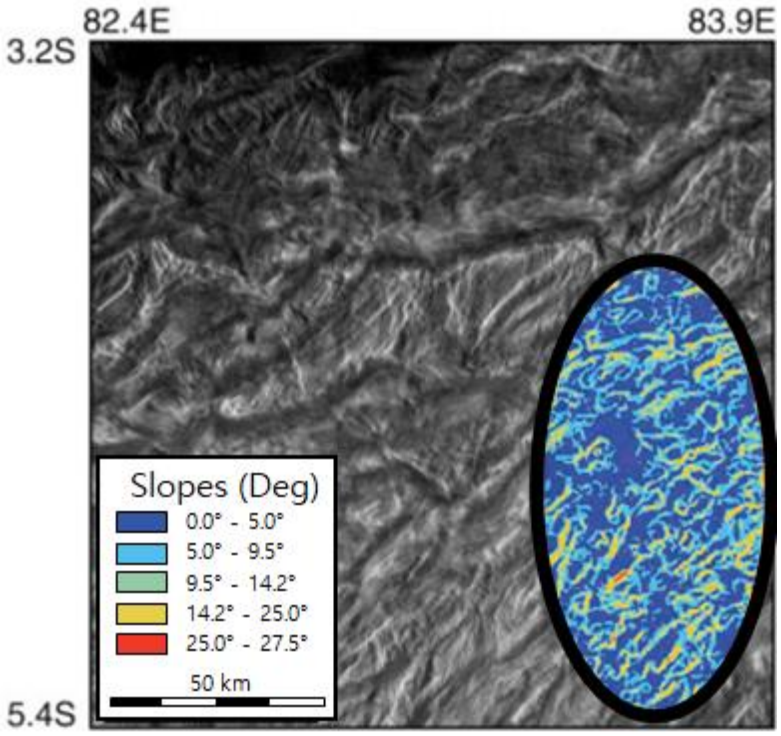

Figure 6 Landing ellipse for the VITaL mission: SAR image of the Ovda Regio was from [36] **and macros-scale slopes in the landing ellipse derived from** [20]

In order to combat these challenges, VITaL's design was specifically made in order to handle the hazardous landing conditions and steep slopes that may be encountered in Tessera regions. The VITaL lander employs a wider and heavier toroidal base than was used in the Venera missions to achieve a very low center of gravity and increase its landing stability. The baseline design of VITaL had a static tipping stability of over 72°. Despite this robust design the Decadal Survey still identified the surface roughness of the Tessera region to be the primary risk of the VITaL mission and deemed that the Tessera region can be "viewed as largely inaccessible for landed science…" [14].

Although the concept has not been selected for additional study beyond the initially commissioned work of the Decadal Survey, this mission concept serves as a benchmark that other concepts can be compared to. In this dissertation, much of the work developed for VITaL was used a foundations for the conceptual mission to Venus developed to show the merit of the TANDEM design for missions to hazardous environments. The instrumentation, thermal control system, and pressure vessel design from VITaL were all adapted to the developed vehicle's design to ensure that both concepts could perform the same science. With both the VITaL and TANDEM mission concepts going to the same destination and carrying the same payload, a direct comparison of the two landers will be made. This will highlight the benefits of a tensegrity lander over the heritage design of a Venera Class lander.

Advanced Deployable Entry and Placement Technology (ADEPT)

As payload sizes for robotic missions to other celestial bodies are growing larger, new entry vehicles are being explored that can handle the larger payloads while still fitting within existing LVs. Mechanically deployable heat shields open like an umbrella allowing them to be stowed at a small cross sectional diameter and then deployed for entry to produce a large drag area. The most notable mechanically deployable heat shield is the well-established ADEPT concept [4–8].

ADEPT's thermal protection system (TPS) is comprised of a 3D-woven carbon fiber fabric The carbon fabric is a flexible skin that functions as both the TPS and the structural support that transfers the aerodynamic loads to the frame of the entry vehicle. This technology was extended for use in the current proposed EDLL vehicle concept such that it can provide the same benefits as ADEPT, while substantially reducing the vehicle's. The fabric has been arc jet tested at Venus Entry conditions [37,38], and will be flying on a sounding rocket in September 2017 [39].

Beyond enabling larger scientific payloads to be flown, ADEPT has some significant benefits for the Venus entry environment. Traditional entries into the Venusian atmosphere, typically had very steep flight path angles ranging from approximately 20° to nearly 80° [40]. The flight paths used were largely due to the characteristics of the TPS material, which had a high density and high thermal conductivity. In order to minimize the mass of a vehicle using such a material, high entry flight path angles (EFPA) were used to increase the magnitude of the peak heat pulse while its duration was shortened. As the EFPA increased so did the peak deceleration of the vehicle. Thus the steep Venus entry is a limiting factor in the type and amount of scientific payload that can be include in a mission to Venus. Much of the scientific equipment that is desirable for an in-situ mission to Venus, like the Raman/LIBS Spectrometer, is not capable of surviving the 200-400 *g's* experienced on entry with traditional entry vehicles.

In order to reduce the deceleration loads of the entry vehicle, a shallower EFPA must be used. This, however, presents a technology challenge, because as the EFPA decreases for a Venus entry the total heat load grows exponentially. This require a thicker heat shield and thus the mass of the entry vehicle increases, decreasing the payload mass fraction. While modern lightweight TPS concepts are now being developed which can enable rigid entry vehicles to enter at shallow EFPA [41], an alternative method to enable shallow entries is to decrease the vehicle's ballistic coefficient (mass to drag area ratio). Lowering the ballistic coefficient also lowers the peak heat flux and total heat load of the due to entry.

One method to achieve this lower ballistic coefficient is by using deployable entry vehicles like ADEPT. The low ballistic coefficient of ADEPT enables it to enter at EFPA close to the skip out angle, reducing the expected entry loads to well below 100 *g's*. This expands the range of scientific equipment that can be included and reduces their expected mass by 10% - 25% by reducing their required structural reinforcements. This was seen in the ADEPT-VITaL mission study [4].

The ADEPT-VITaL mission was a hybrid concept where the traditional entry vehicle for the VITaL mission was replaced by the ADEPT entry vehicle, as seen in Fig. 7. The design changed would raise the TRL of the Raman/LIBS instrument as it would no longer need to be certified for entry loads on the order of 30 *g's* [4]. The inclusion of a mechanically deployable entry vehicle eliminated one of the biggest challenges of the VITaL mission, but it offers no benefit to the other key challenge of safely landing in the Tessera regions. This case study highlights the benefits of using a deployable entry vehicle for missions to Venus. Furthermore, a comparison of the TANDEM and ADEPT-VITaL mission will be performed to specifically highlight the compounding benefits of combining tensegrity landers with mechanically deployable entry vehicles.

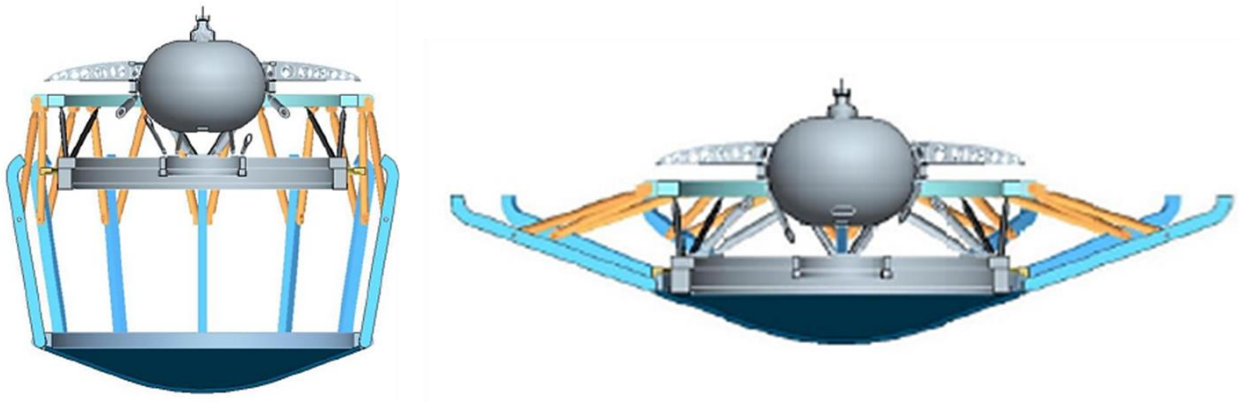

(a) (b)

Figure 7 The ADEPT-VITaL concept houses the VITaL Lander inside an ADEPT entry vehicle [38]**, (a) stowed configuration (b) deployed**

Tensegrity Robotics

Tensegrity systems provide a non-traditional solution to many problems encountered in a space mission, such as size and mass constraints. Members of a tensegrity structures are classified as discrete structural elements which hold either a compressive or tensile load. Tensegrity structures distribute their loads through a network of tension cables while maintaining their shape through a set of discontinuous rods in compression. By isolating the loads in this manner, the mechanical complexity of the structure is reduced. Furthermore, the truss-like structure utilized by tensegrity systems lend themselves to lightweight designs. To avoid confusion, in this dissertation the terms bar, rods, and compression members are synonymous with each other, as are the terms cables and tension members.

Because the tension network is incapable of supporting a compressive load, the truss-like structure must be developed in a predetermined, stable geometry that isolates the compressive loads to the compression members and the tensile loads to the tension network. This predefined stable geometry is also referred to as an equilibrium configuration. It is shown in Chapter 4 that the equilibrium configuration of a tensegrity structure can be found in terms of either the length ratios of all of the members (also referred to as the length coefficients) or the normalized internal force (also referred to as the tension coefficients).

The term tensegrity was coined by Buckminster Fuller and is the conjunction of *tensile* and *integrity* [42]. Fuller is credited with bringing the concept into the engineering world from the world of structural art where it was largely pioneered by artist Kenneth Snelson [43]. Most of the traditional applications for tensegrity structures is in the field of civil engineering, with applications as domes [44,45], towers [46,47], and bridges [48–50] to list a few. An image of the largest tensegrity bridge can be seen in Fig. 8. Additional information on classical tensegrities, their history, and a more complete list of applications consult the textbooks by Motro [51] and Skelton [52].

Figure 8 The Kurilpa Bridge, in Brisbane, Australia is the world's largest [50]

In the field of civil engineering, tensegrity structures are largely considered as static structures. However, tensegrity structures, as they are used in this dissertation, lend themselves well to smart or active structures. The design of other active structures can be complicated by stiff and rigid joints. These joints are typically the intersection of various load paths and as such are subject to large bending or shearing loads. Tensegrity structures eliminate these heavy joints by controlling the length of various tension members. As the tension network length coefficients are changed, the overall geometry of the structure can be changed from one equilibrium configuration to another [53]. This provides a robust method of actuate tensegrity structures into systems that can be stowed and deployed [54–56] or even controlled to produce a tensegrity robot, which can walk, crawl, and/or roll on the ground [11,57,58].

The NASA Innovative Advance Concepts (NIAC) research by Agogino et al. [59] and SunSpiral et al. [60] (for the Phase I and Phase II study respectively) largely pioneered the planetary exploration application of tensegrity robots. Their robot, known as the Spherical Under-actuated Planetary Exploration Robot ball (SUPERball), has demonstrated the excellent crashworthiness that can be obtained by spherical tensegrity robots.

Similar robots can be designed to withstand impact speeds up to the robot's terminal velocity. This enables the robots to safely explore significantly rougher terrain that other planetary explorers. With tensegrity robots, it is now feasible to explore cliff and other steep slopes without risking damage from rolling down the slope or off the cliff. This is an enabling technology in many ways. This technology is the key that opens up landed science in the Tessera regions. In this dissertation the versatility of tensegrity robotics was incorporated into the development of the new EDLL vehicle to provide it with unique and multifunctional capabilities.

Chapter 2
Venera Class Landers

In an effort to set a benchmark that represents the current state-of-the-art for an in-situ mission to the Venusian surface, a number of existing proposed missions to Venus were investigated. Unlike the more frequently explored Mars, Venus is more suitable to alternative robotic exploration methods. The exploration of Mars to date can be broken into three basic categories: orbiter [61–63], lander [64–66], and rover [67]. These modes of exploration have been seen and proposed for Venus [31,68–72], but Venus' dense atmosphere also makes balloons [73–78], billows [79,80] flyers [81–83], sailors [84], atmospheric probes [85], and other wind powered concepts [86] just as viable methods of exploring Venus. The white paper put out by the Venus Exploration Analysis Group (VEXAG) provides a good introduction and overview of the various types of missions that are foreseen for Venus exploration and the technologies required for these missions [87].

With all of these various methods of exploration, special attention was given to those that were most commonly proposed and those that had the highest TRL. The baseline design was down-selected to a lander concept and the most common design for a new Venus lander is the heritage design of the Venera Landers [20,88–91]. The original Venera landers have been thoroughly investigated and reverse-engineered in this study to understand the key attributes in Venera Class of landers. Understanding the Venera landers design will add to the design of a new Venera Class benchmark landers for future missions to Venus.

The primary structures of the Venera lander are analyzed as four distinct functional components. From top down, those four component are: the parachute canister and drag-plate, the payload module, the legs, and the impact ring. For simplicity's sake, the parachute capsule and the drag-plate are grouped into one component because although both components are necessary for descent, they do not add much to the structural response of the lander at impact. The payload module was comprised of a pressure vessel, an internal stiffener, the payload contained within it, and the insulation surrounding it. The payload module was roughly one meter in diameter, 80 cm diameter pressure vessel with the remaining thickness contributed to the insulation [26]. All the sensitive instruments were housed inside the spherical pressure vessel. Although the payload of each mission changed, the overall size and design remained constant.

Below the payload module is what many schematics label “Посадочное устройство” which directly translates as “landing gear.” In this work, the “landing gear” was further broken into two subcomponents: the legs and the impact ring. There were 18 legs that connected the payload module to the impact ring below. Unfortunately, credible and verified sources of information on the landing gear are very hard to come by. As a result, the resources available are typically secondary sources from western literature which contain some misconceptions as to how the landing gear performed and do not by themselves present a conclusive design of the landing gear [22,25–27]. Both Bond [25] and Soediono [26] mention that legs were some type of shock absorber; while Ball [22], Keldysh [27], and many more make no mention of the legs. One original source, translated from Kosmichekie Issledovaniya, describe the legs as, “rods, …[forming] a three-dimensional truss” [92].

To add to the ambiguity, none of the publically available schematics of the Venera and Vega landers show any internal components of the legs. However, due to their short length and small diameter it is likely that they were likely just rigid rods as described by Boiko [92] or a secondary energy absorbers used to isolate payload from much of the shock wave due to impact. The legs also provided the added benefit of keeping the payload module off the ground. Because a wide scale survey of Venus wasn’t preformed until NASA’s Pioneer Venus Mission in 1978, the topography of the surface was largely unknown [93]. Even today due to the thick cloud layer, the resolution of the mapped surface is relatively coarse. Topography data from Magellan’s Synthetic Aperture Radar has a resolution of approximately 2 km [16]. If the lander happened to impact on a very rocky terrain, the payload module’s pressure vessel would be susceptible to a penetration. Due to the extremely high pressure at the surface, even a small impact to the pressure vessel could lead to buckling of the pressure vessel which could damage or destroy the payload. The legs add clearance to the payload module to decrease the risk of penetration in this scenario.

There is a consensus in the literature that the impact ring was a hollow metallic torus, designed to crush on impact. The crushing of the impact ring would convert much of the kinetic energy of the lander into plastic strain. Additionally, the impact ring had holes perforating the outer surface of the metallic shell. These holes, visible in Fig. 4, had several interesting characteristics. The obvious reason for these holes is to equalize the atmospheric pressure pushing on the outside of the ring with the internal pressure. But because of these holes allowed the ring to be filled with the dense atmospheric gases, when the impact ring was crushed, the high density fluid forced out of these holes added some viscous damping to the impact sequence.

However, results from Avduevskii et al. conclusively showed that the impact ring did not crush for the Venera 13 & 14 missions [94]. Instead, they presented, “Since the ground-based test showed that deformation of the landing device does not occur for the magnitude and character of the impact overloads

obtained in the course of the flight experiment…, one can consider to a first approximation that [the] lander is a rigid body interacting with a yielding soil….” Avduevskii et al. also show that the impact ring did crush when the landing surface was very stiff (e.g. cement foam). From this it can be concluded that the original landing gear of the Venera landers were designed with a variety of different impact surfaces in mind. For soft, sand-like impact surfaces, the lander behaved like a rigid body, allowing the soil to dissipate the impact energy. For surfaces that were stiffer but still yielded some, the impact ring would crush. It is possible (but unconfirmed) that for near rigid impact surfaces, the legs would also buckle to add an addition energy dissipation mechanism. This could be the shock absorber in the legs mentioned by both Bond [25] and Soediono [26].

Energy Absorbers

Energy absorbers can be classified as a mechanism used to dissipate or absorb energy. Classical energy absorbers use friction and damping as well as irreversible deformation [95]. The Venera landers likely utilized both classifications. Although both methods were viable options, each one presents a significant engineering challenge. Therefore, a variety of options were considered for the new baseline model.

Viscous dampers could be used in the new Venera Class lander baseline, although a number of obstacles must be overcome for them to be used. The design of a viscous damper, such as a dashpot in the legs, would need to overcome the effects of the extreme temperature change. Within approximately one hour the fluid will transition from the temperature maintained in transit to the surface temperature, approximately 485ºC. Under this variation most fluids will be subject to phase change, as well as change in specific volume, viscosity, and several other critical properties.

Alternatively, the new baseline design could implement irreversible deformation using landing legs; allowing the legs to plastically deformation/buckle on impact to provide a form of shock absorption. This mechanism would be significantly simpler to account for the temperature change and would be easy to predict analytically or computationally. However, deforming the legs is not the method chosen as it loses the added benefit of keeping the payload module off the landing surface. Using this mechanism would lead to a decrease in reliability of the lander and would increase the risk of pressure vessel impacting the surface.

The hybrid mechanism used in the impact ring of the original Venera landers was a clever utilization the landers environment. While the original impact ring is mass effective mechanism, it is complicated to predict analytically, computationally, and experimentally because its damping mechanisms is based on complex fluid structure interactions. This is not conducive for rapidly analyzing various designs and thus may not be suitable for the baseline model.

Because of these complications, none of the aforementioned energy absorbers were chosen for the new baseline design. Alternatively, the use of crushable honeycomb and metallic foams was substituted in place of those mechanisms to provide a lightweight concept with highly predictable impact characteristics. Although its first use as an energy absorber in the Apollo 11 landing gear predated the design of the Venera lander by a couple of years, metallic honeycomb was not used for the Venera lander because the technology was still extremely new and was not yet a commonly used energy absorber [96].

As far as compressive energy-absorbers are concerned, honeycomb and metallic foams offer near ideal energy absorption characteristics. The energy absorption process can be broken into three phases: initiation, plastic deformation, and densification, as seen in Fig. 9. The initiation phase occurs on impact and is characterized by purely elastic deformation. That is, if the deformation does not exceed the initiation phase, the material will return back to a zero stress and zero strain state. However, after the initiation phase is surpassed, the thin walls of the honeycomb structure will begin to buckle in a near uniform periodic distance. This progressive buckling behavior is what contributes to the near ideal energy absorbing characteristics of honeycomb. Throughout the plastic deformation phase, impact energy is absorbed at a constant rate until the densification phase is reached. When the material is fully condensed the stress/strain relationship returns to a near linear state. Honeycomb materials can crush up to 80% strain before the densification phase begins.

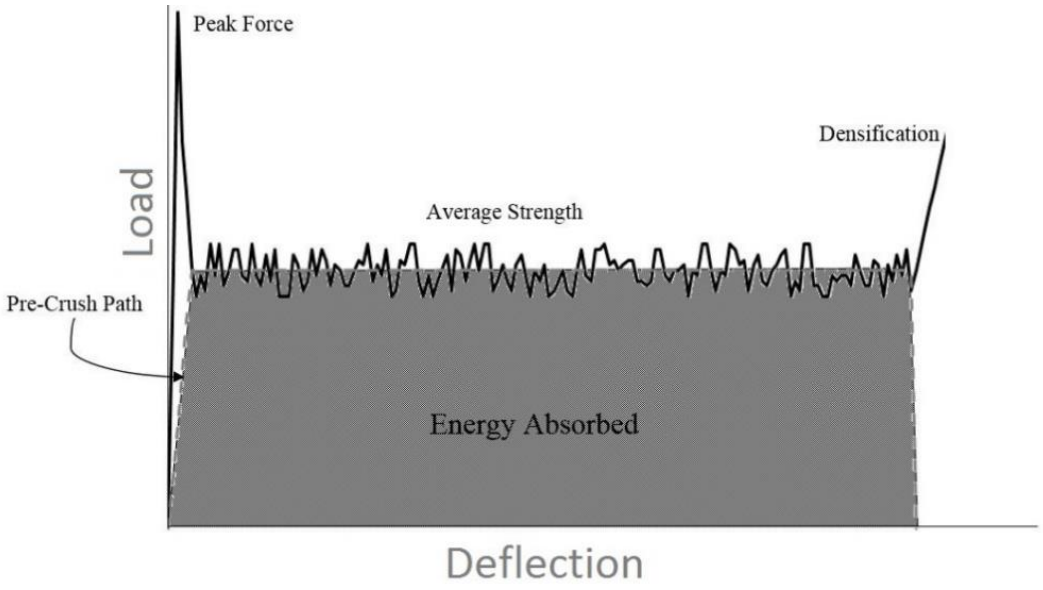

Figure 9 Honeycomb crush load versus deflection relationship

The average crush load of the honeycomb can be tailored by the geometry of the honeycomb cell and the thickness of the cell wall. Thus, a wide range of crush strengths can be attained by simply adjusting the geometry or material of the honeycomb. Better impact characteristics for honeycomb can be obtained

from a procedure called pre-crushing, which applies a load to the honeycomb and allows the material to surpass the peak force start buckling before it is unloaded. Now that the buckling has been initiated, the peak load can be bypassed the next time the material is loaded.

Metallic foams respond similar to honeycomb but with some differences. Metallic foam typically reach densification before honeycombs at roughly 60% strain. Thus foams have a smaller specific energy absorption than honeycomb, however, they are effectively an isotropic material. While honeycomb is restricted to a specific orientation and in some cases requires a guide, metallic foams can be crushed predictably under any impact orientation.

For these reasons, the investigation of the Venera Class landers for future missions to Venus will utilize honeycomb legs and a low density open cell metallic foam for the impact ring. Honeycomb legs concept is a reasonable choice for many of the reasons mentioned above. In addition to the fact that the legs are already designed to only apply an axial load that will facilitate the proper guided crushing of the honeycomb without adding any complexity. The impact ring on the other hand, will be better suited by the metallic foam because it is likely that the ring will not impact perfectly normal to the surface.

Multi-Fidelity Design Tool

In order to see how the design of each component affects the lander as a whole, it was important to analyze each component individually. With the vast number of different combinations, it was impractical to model and test all combinations. Instead, a system was created to systematically analyze the multiple variations at three distinct levels of fidelity.

Figure 10 gives an overview of different levels of fidelity that were used in this study. The low-fidelity model uses geometric constraint and analytical approximation of the impact response of the lander. This model is able to provide predictions of the lander's total mass, impact velocity, and peak deceleration at impact for an ideal impact on a rigid surface. The medium-fidelity model automatically creates a finite element model based on imported sizing parameters from the low-fidelity model. This model can be used to test various impact scenarios and impact orientations at a relatively low computational expense. The high-fidelity model offers a more detailed simulation than the previous models but is more time-intensive, both to build and to run. However, the high-fidelity model is able to accurately predict the stress concentrations in the model. It is noteworthy to mention that neither the medium nor high-fidelity models explicitly model the drag-plate and parachute capsule because they offer minimal structural contributions to impact. However, both models include the mass of the drag-plate and parachute capsule as well as their effect on the landers terminal velocity.

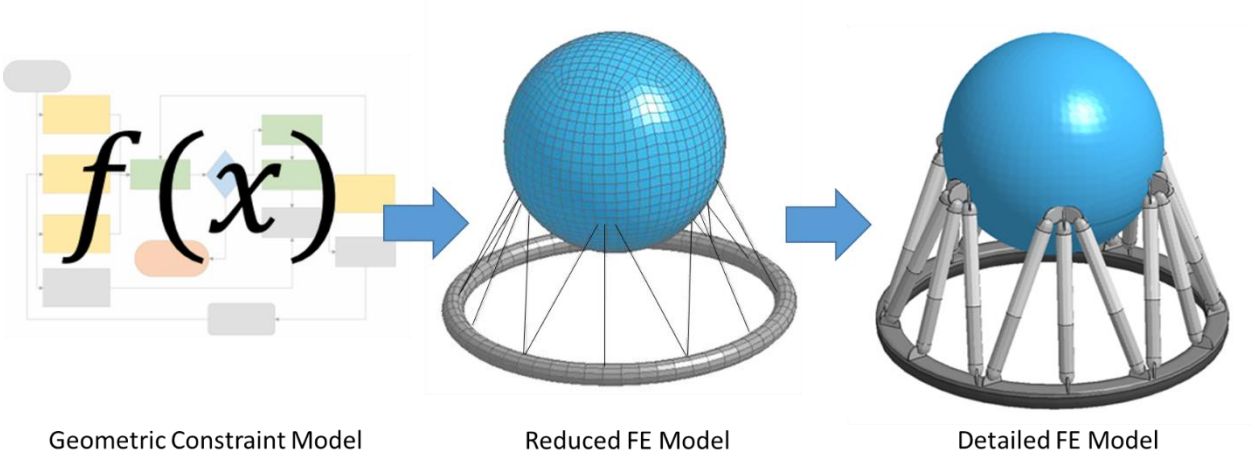

Figure 10 Multi-fidelity models

With this multi-fidelity design tool, the characteristics inherent in the design of the Venera Class lander were investigated efficiently. The low-fidelity model can rapidly analysis dozens of variations within seconds. From there, data from the most promising designs can be passed up to the medium-fidelity to dynamically simulate the various impact conditions with a still relatively low run time. When a final design is chosen, its parameters are used to create the high-fidelity model to investigate the detail of the model.

Low-Fidelity Geometric Constraint Model

Each of the four key components mentioned above were approximated as simple geometric shape so that the volume of material that comprised them and thus their mass could be calculated. Most of the major components were modeled as follows; the payload module as a hollow sphere with uniform thickness, the legs as cylinders, and the impact ring as a torus. The drag-plate and some of the minor components (e.g., the joints connecting the legs to the impact ring and payload) were modeled based on engineering estimates. From this work, an accurate account of how each component contributed to the landers overall mass was made.

An additional benefit to modeling each component based on geometric constraints is that the configuration of the lander can easily be parameterized and modified to predict how the lander will behave for various vertical impact scenarios. Each major component could be varied with respect to the others to see how it would affect the impact characteristics of the lander as a whole. These results together with the estimated mass of each lander configuration would be used to find the optimum lander designs.

Within the design of the Venera Class lander, there are dozens of parameters that can be varied. In order to predict the mass and impact characteristics of any lander configuration, a systematic approach was employed to simplify the process. For this reason, many of the design parameters were found to be

interdependent on other parameters. For example, the amount of honeycomb needed to properly absorb the kinetic energy can be calculated from the landers kinetic energy, which is a function of the landers mass and terminal velocity. Additionally, the required thickness of the payload module to prevent buckling under hydrostatic pressure is a function of the pressure vessels radius.

By finding multiple relationships such as these and keeping some of the obviously minor variables fixed, the entire model was simplified down to 10 major design variables. The payload module was sized as a function of its radius and mass. The distance the payload module initially was above the impact ring was modeled by the parameter "Payload Height." The impact ring was modeled based on its radius, width, and the aspect ratio of a cross section of the metallic foam's. The drag-plate was sized as a function of its radius and complementary cone angle. Finally, the legs were modeled based on the number of legs and their configuration. Some of the additionally parameter used in the geometric constraint model are discussed in their respective sections below, but these values were held constant during the verification of the multi-fidelity design tool. Figure 11 shows the primary geometric design variables.

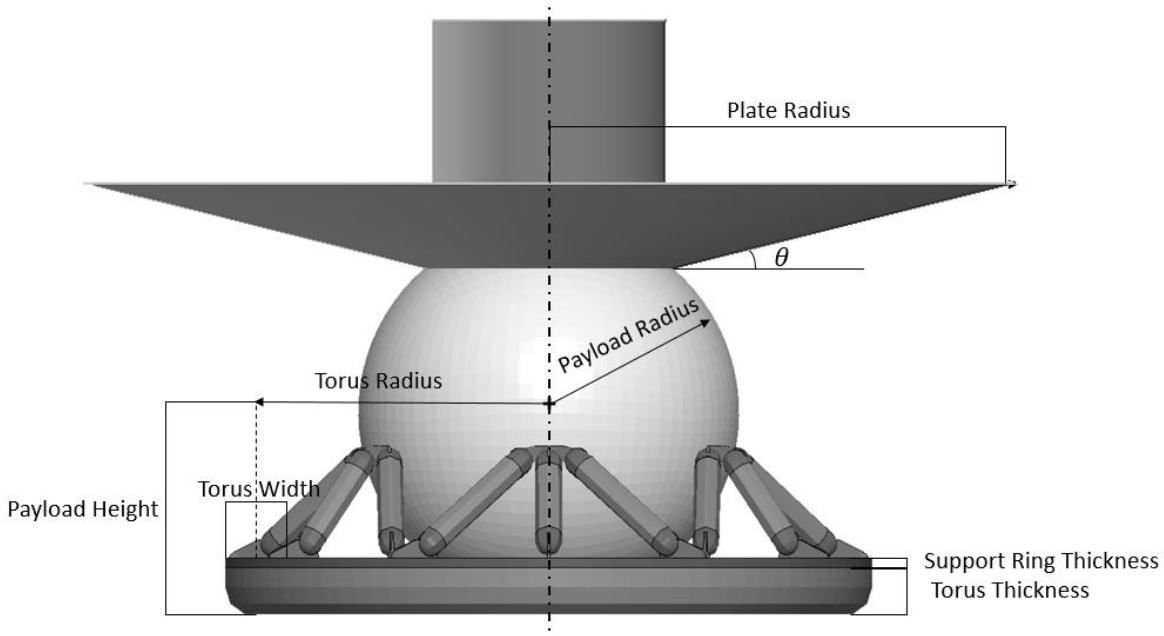

Figure 11 Primary geometric design variables

A process overview of the low-fidelity model is shown in Fig. 12. The ten input parameters, seen at the top of Fig. 12 were used to size the drag-plate, the payload module, and the impact ring. Together, those masses would be used as the initial estimate of the landers total mass. The total mass was used to calculate the terminal velocity and the kinetic energy of the lander, which in turn was used to size the legs.

The additional mass of the leg was then fed back into the total mass of the lander for the next iteration. The iterative solver continued until a 99% convergence of the lander total mass was achieved.

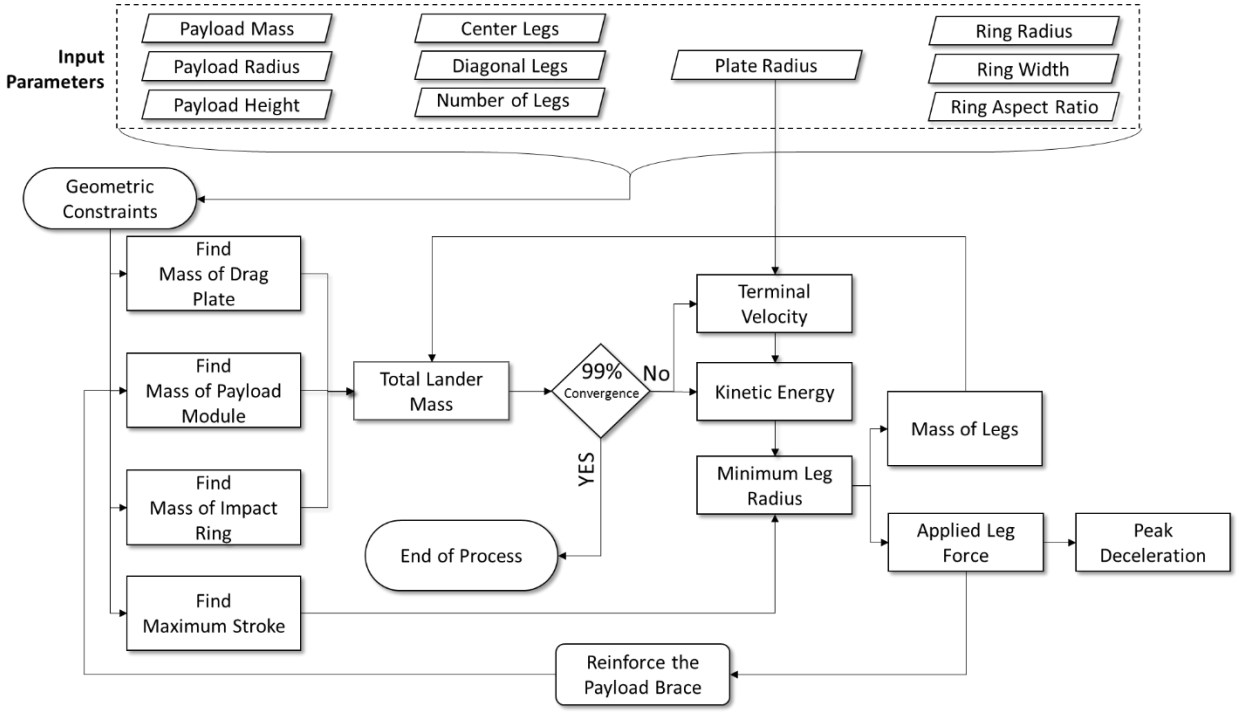

Figure 12 Geometric constraint model process

Drag-Plate: The drag-plate in the low-fidelity model is defined by four variables: projected plate radius, complementary cone angle, plate thickness, and normalized plate attachment point. The plate attachment point, η_{plate}, is a value that varies from -1 to 1 and represents where on the payload module the drag-plate is attached, where -1 is the bottom, +1 is the top and 0 is the middle of the module.

A large amount of computational expense could be invested in order to find the coefficient of drag (C_D) of the lander based on each of these parameters, however, this is beyond the scope of this study. Because each configuration can potentially yield a different coefficient of drag a simple surrogate model was developed to predict the C_D based on the size of the radius of the drag-plate compared to the payload module radius and the cone angle of the drag-plate. It is intuitive that the drag coefficient of the lander will have a minimum no less than the coefficient of drag for a sphere at the same Reynold's number and a maximum no more that of a flat disk. Both the drag of a sphere and a flat plate have been well studied for the Reynolds numbers seen near the surface (order of $6x10^6$ or higher). These shapes yield a C_D of 0.16 and 1.17, respectively [97–99]. Thus the approximate C_D of the lander should be approximately 0.16 for designs where the normalized difference between the drag-plate and the radius of the payload module at the plate attachment point is small. For designs where the difference is large and the cone angle is approximately

90°, the C_D should be close to 1.17. Given the previous conditions, the C_D for this analysis was varied based on the Eq. (1)

$$C_D = 0.0112(90-\theta)\left(\frac{r_{plate} - r_{payload}\sqrt{1-\eta_{plate}^2}}{r_{plate}}\right)^{0.6} + 0.16 \quad (1)$$

where C_D is the vehicle's approximate drag coefficient, θ is the drag-plate cone angle, r_{plate} is the radius of the drag-plate, $r_{payload}$ is the payload module radius, and η_{plate} is the non-dimensional vertical attachment location of the drag-plate on the payload module (measured in percent of radius away from the module center). The constants from Eq. (1) were tuned to match empirical data. For verification of this C_D approximation, it can be seen that when there is no drag-plate the term in the parentheses is zero (that is $r_{plate} = r_{payload}\sqrt{1-\eta_{plate}^2}$), thus $C_D = C_{D_{sphere}}$. Additionally, it can be shown that when $r_{payload} = 0$, the C_D matches the trend shown by Hoerner for cones of various cone angle [99]. For the case where $r_{payload} = 0$ and $\theta = 0°$, $C_D = C_{D_{disk}}$. Finally, based on a number of physical experiments performed by V. P. Karyagin et al. it is known that the coefficient of drag for the Venera landers was 0.8 or greater for high Reynolds numbers (order of $6x10^6$) [100]. When the parameters based on the original Venera landers ($r_{payload} = 0.5,\ r_{plate} = 1.075m,\ \eta_{plate} = 50\%,$ and $\theta = 10°$) are used in Eq. (1), the estimated $C_D = 0.82$. With the C_D calculated from Eq. (1), the terminal velocity was found and used to estimate the total kinetic energy of the lander before impact.

Payload Module: As mentioned previously, the payload module is comprised of multiple subcomponents. These subcomponents include all the scientific payload, the pressure vessel, an internal brace to provide additional structural stability where the leg connect to the module, and the required insulation. Due to the mechanical focus of this study, only the structural components were modeled explicitly. The non-structural components (e.g., the scientific payload and the insulation) are taken into account by the payload mass.

The pressure vessel required two parameters to fully define its geometry, the radius and thickness of the pressure vessel wall. Numerous analytic and experimental investigations of buckling in thin walled spheres under external pressure have been made. Zoelly was the first to provide an analytical solution for the critical applied load given the material properties, radius, and thickness of the sphere [101] and has since been reported in various other works. This equation was used to scale the thickness of the pressure vessel based on the desired radius. Alternatively, an additional parameter can be include to add a factor of safety to the pressure vessel as seen in Eq. (2)

$$t = \sqrt{\frac{F_S P r^2}{1.2E}} \tag{2}$$

where t is the pressure vessel thickness, P the external pressure, r the vessel radius, E the material modulus, and F_S the factor of safety. Inside the pressure vessel where the legs connect to the payload module, there is a brace to add extra stiffness and resist buckling of the pressure vessel. The dimensions of the brace are scaled based on the load applied on the pressure vessel by the legs and the circumference of the pressure vessel at the connection location of the legs.

Legs: The mass of each leg is found from the mass of the honeycomb in the legs, the mass of the leg casing, and the estimated mass of the pin connection joint located at both ends of each leg. To ensure that the lander is able to safely land on the surface given its momentum, the amount of energy absorbing material is scaled based on the total kinetic energy of the lander before touchdown. For the geometric constraint model it is assumed that 100% of the kinetic energy will need to be absorbed by the honeycomb and metallic foam. Thus the radius of each leg can be calculated according to Eq. (3)

$$r_{leg} = \sqrt{\frac{\frac{1}{2} m_{total} V_{terminal}^2 - IE_{ring}}{\pi \sigma_{leg} \sum S}} \tag{3}$$

where r_{leg} is the radius of a single leg and defines the amount of honeycomb material in each leg, m_{total} is the mass of the Venera lander, $V_{terminal}$ is the lander's terminal velocity, IE_{IR} is the maximum energy that can be absorbed by the impact ring, σ_{leg} is the crush strength of the honeycomb material in the legs, and $\sum$S refers to the total stroke of all of the legs which can be found from the geometric constraints set up by the 10 input parameters. The leg was given the most variability out of any other component. Not only are the length of the leg and its connection point to the payload module variables, but the number of legs and their configuration were also allowed to change. A trade study was performed to see how sensitive the legs were to the overall design. The three most successful leg configurations are shown in section IV.C. As seen in Fig. 4, the original Venera lander utilized a tri-leg configuration with 18 total legs.

Impact Ring: The impact ring was comprised of an upper and lower sections. The lower section was comprised of the metallic foam. The amount of metallic foam used was defined by the three parameters mentioned previously: ring radius, torus width, and foam aspect ratio. The upper section was a solid titanium ring to support the metallic foam as well as provide a stable location where the legs could be attached. The solid ring was defined by the ring radius, torus width, and ring thickness variables. The amount of energy absorption provided by the impact ring was calculated by Eq. (4)

$$IE = \sigma AS \tag{4}$$

where σ is the crush strength of the energy absorber, A is the area of crush surface based on the width and radius of the impact ring, and the stroke S was based on the thickness of the foam before the densification stage is reached. A similar equation was used to find the energy absorbed by the legs.

Peak Deceleration: The payload must be designed to withstand a certain amount of loading. During takeoff and atmospheric entry the lander will experience an elevated *g*-load. It is expected that the *g*-loads experienced during entry will be much higher, at an estimated value of 250 *g's*. To ensure the survival of the scientific equipment, the lander must be able to come to a complete stop without exceeding that maximum allowable *g*-load. To check whether the lander configuration is able to impact the surface without exceeding the *g*-limit, an estimated deceleration calculation was included in the algorithm. Because honeycomb experiences a constant force as it deforms, the deceleration will be relatively constant. The deceleration is estimated by dividing the force balance between the legs and the mass of the upper half of the lander by the combined mass of the payload module, drag-plate, and parachute according to Eq. (5) and as shown in Fig. 13

$$a = \frac{(F_{g_{paylod}} + F_{g_{plate}} + F_{g_{parachute}}) - \sum \sigma_{leg} A_{leg} cos\theta_{vertical}}{(m_{payload} + m_{plate} + m_{parachute})} \tag{5}$$

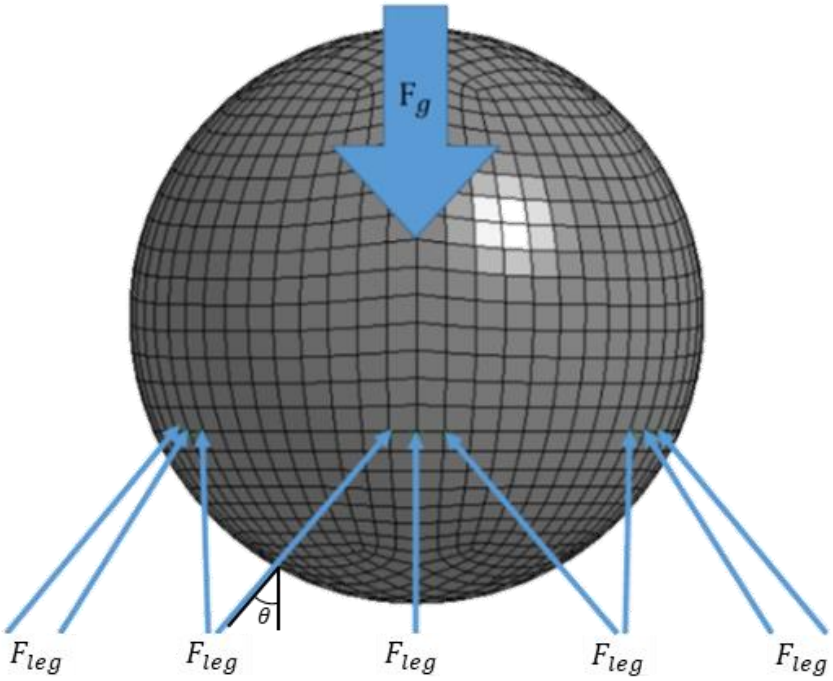

Figure 13 Free body diagram for lander dynamics

where a is the acceleration of the payload module and F_g and m are the weight and mass of various components respectively. θ is the angle each leg makes with the vertical axis in its initial configuration. If $r_{leg} = 0$, (i.e. the legs are modeled as rigid bodies) then an alternative acceleration calculation in Eq.(6) is used.

$$a = \frac{F_{g_{lander}} - \sigma_{\text{ring}} A_{ring}}{m_{lander}} \tag{6}$$

Medium-Fidelity Model

The purpose of this stage of the design tool was to further investigate lander configurations that showed promising results from the low-fidelity solution while retaining a large variability and low calculation time. This process was automated to import the calculated masses and initial conditions from the low-fidelity solution and dynamically model them. The process allowed for additional parameters to be investigated while verifying the results found by the geometric constraint model.

In order to reduce calculation time, the lander was modeled using low degree-of-freedom elements such as beams and shells. The pressure vessel is modeled as a hollow shell with an assigned thickness calculated in the geometric constraint model. The mass of the payload module is evenly distributed throughout the pressure vessel. Because an exact solution exist for the axial deflection of 1-D elements, each legs was modeled using a single truss elements. As seen in Eq. (3), the deformation of the legs, and thus the energy absorbed, can be modeled using only the cross-sectional area and the area-averaged stress of the honeycomb. A piecewise constitutive relationship, similar to the trend shown in Fig. 9, was developed to approximate the honeycomb deformation while the leg radius and approximate leg mass was imported from the low-fidelity model.

As can be seen in Fig. 14, the connection points between the legs and the payload module experience a local stress concentration. This is a result of the legs being modeled as 1-D elements and were connected to the payload with a single node. Because of this, the stresses observed in the region surrounding the connection point does not accurately predict the actual stress seen on impact. Yet, the simulation accurately predicted the payload dynamics upon impact. To be able to accurately investigate such unexpected stress concentrations, a higher fidelity model was created. The high-fidelity model was use to verify the payload dynamics of the medium-fidelity model and will be discussed in a later section.

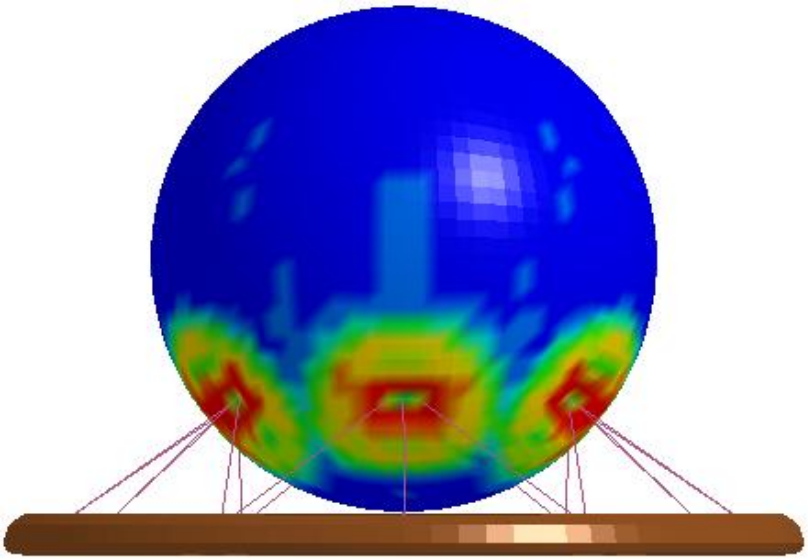

Figure 14 Stress singularities and concentrations at leg interface

High-Fidelity Model

The low- and medium-fidelity models were designed to be able to rapidly analyze design variations. In order to achieve short runtimes, these lower fidelity models ignore some of the details of the lander. Unlike the medium-fidelity model, the high-fidelity model uses brick elements to model the legs and explicitly models the connecting joints so these critical points can be investigated. Additional sub-components, such as the pressure vessel internal stiffener and impact ring frame were captured in both the medium- and high-fidelity models. As a result of these additional details, the high-fidelity model yields reasonable stress concentrations around the leg joints as seen in Fig. 15. This revealed that for most landing configurations, the stress concentration from the legs onto the payload was benign, however in some cases the initial leg joints were not robust enough to handle loads on impact causing them to fail. In these cases the leg joints were thickened and the simulation rerun. Unlike the medium-fidelity model, the high-fidelity model was constructed manually for each design. Therefore, each redesign took significantly more time to prepare and execute.

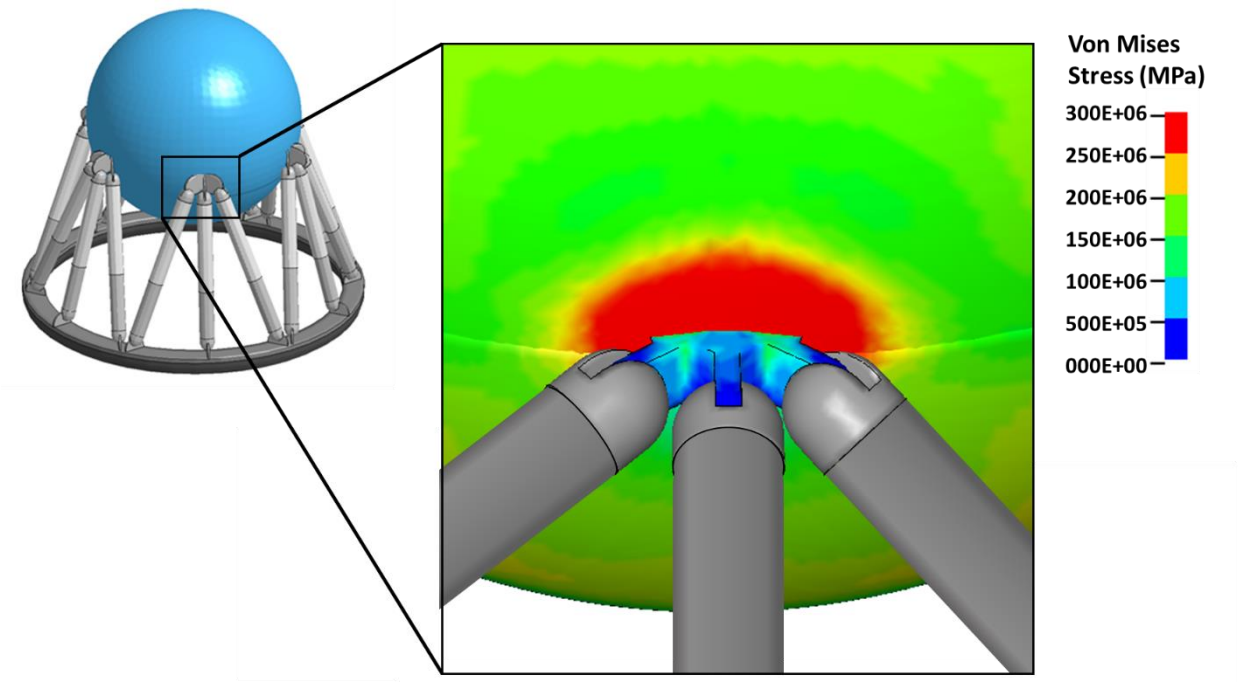

Figure 15 Stress concentration at the leg interface of high fidelity model

Once a preliminary high-fidelity model was created, a mesh convergence study was performed. A mesh convergence study was not performed for the medium-fidelity model because the stress concentrations due to the use of 1-D legs will never converge. The payload acceleration was plotted for three different mesh resolutions with approximate element sizes of 2.2 cm (coarse), 1.1 cm (medium), and 0.6 cm (fine). As seen in Fig. 16, if the mesh is too large the payload will decelerate more incrementally due to honeycomb legs being artificially stiffened due to the mesh coarseness. The finer meshes predict a more constant deceleration especially in the latter half of the impact. The peak *g's* for the coarse, medium, and fine meshes were 48.57, 45.98, and 45.52, respectively, with a 5.6% change from coarse to medium and a 1.0% change from medium to fine. The next section presents a comparison of results from the low-, medium-, and high-fidelity models.

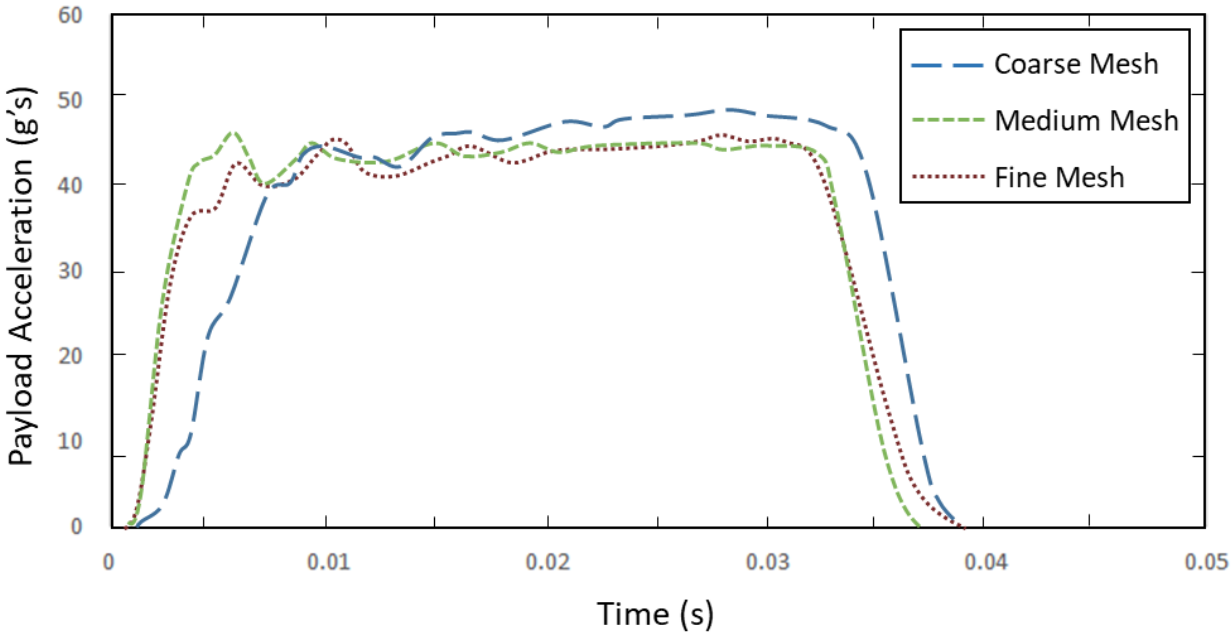

Figure 16 Deceleration of the high fidelity model for various mesh resolutions

The correlation between the kinetic and internal energies is shown in Fig. 17. The internal energy is largely contributed by the plastic deformation of the impact ring and honeycomb legs, while the kinetic energy trend follows the velocity of the payload module. These energies are significant because they quantitatively capture the impact characteristics of the lander. Because a reduced element formulation was used to decrease computational expenses, the total energy was not fully conserved. There are two major contributions to the variation in total energies: hour-glassing energy and negative sliding energy. Hour-glassing energy adds energy to the system while sliding energy removes energy from the system. The change in total energy of the system is 3%, -9%, and -12% for coarse, medium, and fine meshes, respectively. Typically, simulations that conserve energy well are more reliable. As seen in Fig. 17, the coarse mesh simulation generates a significant amount of total energy directly after impact. Although the coarse mesh's initial and final total energies differ by only 3%, the energy generation implies that is simulation has a lot of hour-glassing energy. The maximum change of total energy in the coarse model shows an hour-glass energy of 13%. Typically hourglass energies should be within 10%, which is considered acceptable [102]. The medium and fine meshes show have significantly less hour-glassing energy. Although they lose a little bit of total energy throughout the simulation as a result of the negative sliding energy, this mode of energy dissipation is not detrimental to the simulation. Based on the slightly better conservation of energy and due to significantly higher computational cost of the fine mesh, it was decided that the medium mesh size would be sufficient for all further investigation.

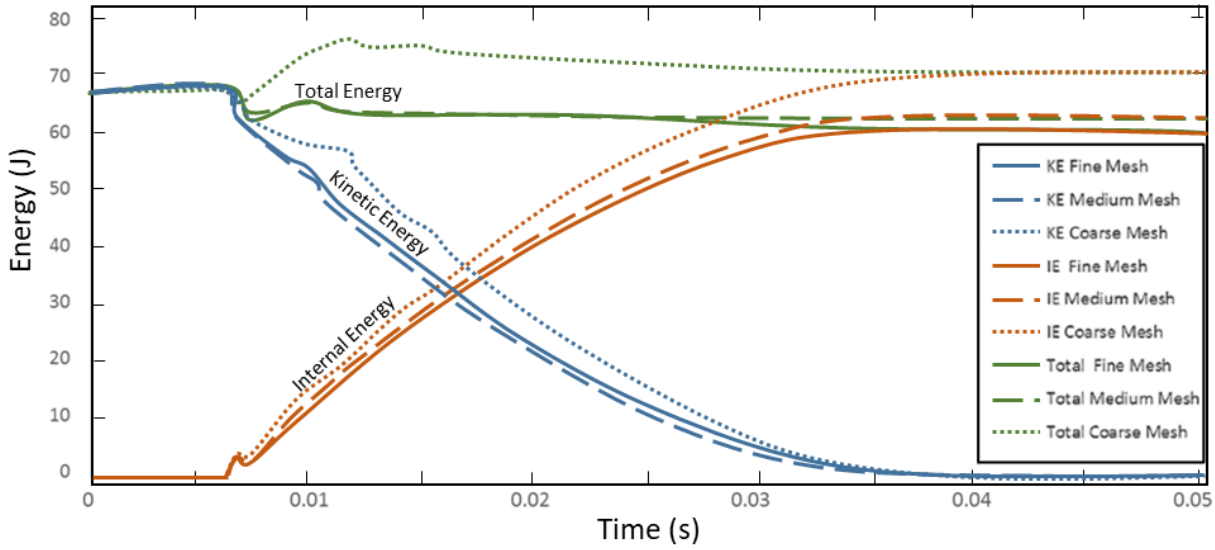

Figure 17 Energy of the high fidelity model for various mesh resolutions

As a result of the detailed modeling of the lander in this model, the unsteady response of the honeycomb under dynamic loading can be observed. The plastic strain predicted in the honeycomb legs is shown in Fig. 18. Typically honeycomb crushes axially in a very predictable progressive manner from one end to the other. However as this simulation accurately captures, if the honeycomb crush is not perfectly guided, it will have a tendency to bend back and forth. This honeycomb is guided by an outer casing seen in the left half of Fig. 18 but the compression is not fully constricted. This is what caused periodic streaks of highly compressed honeycomb. While this does not appear to be a problem for the landing sequence, an additional guide rod can be implemented inside each leg to completely constrain this bending.

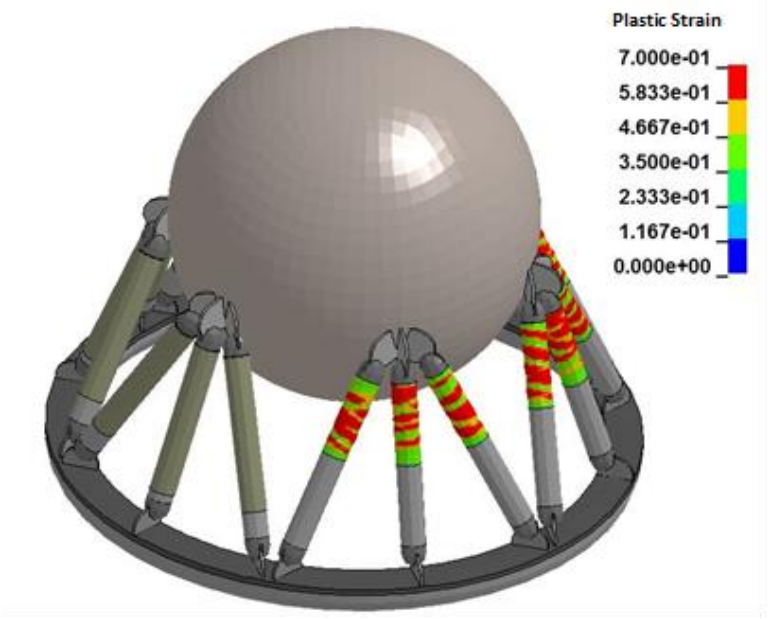

Figure 18 Post impact result of high-fidelity simulation

Verification

Comparisons among values taken from all levels of fidelity are shown Fig. 19 and Fig. 20. By contrasting each of these values, the difference in the lower fidelity models can be found. The *g*-loadings on impact are shown in Fig. 19. The energy balance during impact, where the internal energy measures the amount of energy that was absorbed on impact by both the impact ring and the legs is shown in Fig. 20. Compared to the medium mesh of the high-fidelity model, as can be seen in Fig. 19, the difference of peak deceleration is 4.8% and 1% for the low and medium-fidelity models, respectively. Fig. 20 shows a 3.1% and 1.8% difference for the low-fidelity model's maximum kinetic and internal energy respectively, and a 4% error for both the maximum kinetic and internal energy of the medium-fidelity model. Keep in mind that although the low-fidelity model in Fig. 20 shows time varying values, only the maximum values were calculated. The time-varying values of the low-fidelity model shown in Fig. 20 are there only to represent the expected transition of energy from kinetic to internal.

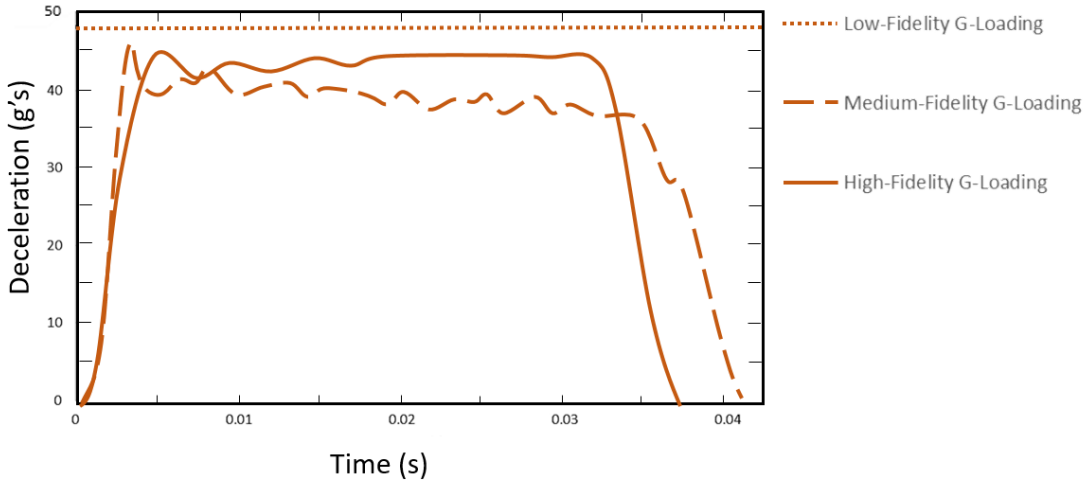

Figure 19 *G*-loading comparison among all three models

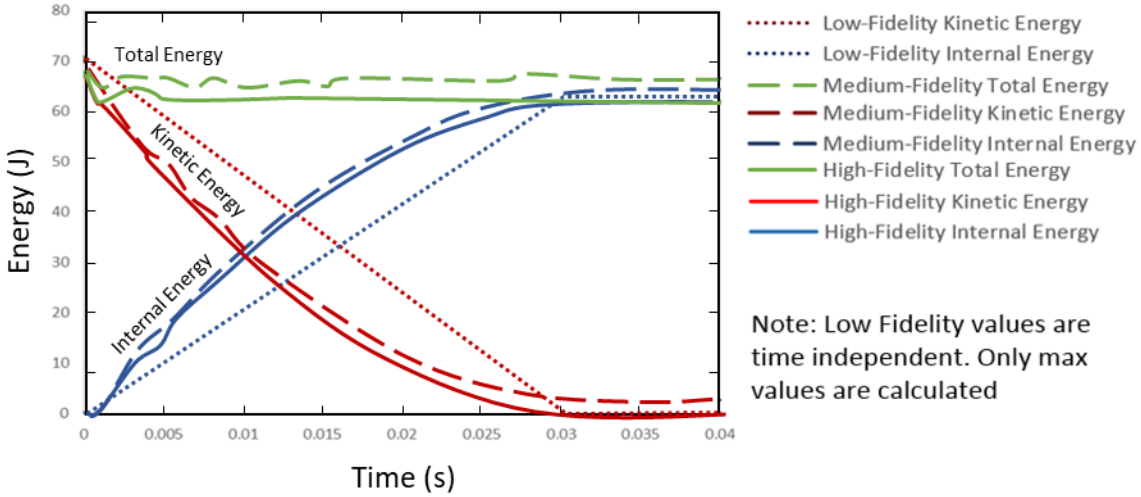

Figure 20 Energy comparison among all three models

Results and Discussion

It has been shown that the developed low-fidelity model is able to predict the landing *g*-loads and energy absorption to within 5% error of the high-fidelity model. This serves to verify the methodology used and enables the use of the low-fidelity model to perform a mass sensitivity analysis. The analysis was broken into three sections: Lander Scalability, Mass Sensitivity, and Leg Configuration Analysis. Each of these sections looked at how the change of certain parameters will affect the overall mass of the lander. For this analysis the preliminary baseline design used for the verification of the multi-fidelity tool was set as a reference point that all changes could be related to. This preliminary baseline was sized so that its mass would be approximately the same as the Venera 9 and 10 landers. The results of the mass sensitivity analysis are dependent on the design assumptions made in this study and thus may vary from that of the original Venera landers. However, by comparing the sizing to that of the original Venera as done in the Lander Scalability section, it can be shown that the original design and new design scale similarly and are still comparable.

Lander Scalability

While the fundamental design of the later Venera landers were the same, there were some changes along the way. The Venera 9 and 10 landers were chosen because they closely adhered to the assumptions made in the lower fidelity models. The Venera 9 and 10 landers mass were 660 *kg* each. Although the mass of the payload cannot be explicitly found in the literature, based on the sizing algorithm found in this work it was approximated that the lander's payload module weighed 260 *kg* (note that for this work the mass of the thermal control system and the pressure vessel was included in the payload's mass).

Lander scalability focused on changing the amount of payload carried by the lander. This is one of the very valuable applications of the geometric constraint solution. As the size and mass of the payload changes, the low-fidelity algorithm scales the lander appropriately. To track these changes, two trends were modeled in Figs. 21 and 22: Constant Payload Density and Constant Payload Size. Constant Payload Density tracks the change of the lander's structural mass as the size and mass of the payload module scale up and down, while the size to mass ratio of the payload remains constant. This trend line captures the scalability of the lander. The second trend line, titled Constant Payload Size, retains a constant payload module radius while increasing the amount of payload mass inside the pressure vessel.

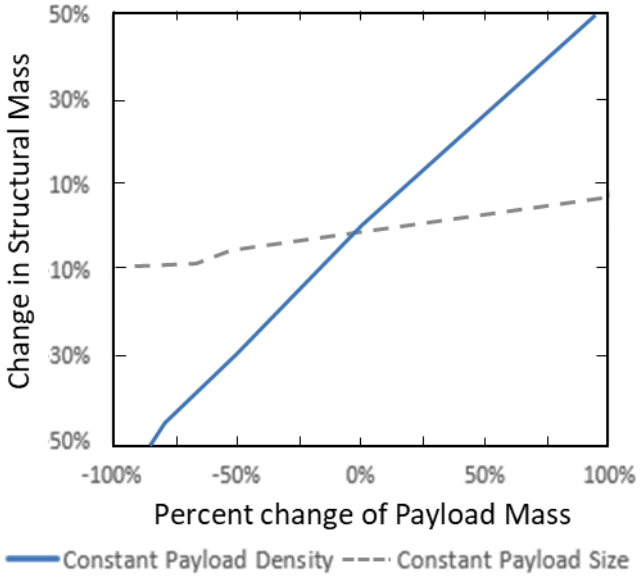

Figure 21 Venera class lander scalability

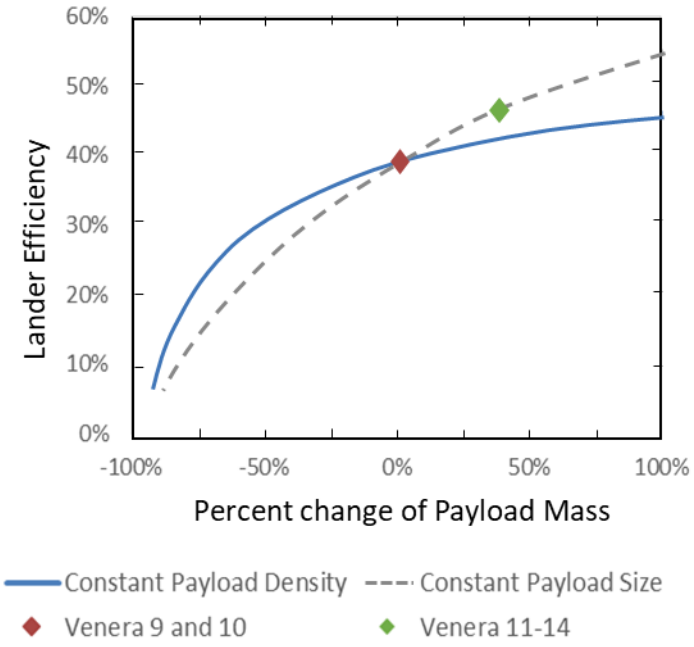

Figure 22 Venera class lander efficiency

As the mass of the payload is increased, the amount of structural support to safely bring it to the surface will also need to increase. This relationship can be seen in in Figs. 21 and 22. For a constant payload density, it can be seen that this lander has a scalability of approximately 2:1. That is that if the payload is increased by 2% the structural mass of the lander will need to be increased by 1%. However, if the payload can be added without changing the size of the payload module the scalability jumps from 2:1 to over 10:1. Venera Landers 13-14 managed to utilize this high scalability ratio by attaching experimental equipment to the outside of the lander. Without

making any major changes to the lander design, an additional 100 *kg* of payload comprised of additional batteries and experiments was added to the Venera 13-14 landers, bring the total mass to 760 *kg* [103].

The ratio of the lander's payload mass compared to the total mass of the lander can be thought of as the efficiency of that lander's design. As the amount of payload increases the efficiency of the lander also increases. This means that this design scales up well but is less effective for smaller amounts of payloads. As seen in Fig. 22, the Venera 9 lander had a lander efficiency of approximately 40%. That is, that the mass of the payload made up approximately 40% of the total mass of the lander. By adding an additional 100 *kg* of payload to the Venera 9 lander, the low-fidelity model predicted the total mass of the latter Venera landers as 772 *kg* which corresponds to the reported values with an error of only 1.6% compared to the actual mass of the Venera 13 and 14.

Mass Sensitivity Analysis

The mass sensitivity analysis was used to reveal the most crucial components of this design. Five of the eight input parameters dealing with the structural design of the lander were varied to see the effect on the lander as a whole. The remaining three parameters are discussed in the next section. The same preliminary baseline design used in the scalability test, was used for the mass sensitivity study. Each of the parameters were individually varied from 10% to 250% of the baseline and the resulting change in the overall mass of the lander was recorded. For example, a 50% change of most design parameters results in less than a 5% change in the overall mass of the lander, that 5% change corresponds to 33 *kg*. While this value is within the range of uncertainty of the mass approximation, however it is noteworthy and the overall trend will be helpful in selecting an optimized baseline design for future missions.

This analysis is highly nonlinear and many variables are interdependent on the others. Therefore, as each component is scaled up and down, the other dependent components will also change in size. For example, if the payload height is increased, the landers stroke will also increase, thus decreasing the radius of each leg and changing the mass of the legs. Because the process is highly coupled, it is possible that scaling one parameter could affect the mass of every other component.

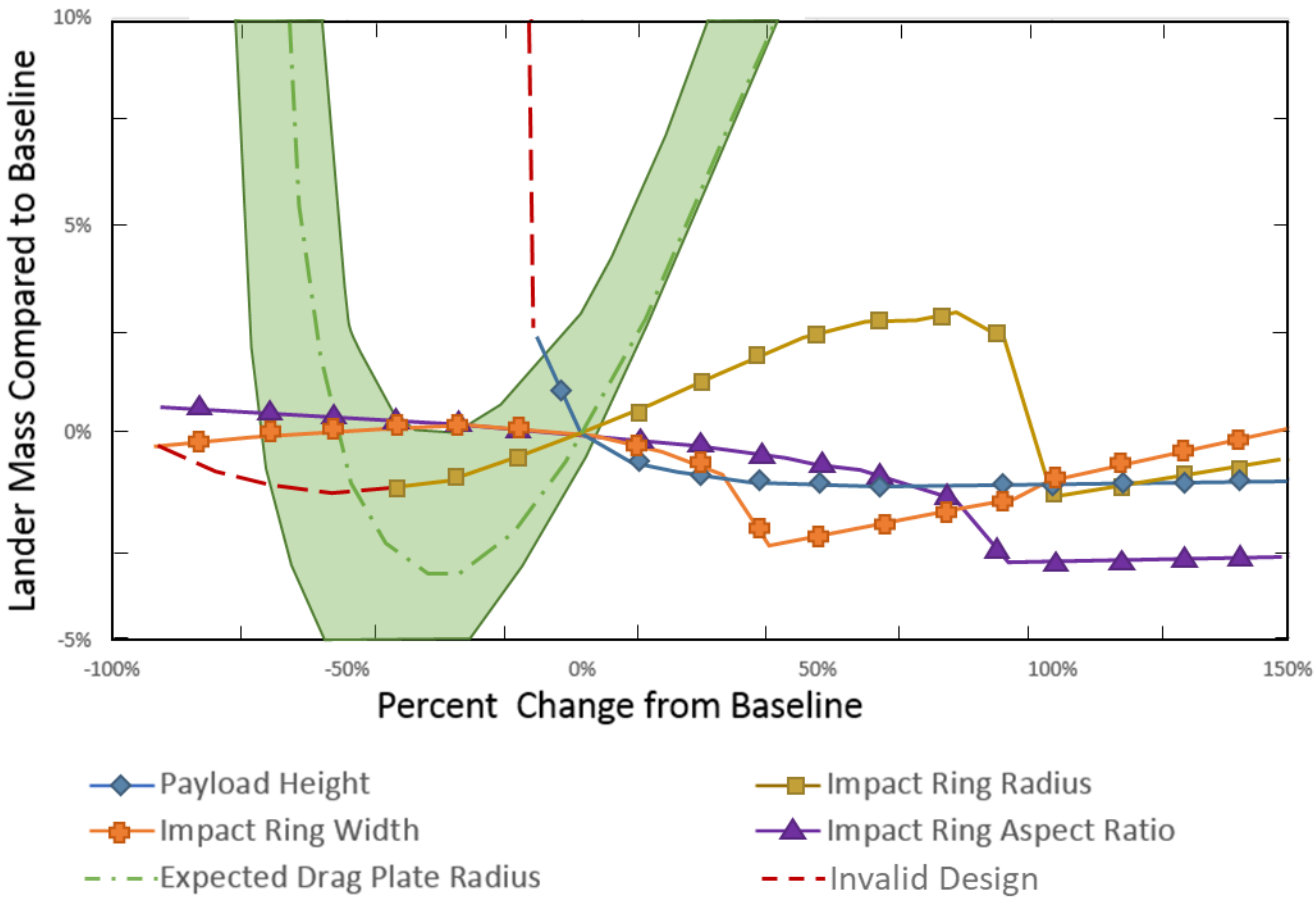

Figure 23 Mass sensitivity analysis

As seen in Fig. 23, the effect the radius of the drag-plate has on the mass of the lander was given a range of expected values. As mentioned previously, the Venera lander had an experimentally found coefficient of drag of at least 0.8 [100]. Any changes to the geometry of the lander will result in a C_D change. The range presented in Fig. 23 shows the upper and lower bounds of the vehicles C_D in shaded green. The nominal result shown by a dashed line was found by varying C_D defined by Eq. (1). The effect the drag-plate radius has on the lander reveals that there is an optimal value. For a small or absent drag-plates, the lander's mass increases to compensate for a higher terminal velocity. This mass increase is a compounding effect as the added mass will additionally increase the landers terminal velocity. It is possible to nullify this compounding effect, as was done by Hall et al. [88], by riding the parachute all the way to the surface, but this approach was not utilized in the baseline design. On the contrary, as the plate radius was increased the terminal velocity monotonically decreased. However, at some point the mass saved by decreasing the landers speed is overcome by the mass used to extend the drag-plate. Matching the optimal plate radius, was found to be one of the primary design drivers for the Venera Class lander design.

The height the payload is above the impact ring has the least effect on the landers mass of any of the other design parameter. However, if the height is too small the lander's mass increases asymptotically, because the stroke of legs is decreased, resulting in significantly bulkier legs and a sharp increase in max *g*-load. After a 10% decrease in height the lander's *g*-load exceeded the mission requirement of 250 *g's*, and this is highlighted with a dashed red line in Fig. 23. While this parameter does not significantly affect the mass of most designs, it does have a significant effect on the lander's tipping stability. As the payload module's location greatly effects the center of gravity (CG) of the vehicle, a higher payload module, though a little lighter, will increase the lander's chance of tipping over if it does not land on a flat surface.

Also note that this trend is only applicable for designs with actuating legs. For designs where the impact ring absorbs all of the kinetic energy on impact, the trend is reversed; increasing payload height will increase mass. In designs like this, the payload module should be as low as it can be while still leaving clearance beneath the payload module to avoid coming into contact with rocks and protrusions that are small enough to fit inside the impact ring.

The impact ring's radius, width, and aspect ratio contribute to how much metallic foam is used on the lander. Each of these parameters have a distinct minimum value as they are increased. These minimums reveal a fundamental characteristic of all Venera Class landers. Each of these minimums occur when the impact ring has enough energy absorbing material to fully absorb the landers kinetic energy with no additional support from the legs. At this point, the mass of the honeycomb in the legs is reduced to zero and the legs no longer actuates. As a result, the lander will experience a significant increase in *g*-load but the expected values will remain well under the mission requirements. This means that while the legs offer some practical benefits, like avoiding payload penetration by keep the pressure vessel away from the ground, they do not efficiently assist in the crashworthiness of the lander. As discussed previously, it is a likely that the original Venera design also did not have any internal energy absorbers although there is some level of debate on that point.

Based on this study, increasing the amount of energy absorbing material in the impact ring, has shown to affect the lander's mass almost as significantly as the drag-plate. For this reason, it was decided that the new baseline will not house any internal energy absorbers in the legs. Thus a simple solid beam can be used as the design of the legs. Additionally, the size of leg joints can be reduced now that the legs are no longer actuating. Overall this change simplifies the design and reduces the total lander mass.

Leg Configuration Analysis

The leg configuration analysis systematically changes both the number of legs and their configuration. The various leg configurations that were tried can be seen in Fig. 24. The top view of a

"radial leg" configuration with 6 legs is illustrated in Fig. 24.a. The top view of an "oblique leg" configuration with 12 legs is illustrated in Fig. 24.b. And the top view of a "tri leg" configuration with 18 legs was illustrated in Fig. 24.c.

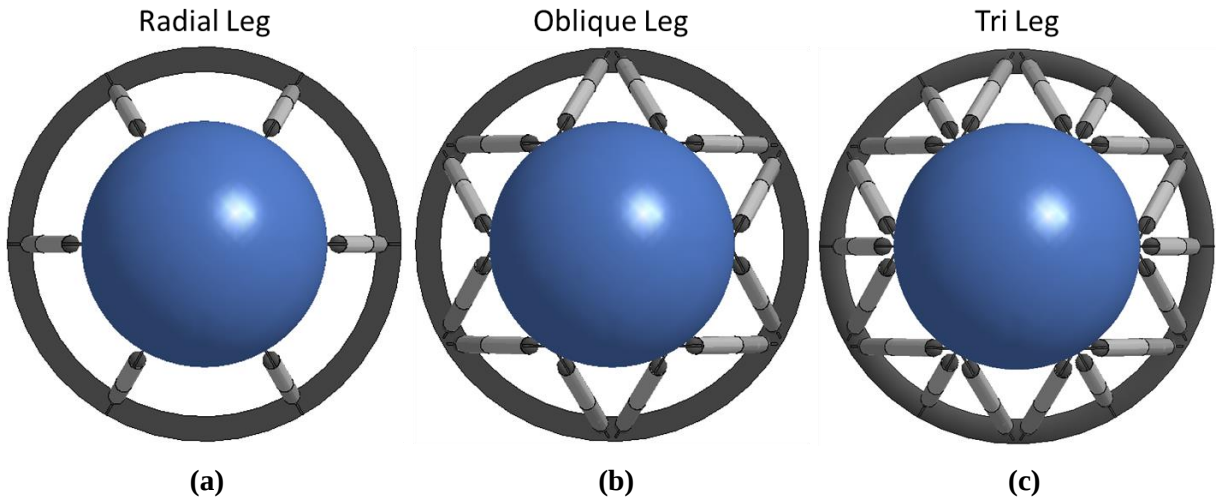

Figure 24 Various examples of leg configuration for Venera Class landers

The leg configuration analysis reveals another significant method to reduce the total mass of the lander. As mentioned previously, the original Venera design had 18 total legs in the tri-leg configuration. As seen in Fig. 25, for the same number of legs there is no major change in the landers total mass for different leg configurations. On the other hand, the total number of legs have a small but notable contribution on the landers total mass.

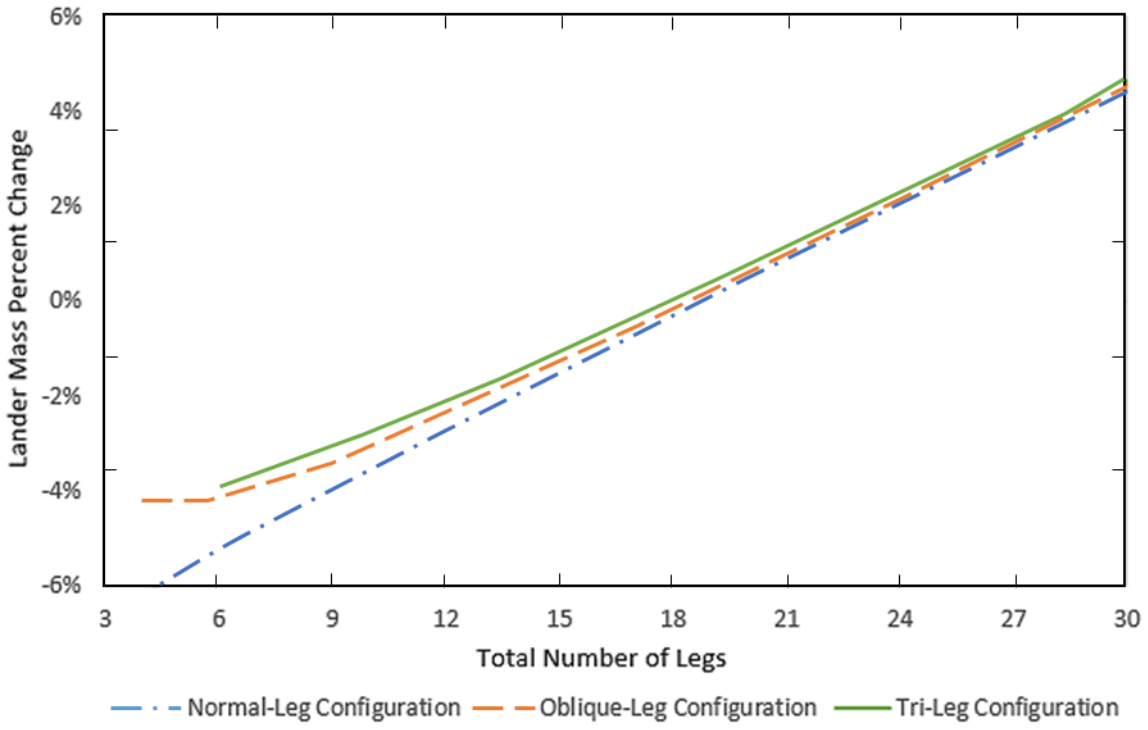

Figure 25 Leg configuration analysis

The original design used as many legs as it did to add a level of reliability to the design. If one leg was to fail the effect would not be as devastating as if there were only 6 legs. However, this added robustness comes at a small cost. As the number of legs are drops, for example in the tri-leg configuration from 18 legs to 9 legs, the total mass savings were approximately 20 *kg*. Of these 20 *kg* more than 15 *kg* were contributed to the removal of the hinges and extra fixtures attached to the legs and not the legs themselves. This explains why the effect seen by changing the number of legs so closely matches the Constant Payload Module Size trend seen in Fig. 25; most of the leg's mass is just added mass. This conclusion combined with results from the mass sensitivity analysis reveal that the leg are one of the components with the largest potential for mass savings.

Comparisons to Published Concepts

To show the capabilities of the low-fidelity model the Venera Class baseline lander, VITaL, from the Venus Flagship Mission Lander [88] was duplicated and the results from the geometric constraint model were compared with published results [20]. The expected entry loads for the original mission was 200 *g's*, more than double the expected landing loads. Smith et al. showed that entry vehicles with high ballistic coefficient, such as ADEPT [4], can be used to reduce the entry loads to the same order of magnitude as the landing loads. For the VITaL mission Smith et al. expected a mass savings of 10-25%. Because the low-fidelity model predicts designs based on landing loads, the results will match results published for the

ADEPT-VITaL mission. However, the original design can be estimated by adding a 20% mass margin to each of the parameters.

Two components in the low-fidelity model required small modifications to accurately model the ADEPT-VITaL lander: the configuration of the legs and the drag-plate. The VITaL lander utilized an oblique leg configuration with 6 leg going to an outer ring and 6 additional legs going to a smaller inner ring. The inner ring is used to transfer load on entry through a snubber to the frame of the aeroshell. It also protects from large rocks that may fit inside the radius of the outer ring. As this inner and outer leg configuration was not studied in the low-fidelity model, the mass of an oblique leg configuration was doubled to capture the additional 6 legs. The drag-plate of the ADEPT-VITaL lander, unlike the baseline model which is a single solid plate, has holes around the circumference of the plate and has 24 support plates above the drag-plate. These holes reduce drag area and thus the effective radius of the drag-plate from 1.250 I to approximately 1.089 I. Based on the size of each support plate, it was estimated that each of the support plate weighed 0.25 *kg*. The mass of the drag-plate used in this calculation took into account the support plates and the holes. The remaining parameters were converted from data provided by Gilmore et al. are shown in Table 2.

Table 2 Design parameters for the VITaL lander [20]

	ADEPT-VITaL	Units
Parachute Capsule	35	*(kg)*
Plate Radius	1.25	*(m)*
Plate Thickness	0.0025	*(m)*
Plate Angle	0	*(deg.)*
Plate Attachment Point	0%	-
Payload Module Mass	150	*(kg)*
Payload Module Radius	0.5	*(m)*
Payload Module Height	0.895	*(m)*
Pressure Vessel FS	2.0	-
Leg Inner Radius	0.0	*(m)*
Leg Casing Thickness	0.005	*(m)*
Leg Attachment Point	10%	-
Impact Ring Radius	1.25	*(m)*
Impact Ring Width	0.16	*(m)*
Impact Ring Thickness	0.177	*(m)*
Support Ring Thickness	0.085	*(m)*
Metallic Foam Strength	0.65	*(MPa)*
Total Number of Legs	12	-
Configuration	Oblique Leg (Inner & Outer)	-
Mass Margin	20%	-
Coefficient of Drag	0.85	-
Total Mass (w/o margin)	811	*(kg)*
Total Mass (w/ margin)	974	*(kg)*

The unlike the new baseline Venera Class lander, the VITaL concept was designed to land in the Tessera regions of Venus. The Tessera regions are areas of high scientific interest and characterized by high slopes. Due to the uncertainty in the terrain, proposed VITaL design was reinforced to handle landings on boulders as large as 1.3 *m* and provides stability for slopes up to 60º. For this to be achieved a very low CG was required. Thus the solid support ring in landing gear was thickened to 8 cm thick. This provides a good foundation for landing on uneven surfaces.

Given the input parameters in Table 2, the low-fidelity code was able to predict the total mass of each component, the terminal velocity of the vehicle, and the impact overloads on the payload. A comparison between the reported and the predicated values are presented in Table 3 for both the VITaL lander and the ADEPT-VITaL lander. Both low-fidelity models yielded percent errors smaller than 5% for most reported values and no values had an error larger than 10%. These levels of error are acceptable as the model has been designed to predict values for various Venera Class lander designs; higher fidelity results can be achieved by customizing the low-fidelity model to the specific lander design. Notice that the Payload Module does not contain the mass of the pressure vessel. Both Gilmore et al. and Smith et al. included the mass of pressure vessel in the Structure section. Thus, the total mass of the payload module is approximately 260 *kg*.

Table 3 Comparison from published results [4,20]

	ADEPT-VITaL	Low-Fidelity Model	Error	VITaL	Low-Fidelity Model	Error
Payload Module** (*kg*)	149.2	149.2	0.00%	174.0	179.0	2.90%
Structure (*kg*)	212.3	212.8	0.24%	283.0	255.4	9.77%
Landing System (*kg*)	452.3	482.3	6.63%	603.0	578.8	4.02%
Total (*kg*)	813.8	844.3	3.75%	1060.0	1013.2	4.42%
Terminal Velocity (*m/s*)	Not Reported	8.36	N/A	9.00	9.16	1.78%
G-Loading (*g's*)	Not Reported	97.9	N/A	83	81.5	1.81%

*** Note: The payload module mass is comprised of scientific experiments, communications, TPS, and power. Unlike other locations in this dissertation, the mass of the pressure vessel is not included*

Selection of a New Baseline Design for Venera Class Landers

Based on these results, the new baseline model for Venera Class landers was chosen. The new design optimizes the lander's components based on a given payload mass of 260 *kg*. The VITaL design was constrained by its landing conditions. In order for the lander to handle slopes of 60°, it has to maintain a wide based and a very low center of gravity. This design was very robust but in order to produce a more mass efficient lander was designed to land on level surfaces. The preliminary design was modeled after the original Venera landers. This design distributed the impact absorbing material between the legs and the impact ring. The new baseline Venera Class lander design was developed by minimizing the mass of the lander subject to geometric constraints of Venera Class landers and a minimum torus radius. The design variables for the preliminary model and the new baseline model are given in Table 4. The values that were bolded are the design variables, all other parameters remained fixed for this analysis.

While the design in Table 4 is a local minimum and does not likely represents the global minimum mass of a Venera Class lander with a 260 *kg* payload module, it does reflect many of the same features that have been discussed previously. The changes are reduction in the payload height, increase in the aspect ratio of the impact ring, and using minimum number of legs (the normal leg configuration was not permitted for this analysis). The two key design features that are shown in Fig. 23 are that the largest drag-plate radius is not the optimal radius and the most mass efficient designs isolate the energy absorbers in the impact ring. Both of these features are also seen in the optimization presented in Table 4.

Table 4 Comparison between the Preliminary Design and the New Baseline designs

	Preliminary Design	Percent Difference	New Baseline
Parachute Capsule (*kg*)	35	-	35
Plate Radius (*m*)	**1.075**	**4.65%** ⇩	**1.025**
Plate Thickness (*m*)	0.0025	-	0.0025
Plate Angle (*degrees*)	**15**	**100%** ⇩	**0**
Plate Attachment Point	**80%**	**22.1%** ⇩	**66.3%**
Payload Module Mass (*kg*)	150	-	150
Payload Module Radius (*m*)	0.5	-	0.5
Payload Module Height (*m*)	**0.650**	**7.7%** ⇩	**0.600**
Pressure Vessel FS	2.0	-	2.0
Leg Casing Thickness (*m*)	0.005	-	0.005
Leg Attachment Point	**27.5%**	**152.7%** ⇧	**69.5%**
Impact Ring Radius (*m*)	**0.9**	**33.3%** ⇩	**0.60**
Impact Ring Width (*m*)	**0.25**	**26.4%** ⇩	**0.184**
Impact Ring Thickness (*m*)	**0.01**	**430.0%** ⇧	**0.057**
Support Ring Thickness (*m*)	0.015	-	0.015
Metallic Foam Strength (*MPa*)	0.65	-	0.65
Total Number of Legs	**18**	**66.6%** ⇩	**6**
Configuration	**Tri Leg**		**Oblique Leg**
Terminal Velocity	7.49 *m/s*	5.07% ⇧	7.87 *m/s*
G-Loading	28.17 *g's*	225.7% ⇧	91.74 *g's*
Leg Inner Radius	0.022 *m*		0.0 *m*
Total Mass	**660.0 *kg***	**25.0%** ⇩	**495.5 *kg***

The new baseline design will serve a benchmark to compare alternative designs against. The TANDEM vehicle that was developed in this work is compared to this baseline as well as the ADEPT-VITaL mission to show its merit.

Chapter 3

The Tension Adjustable Network for Deploy Entry Membrane (TANDEM) Concept

TANDEM is a hybrid of two innovative concepts under active research at NASA: tensegrity robotics and mechanically deployable semi-rigid heat shields. TANDEM uses a similar fundamental concept as ADEPT but replaces the vehicle's internal structure with tensegrity-actuation rover. This provides the same benefits as the ADEPT concept while seamlessly integrating the multifunctional tensegrity infrastructure.

Coupling tensegrity and ADEPT into a single design has significantly more advantages than either concept has separately. Tensegrity actuated deployable heat shields [9,10] have been proposed before, as have tensegrity lander/rovers [11]. However, to date, no one has presented a unified vehicle where one underlining tensegrity structure is capable of handling all of EDLL. The systems-level design approach to the EDLL sequence is what makes TANDEM unique. In most EDL (plus locomotion, if applicable) concepts, each leg of the sequence is handled by a separate system; the heat shield plays no role in landing and the payload (i.e., the rover) is typically considered dead mass until it has actually landed on the surface. In TANDEM, everything is connected to an actively controlled tensegrity frame so that the systems used for landing and locomotion are also utilized in entry and descent. TANDEM brings a new level of controllability to the EDLL sequence without increasing mass.

Concept Overview

TANDEM's lightweight and multifunctional design can be tailored to a variety of missions and is a feasible option for many atmospheric celestial bodies. It's mechanically deployable heat shield, high payload to structural mass ratio, and ability to safely impact the surface at high velocity makes TANDEM a great candidate for the next generation of robotic missions to Mars. Furthermore, its multifunctional capabilities during descent and omnidirectional protection on impact will be invaluable for landed missions to Titan or Venus where the thick atmosphere prevents the development of high resolution surface maps. In view of TANDEM's widespread applications, it was decided that in order to provide an in-depth understanding of the concept, the breadth of the preliminary investigation should be focused on applications

for a single planetary system. To this end, all of the subsequent work will be presented in the framework of a conceptual mission to the surface of Venus. The EDLL sequence for this mission is summarized in Fig. 26.

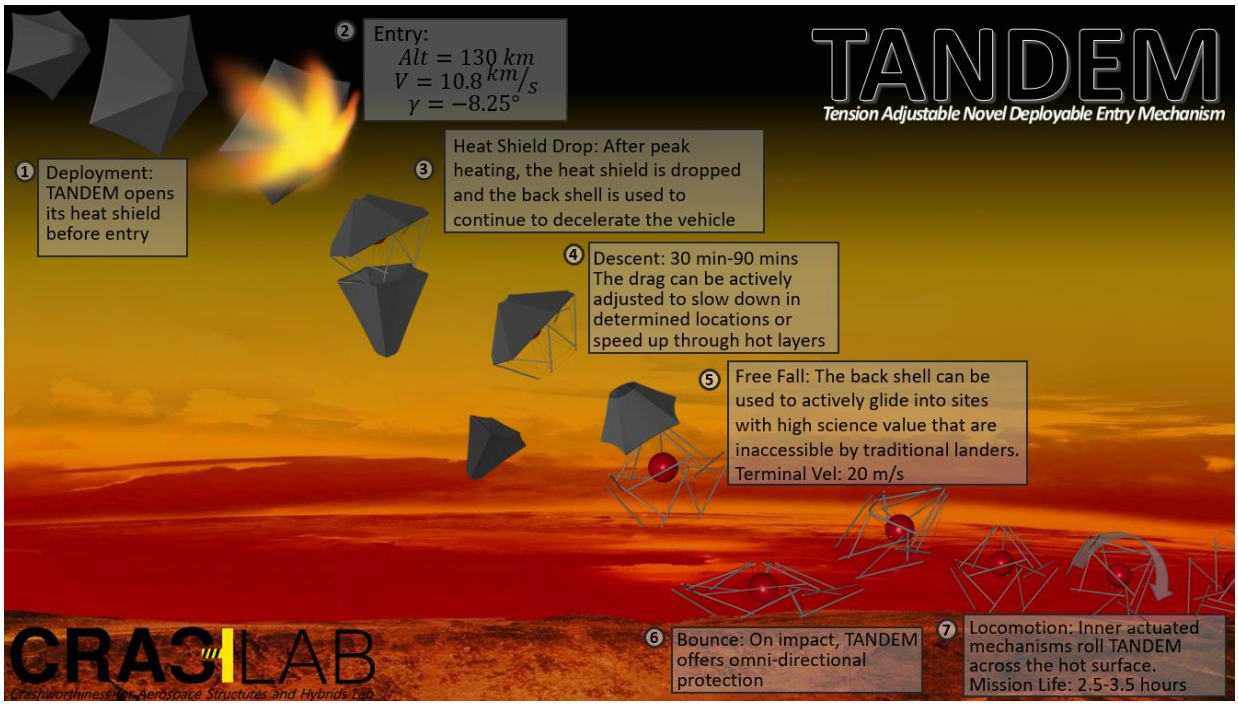

Figure 26 EDLL sequence for TANDEM mission to Venus

For launch and transit, the TANDEM vehicle will be stowed as shown in Fig. 27. Upon arrival, TANDEM will detach from the cruise stage and deploys its heat shield. For simplicity, Fig. 27 visualizes the tensegrity structure and payload module, but the entry membrane and backshell are attached to the tensegrity structure for deployment as shown in Fig. 26.

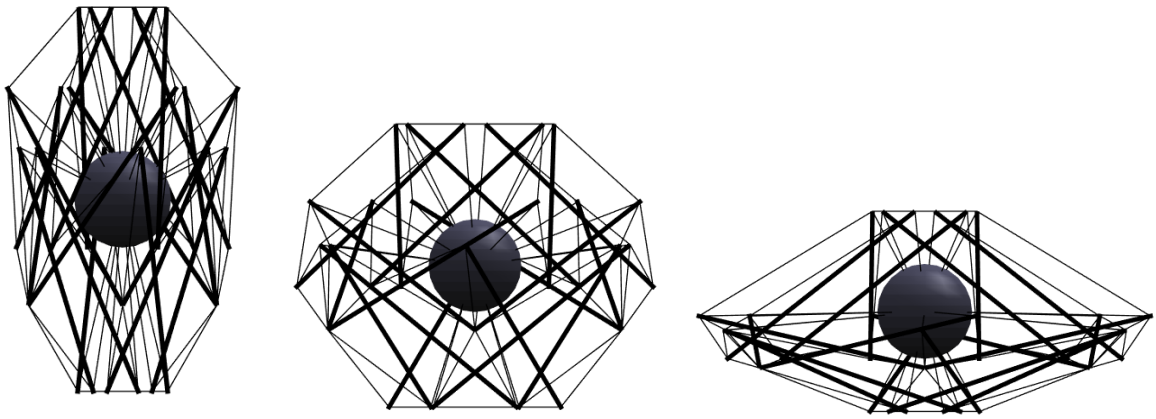

Figure 27 Tensegrity structure changing configurations from stowed to deployed

In addition to TANDEM's low ballistic coefficient, the vehicle has an efficient mechanism to provide lift. Mars Science Lab (MSL) is an example of entry vehicles using a lifting trajectory. MSL achieved lift by using a total of 300 *kg* of ballast mass devices, ejecting the masses to shift the center of gravity of the vehicle. Alternatively, TANDEM is able to achieve lift with little to no mass penalty. The payload module is suspended by a number of cables designed to actuate. This enables locomotion after landing, but can also be used to change the location of the payload module during entry, shifting the CG of the entry vehicle. With an offset CG, the vehicle will create a positive L/D ratio. Additionally, the payload can be shifted laterally in order to direct the lift vector. To ensure stability, the payload module will need to be kept low such that the vehicle's CG is below the aerodynamic center. The lifting entry allows the vehicle to decelerate in the upper atmosphere, maximizing the time spent on descent to collect more data samples than it could on a ballistic entry.

After entry, the TANDEM vehicle will eject the heat shield. The separation of the heat shield and TANDEM vehicle can be initiated by a spring-loaded mechanism. As the heat shield is ejected from TANDEM, it will no longer be able to maintain its deployed radius and will naturally return to a near-stowed, low cross sectional area configuration. There will be little chance of re-connect with the heat shield due to of the difference in ballistic coefficients (mass to drag-area ratio) of the heat shield and the descent stage of the TANDEM vehicle.

The descent stage may be equipped with parachutes to aid with the heat shield separation, but due to Venus's high density atmosphere, parachutes are not required to reach a safe landing velocity. Alternatively, the backshell can be used as a flexible drag device. Because the vehicle begins to heat up during the descent through the Venusian hot, dense atmosphere, it can be advantageous to descend quickly to the surface to maximize the time spent there while still arriving at a safe velocity. This was, to a degree, achieved previously in the Venera campaign by using a reefing cord to constrict part of the parachute. As the vehicle approached the surface, the atmospheric temperature increased, melting the reefing cord and allowing the parachute to fully open [104]. TANDEM is able to add to this concept by actively controlling its drag area. Utilizing the tension network, TANDEM can open and close its flexible backshell to control its rate of descent. This enables a balance between the need for a quick descent and the need of detailed exploration in various areas in the atmosphere that are of scientific interest. The Venus Exploration Analysis Group (VEXAG) has listed the atmospheric formation of Venus as the first goal for Venus exploration [105]. Unlocking the mysteries of the Venusian atmosphere will require a detailed investigation at key altitudes. A regulated descent can be used to maximize the vehicle's scientific investigation during the descent phase without excessively compromising its mission time on the surface. Based on a 10.8 *km/s* entry with a low EFPA and without the use of a parachute, it was found that the incorporation of the flexible

backshell into an EDLL profile will create a range of descent times from as low as 25 minutes to as long as 2 hours. Figure 28 shows the full range of descent trajectories that can be explored with TANDEM.

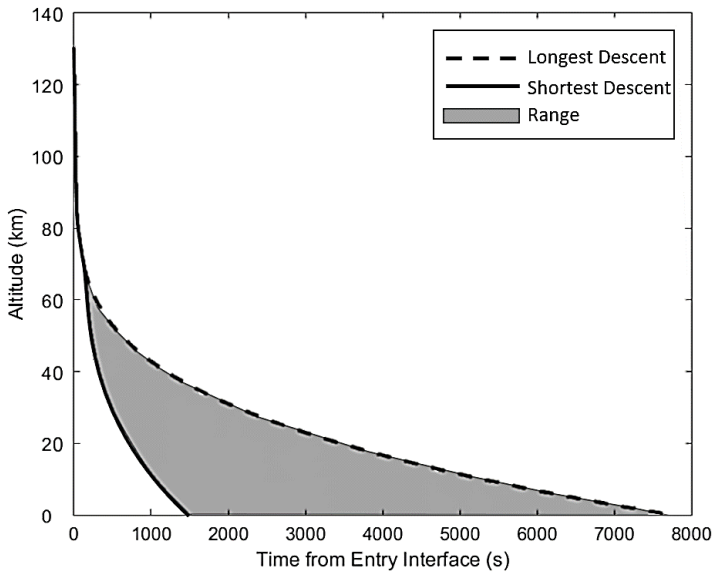

Figure 28 Range of descent trajectories with the active control of the flexible drag-plate

When the vehicle is nearing its desired landing site, the flexible backshell can be adjusted to achieve pinpoint landing. The use of the backshell is analogous to how a parachutist can navigate to a specific landing site by pulling on cables to change the shape of the parachute. In the same way, controlling the shape of the flexible backshell can also be used as a simple form of hazard avoidance that can open up higher risk landing regions.

Once the vehicle is in the desired landing zone, the backshell can be released, allowing the rover to free fall to the surface. Depending on the ballistic coefficient for the specific mission, the terminal velocity for Venus applications could range from 15 to 30 *m/s*. Due to the large shock dissipating capability of tensegrity structures, TANDEM can be designed such that the landing overloads on the payload will be approximately the same *g's* experience on entry. However, the entry loads endure over a much larger time-scale compared to the impulsive landing loads. This suggest that the onboard equipment will likely be able to handle a larger peak loading on impact than those experienced on entry.

Like most spherical tensegrity concepts, TANDEM inherently provides omnidirectional protection on impact. Even if it impacts on a large boulder or a very uneven and sloped surfaces, TANDEM will survive with no complications. Omnidirectional impact protection opens up a host of landing sites, including Venus's Tessera regions, which are too hazardous or too steep for traditional landers. Additionally, due to the unique shape altering capability of the TANDEM lander, the outer circumference

of the vehicle can be actively adjusted while the payload module position can be altered to provide the optimal landing configuration for various landing scenarios. With its shock dissipating capability and omnidirectional protection, TANDEM provides a high level of reliability and safety to the mission.

As soon as the vehicle lands, it can begin traversing the surface. The tensegrity framework provides TANDEM with a more organic method of locomotion when compared to traditional wheeled rovers. Tensegrity landers have a more diverse range of mobility, including rolling, sliding, bouncing, walking, and jumping, that cannot be safely performed by a traditional rover. These new modes of locomotion open up high-risk terrains for future missions. Additionally, previous missions have shown that immobility presents an additional risk to the mission. As an example, the Venera 14 lander detached one of its lens caps directly under where the soil densitometer was designed to sample, thus significantly interfering with the experiment [106]. With TANDEM, these unexpected interferences can be avoided. While the investigation of various modes of transportation are outside the scope of this preliminary investigation, a proof of concept locomotion demonstration is provided in Chapter 6 as well as an investigation of advanced gait development strategies for tensegrity structures.

Extreme Environment Component Design

The TANDEM vehicle can be broken into four basic components: The semi-rigid heat shield, the flexible backshell, the tensegrity structure, and the payload module. The following section provides a brief overview of these components. Many of the details mentioned in this section are mission dependent and can be altered based on the requirements and destination of each mission. A fuller discussion of the design process used for the conceptual mission developed in this study is discussed in Chapter 7.

The semi-rigid heat shield, when fully deployed, is a 4.5 *m* diameter sphere-cone with a 70° degree cone angle. The nose of the shield is rigid and can be covered with a conventional TPS while the deployable components utilize a 3D woven carbon fabric. The carbon fabric has been arcjet tested based on the mission requirements of the ADEPT-VITaL mission [37] up to 250 W/cm^2. The backshell is not exposed to the same aerodynamic and aerothermodynamic loads as the heat shield but it may still necessary to protect the aft of the vehicle during entry. As a result, there is a wider range of appropriate materials for its use. The nominal selection of backshell material for this analysis will be carbon fabric.

The tensegrity structure itself is comprised of 18 hollow titanium compression members and 78 individual titanium cables that comprise the tension network. Each rod in the structure has an ultra-high-temperature and pressure motor [107] at either end which is used to spool in lengths of cable to control the configuration of the structure. In the center of the tensegrity structure is the payload module, an insulated pressure vessel used to protect the scientific equipment from the harsh environment. All of TANDEM's

scientific equipment, control systems, and communications are housed inside of the payload module. This enables the uses of standard electronics for operation at Venus surface conditions (VSC). However, it also limits the lifespan of a mission. Because the payload houses so many mission critical systems, an ongoing work aims at increasing the operating temperature for several of the internal components. By reducing the number of components in the pressure vessel, the overall mass will significantly drop.

The implementation of an external pressure vessel as the central payload module was first utilized by the Soviet Union for the Venera missions [27] and is now common for new mission concepts [20,88–90]. However, housing these critical components inside of an external pressure vessel can be risky during landing or locomotion, in case the vessel strikes the ground. Additionally, in environments akin to VSC, this practice presents further risks to the mission by limiting the mission lifetime to the time required for the payload to reach its maximum operating temperature. In these conditions, the payload must endure not only the thermal waste of its internal electronics but also the extreme external temperatures.

As can be seen in Eq. (2), the thickness of the payload module is proportional to its radius. Thus, as the payload module increase in size, the mass of the pressure vessel increases cubically. Although it is largely unavoidable, the current practice of utilizing an insulated pressure vessel both limits the amount of equipment and increases the total system mass. By developing TANDEM's electrical and electromechanical components to operate in extreme environments, some of the internal components could be moved outside of the payload module. This would reduce the thermal load and the required size of the payload module for a TANDEM concept, thereby reducing mass, dispersing the locations of mission critical components, and extending mission life by decelerating the accumulation of thermal waste.

The current design of TANDEM utilizes standard electronics with a maximum operating temperature of $35°C$. The TPS was designed keep the payload module under that threshold for 3 hours after entry [20]. An ongoing investigation looks at the incorporation of high-temperature electronics to enable the removal of components from the payload module. The rest of this section explore various components that can be designed to survive at VSC. The electronics of components that can be removed from the payload module can be fabricated using SiC based electronics [108], while components that must remain inside the payload module can be designed to operate at elevated temperatures by the incorporation of silicon on insulator (SOI) electronics [109]. These are discussed in order of current high-temperature TRL and benefits for removal from the payload module: motors, batteries, scientific instruments, data storage, and control systems.

Motors and Batteries

While an under-actuated TANDEM vehicle could be controlled from within the payload module, the batteries and motors produce significantly more thermal waste than any of the other components, limiting the mission life from thermal waste. Additionally, creating a seal that allows the cable to be drawn through the wall of the pressure vessel presents a substantial design problem, especially at VSC. Therefore, batteries and motors are the most important components to develop a high-temperature counterpart for.

Fortunately, the required components currently exist at high levels of technology readiness. Honeybee Robotics has developed various stepper and brushless DC motors for extreme environments [107]. These motors have been tested over a large temperature range (20-460˚*C*), so they are a feasible selection for TANDEM, which requires operation above the entry interface as well as on the surface. The required electronic motor controller will be addressed below under the Data Storage heading.

Batteries provide a more significant challenge. Landis provides a detailed overview of high-temperature battery systems that already exist [110]. The limiting factor with current technologies is that they require elevated temperatures before they become operational. Sodium-sulfur batteries, for example, only operate above the melting point of sulfur, 240°*C* [110]. This means that the power system would not start operating until after the vehicle descends below an altitude of at least 65 *km*.

Three potential solutions to provide an adequate power source are discussed and compared. Further investigation of these options will be addressed in future work. The first solution is to simply keep all of the batteries inside the payload module. This solution will act as the baseline case since it does not require any technology development. Keeping the batteries inside the payload is not preferred, as it results in a higher overall vehicle mass and increased thermal accumulation rate. Additionally, this method requires electrical leads to be embedded into each tension cable in order to transmit the power to each externally mounted motor.

The next alternative solution separates the power system required for the heat shield deployment from the additional system used for surface locomotion. This strategy may be partially required, due to the dichotomy of required torque for locomotion versus deployment. Because deployment of the heat shield also requires the entry membrane to be pretensioned, the high-temperature motors may not be able to provide enough torque to deploy the heat shield. To resolve this, an additional motor and spring-loaded system has been included in the design of the aeroshell that has the sole purpose of assisting the pretensioning of the aeroshell. The proposed solution will allow the tensegrity motors to remain inactive and only utilize the aeroshell motor to transition from the stowed configuration to the deployed configuration. This method is still suboptimal, as it doesn't take advantage of the functionality of the

vehicle; the multifunctional infrastructure will be inactive during entry and initial stages of descent. It is possible to harness the heat generated from entry to active the motor in the upper atmosphere. However, it is not immediately clear how to efficiently transfer the heat to every motor in the tensegrity structure. Yet, this solution will successfully remove the motors and batteries from the payload module, thus extending the mission timeline and potentially reducing the total mass of the system.

Finally, it may be possible to heat the battery before deployment. This is a common practice for thermal batteries, which have operational temperatures corresponding to VSC [110]. While thermal batteries will not be used in this mission due to their short service time, similar pyrotechnics may be used to initially heat up the batteries for operation during deployment and descent, and then the high atmospheric temperatures will keep the batteries at operating temperatures for locomotion. This solution provides the best characteristics but requires further investigation to confirm its feasibility.

Scientific Instruments

The most sensitive components in the payload module are the scientific instruments. Although many of the instrument suites proposed for Venus landers are not designed to operate at VSC, NASA Glenn has developed a number of sensors and instruments that are functional at such conditions. Some of the developed high-temperature sensors include pressure and temperature sensors, electric nose sensors (which can be doped to be sensitive to various chemical compounds), strain sensors (which could be used for feedback control of the vehicle), as well as Microscale Particulate Classifiers (MiPAC) [111]. Such instruments will be useful for characterizing the environment around the landing site and can be used to answer the Decadal Survey's questions about Venus. Further investigation will be made into additional components that can be exposed to the VSC for scientific exploration of Venus.

Data Storage, Avionic, and Control Systems

Due to a large number of degrees of freedom (DOF), the control systems required for tensegrity robotics are highly complex. Despite this, Mirletz et al. [57] have produced an effective strategy for producing various gaits, through the use of a Neural Network and machine learning algorithm. Although the capability for control exists, the data storage required to hold an on board library of various gait and control strategies may surpass the current state of the art for high-temperature SiC components [108]. For this reason, the on board computer required to make calculations for each scenario in real time will have to remain inside the insulated payload module.

Investigations will focus on SOI or similar matrices to improve the maximum operating temperature of the computational and data storage systems from the standard limit of 60°C to the military grade of 125°C or higher. Many systems exist now that can achieved temperatures as high as 230°C in

some studies, with the near term developments aimed at over 300°C. While this does not allow the vehicle to remain operational indefinitely, it will significantly extend the mission lifetime compared to the baseline design.

Less complicated systems, such as electronic motor controllers, can be designed to operate at VSC. In fact, the electronic controller has already been developed for the Honeybee motor and is included in the design of each tensegrity strut. A required technology needed to be developed is a radio frequency (RF) transmitter/receiver capable of operating at VSC. The short range RF transmitter and receiver will enable wireless communication from the on-board computer to the motor controller, simplifying the mechanical design of the vehicle by removing the wiring required to control each motor.

Current high-temperature RF circuits using off-the-shelf Gallium Nitride (GaN) high electron mobility transistors (HEMTs) [112–115] are under development. This systems were intended for downhole communications for oil and gas exploration, however this technology can be leveraged for extreme environment exploration. Existing RF systems for downhole communications can operate at most at 150°C with maximum data rate of about 4 Mpbs [116]. Alternatively, it is believed that the development of a high-temperature RF system capable of operating at 500°C, can be developed by leveraging SiC or SOI/CMOS (Complementary Metal Oxide Semiconductor) technology, as they have shown to operate at high-temperatures [108]. However, SiC and SOI technologies cannot operate at high frequencies due to low unity-gain frequency.

The design and development of these ultra-high-temperature and pressure components are outside the scope of this work, but have been identified as required/desired technologies for this mission. While the development of these technologies will streamline the design, they are not mission critical and the proposed concept can be designed to function without them.

Chapter 4
TANDEM Systems Analysis Tool

A systems analysis tool was developed to aid in the design of a mission utilizing the TANDEM concept. This tool analyzes key parameters of the vehicle during its EDLL sequence. The analysis tool uses a 3-DOF flight mechanics code as its backbone with additional modules integrated into it. Throughout the various stages, a tensegrity form finding algorithm is used to solve for the static configuration of the vehicle. During the entry stage, the tool investigates the aerodynamics and aerothermodynamics using the modified Newtonian method and surrogate convection and radiation models. Because all of these are low computational-expense methods, a large number of different entry and descent sequences can be analyzed rapidly. Landing and locomotion were analyzed by integrating outside codes into the analysis tool. LS-Dyna's explicit finite element solver was used for impact simulations, and the NASA Tensegrity Robotics Toolbox (NTRT) was implemented for locomotion analysis and control. An overview of the systems analysis tool is provided in Fig. 29 while additional information on each of the modules is provided in the following sections.

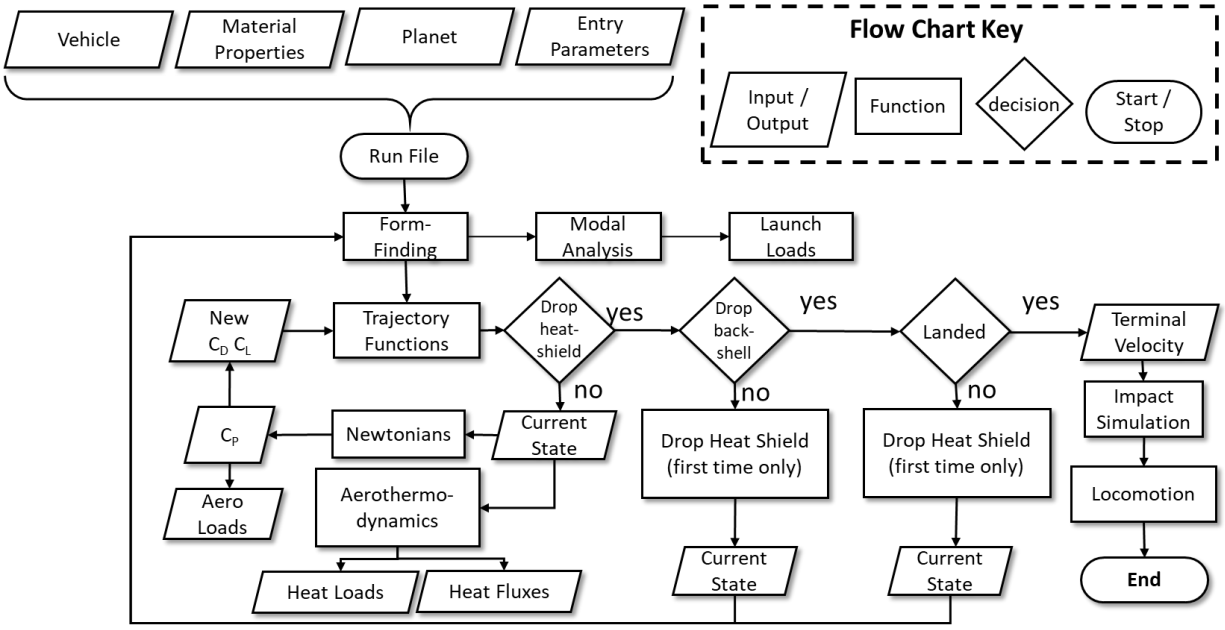

Figure 29 TANDEM systems analysis tool flowchart

Trajectory Functions

A 3-DOF trajectory flight mechanics code (FMC) was developed to calculate the trajectories used in this dissertation. The FMC used the Runge-Kutta method with a 5th order accuracy using Matlab's ODE45 function [117] to integrate the system of ordinary differential equations (ODEs) seen in Eq. (7)

$$\begin{aligned} \frac{dV}{dt} &= -\frac{D}{m} - gsin(\phi) \quad V\frac{d\phi}{dt} = \frac{L}{m} - \left(g - \frac{mV^2}{R_v}\right)\cos(\phi) \\ \frac{ds}{dt} &= \frac{R_P}{R_v}Vcos(\phi) \qquad\qquad \frac{dR_v}{dt} = Vsin(\phi) \end{aligned} \tag{7}$$

where V is the vehicle's velocity, ϕ is the flight path angle relative the local horizon, s is the downrange distance or the tangential position projected on the surface of the planet, R_v is the radial position, R_p is the radius of the planet, L is the lift force, D is the drag force, m is the mass of the vehicle, g is the altitude varying gravitational acceleration, and t is time. Together, these equations define a state vector consisting of the position, velocity, and orientation of the vehicle throughout its entry and descent through the atmosphere.

The aerodynamic loads and aerothermodynamics are determined from the state parameters defined after each time step of the Runge-Kutta integration. The aerodynamic loads are estimated using the modified Newtonian method, which uses the Mach number, atmospheric specific heat ratio, and the vehicle geometry to estimate the pressure, lift, and drag coefficients. During the hypervelocity entry phase, the coefficients are updated at each time step. The modified Newtonian method approximates the flow over the vehicle as a purely inviscid stream of particles. This assumption reduces the calculation of the aerodynamic loads to a simple algebraic equation. This method has been shown to provide accurate approximations for hypersonic and supersonic speeds [118]. A complete derivation of Eq. (8) can be found in Anderson's textbook [119].

$$C_p = C_{p_{max}} \sin^2\theta \tag{8}$$

In Eq. (8) C_p is the coefficient of pressure at a point on the vehicle's surface, $C_{p_{max}}$ is the C_p at the stagnation point and θ is angle between surface normal and freestream. The coefficient of pressure at the stagnation point can be derived as a function of Mach number and specific heat coefficient from the Rayleigh Pitot relation. This is shown in Eq. (9)

$$C_{P_{max}} = \frac{2}{\gamma M^2}\left[\left(\frac{M^2(\gamma+1)^2}{4\gamma M^2 - 2(\gamma-1)}\right)^{\frac{\gamma}{\gamma-1}}\left(\frac{1-\gamma+2\gamma M^2}{\gamma+1}\right) - 1\right] \tag{9}$$

where M is the current Mach number and the specific heat ratio γ is 1.286 for Venus atmosphere [120]. With the C_p of the current time step known, the pressure and aerodynamic load on the vehicle can be solved at any point in the exposed flow field using Eq. (10)

$$p - p_\infty = \frac{1}{2} C_p \rho_\infty V_\infty^2 \tag{10}$$

where p is the aerodynamic pressure, p_∞ is the freestream pressure which is negligible in most cases, ρ_∞ is the freestream density, and V_∞ is the freestream velocity. The drag D and lift L are simply the normal and tangential components of the total aerodynamic load, respectively. From that, the C_D and C_L of the current time step can be calculated using Eqs. (11) and (12). The updated lift and drag coefficients are then applied to the trajectory equations, Eq. (7), for each time step.

$$C_D = \frac{D}{2S\rho_\infty V_\infty^2} \tag{11}$$

$$C_L = \frac{L}{2S\rho_\infty V_\infty^2} \tag{12}$$

The freestream velocity, V_∞, is a state variable, The surface area is a function of geometry, and the atmospheric density, ρ_∞, is found as a function of altitude. The atmospheric data reported by Pioneer Venus [121] are seen in *Table 5* are used for these calculations. However, this tool has been programed with alternative planetary properties and atmospheric model which will enable it to work for any other planet as well. The additional baseline atmospheric models for the other planets was provided by Justus and Braun [120].

Table 5 Atmospheric density as a function of altitude

Altitude (*km*)	Atmospheric density, ρ (kg/m^3)	Speed of Sound, (*m/s*)	Altitude (*km*)	Atmospheric density, ρ (kg/m^3)	Speed of Sound, (*m/s*)
0	65.60	596	100	6.95×10^{-5}	214
5	49.80	581	105	1.93×10^{-5}	217
10	47.30	565	110	5.58×10^{-6}	220
15	27.90	544	115	1.67×10^{-6}	223
20	20.30	523	120	5.20×10^{-7}	226
25	14.40	501	125	1.67×10^{-7}	229
30	9.89	479	130	5.52×10^{-8}	232
35	6.34	466	135	1.88×10^{-8}	234
40	3.96	452	140	6.60×10^{-9}	237
45	2.46	430	145	2.30×10^{-9}	247
50	1.46	407	150	8.74×10^{-10}	256
55	0.868	362	155	3.61×10^{-10}	264
60	0.381	354	160	1.57×10^{-10}	272
65	0.161	345	165	7.38×10^{-11}	275
70	6.53×10^{-2}	243	170	3.52×10^{-11}	278
75	2.75×10^{-2}	234	175	1.93×10^{-11}	282
80	9.80×10^{-3}	225	180	9.33×10^{-12}	285
85	3.04×10^{-3}	216	185	5.02×10^{-12}	289
90	8.62×10^{-4}	216	190	2.64×10^{-12}	293
95	2.45×10^{-4}	215	195	1.24×10^{-12}	296
100	6.95×10^{-5}	214	200	5.85×10^{-13}	300

Aerothermodynamics

The aerothermodynamics are a nontrivial value to calculate. Thus, surrogate equations are used to estimate the convective and radiative heat flux experienced by the vehicle during atmospheric entry. These equations provide the stagnation-point heat fluxes for an axisymmetric blunt body in arbitrary gases at chemical equilibrium. The surrogate equations are tuned to match empirical data or values predicted by higher fidelity models, as functions of only the vehicle's velocity, nose radius, and the atmospheric density as seen in Eq. (13)

$$Q = KV_{\infty}^{a}\rho_{\infty}^{b}R_{n}^{c} \quad (13)$$

where R_n is the nose radius of the vehicle. The constants K, a, b, and c are selected to match different entry conditions and vehicle parameters. Multiple surrogate equation constants, shown in *Table 6* for convection heating and *Table 7* for radiation heating, were reviewed for this step of the analysis to ensure that the results were reasonable and conservative.

Table 6 Convective heating surrogate equation constants

Author	K	a	b	c
Sutton and Graves [122]	$1.896\text{x}10^{-4}$	3	0.5	-0.5
Scott et al. [123]	$1.1547\text{x}10^{-4}$	3.05	0.5	-0.5
Tauber, Bowles, and Yang [124]	$1.35\text{x}10^{-4}$	3.04	0.5	-0.5

Table 7 Radiation heating surrogate equation constants

Author	Range	K	a	b	c
Park and Ahn** [125]	All	$2.787\text{x}10^{-67}$	19	1.05	0.2
Craig and Lyne [126]	$12\ km/s > V_{\infty} > 10\ km/s$	$3.07\text{x}10^{-44}$	13.4	1.2	0.49
	$10\ km/s > V_{\infty} > 8\ km/s$	$1.22\text{x}10^{-12}$	5.5	1.2	0.49
	$V_{\infty} < 8\ km/s$	$3.33\text{x}10^{-30}$	10	1.2	0.49
Tauber, Palmer, and Prabhu [127]	$12\ km/s > V_{\infty} > 10\ km/s$	$8.497\text{x}10^{-63}$	18	1.2	0.49
	$V_{\infty} < 10\ km/s$	$2.195\text{x}10^{-22}$	7.9	1.2	0.49

***NOTE: For simplicity the normalized pyrolysis-gas injection rate was assumed to be 0. This will provide the most conservative approximation*

.

There was very little variation between the various convection models, however, Sutton and Grave's model was selected for the convection calculation. Sutton and Graves's model is unique in its capability to be used for various atmospheric bodies [122]. The constant K in their model was derived from the constituents of the atmosphere and is predefined for various atmospheric bodies in the solar system. The ability to develop a new heating constant for an arbitrary gas will be utilized further in future work, which will analyze the merit of TANDEM on other planetary bodies. Meanwhile, the radiation calculation constants were selected to be the Tauber, Palmer, and Prabhu model because its assumptions match better than the Craig and Lyne model, and it provided a more conservative heat load compared to the Park and Ahn model. Figure 30 shows the convective and radiative heat fluxes at the stagnation point during entry for a vehicle with a nose radius of 1.125 *m* entering at 10.8 *km/s*.

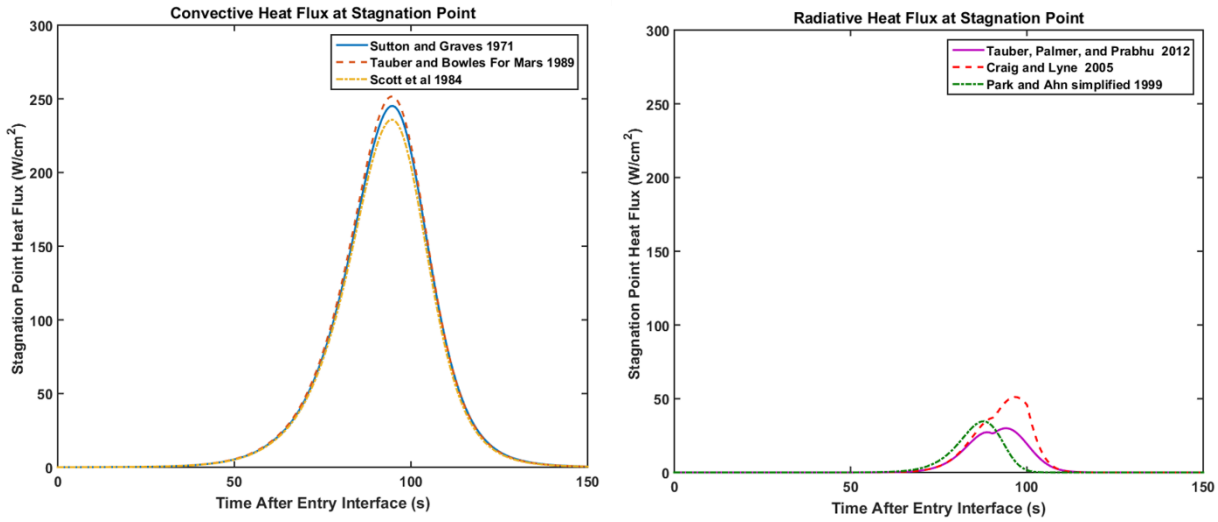

(a) (b)

Figure 30 Comparison of various aerothermodynamic surrogate models for (a) convective heat flux and (b) radiative heat flux

After the vehicle has passed a threshold altitude or acceleration value is reached, the heat shield is released. This transition is approximated by a C^1 discontinuity in the trajectory calculations (i.e. a discontinuity in the derivative of the position function). The vehicle's mass and ballistic coefficient are changed as the heat shield is released. This reflects the descent stage of the EDL sequence where the vehicle is decelerated by the flexible backshell or parachute. In this stage, the Newtonian method is no longer applicable and thus a user defined C_D and C_L must be supplied. An additional C^1 discontinuity can be included to capture the release of the backshell before landing in order to calculate the terminal velocity of the vehicle.

With all of the different modules of the entry analysis developed, a parametric entry study was performed to better understand how TANDEM operates on entry. Several hundred trajectories were rapidly solved for in order plot the relationship between ballistic coefficient and EFPA. Figure 31 shows the results of this study for an entry vehicle with a nose radius of 1.125 m entering the Venusian atmosphere with a variety masses (i.e. ballistic coefficients) and EFPA. Contour-lines for maximum deceleration, peak heat flux, and total heat load are shown. As can be seen in the figure, the maximum entry load on the vehicle is almost highly dependent on the EFPA; the higher the angle, the higher the aerothermodynamic and atmospheric loads. The same trend with was described in Chapter 1 was also seen in this study. For a given ballistic coefficient, increasing the EFPA to near the skip-out range will decrease the peak heat flux of the vehicle but will drastically increase the total heat load that must be withstood, as seen by traveling from

point “A” to point “B”. It can also be seen that a decrease in max deceleration and peak heat flux can be achieved while maintaining a nearly constant total heat load if the vehicle’s EFPA as well as its ballistic coefficient is reduced, from point “A” to point “C”. This represents the change that is enabled with the TANDEM entry vehicle design. In this specific example the total heat load increased by a couple hundred *J/cm²* from “A” to “C” but this will not significantly affect the lander’s mass compared to the several *kJ/cm²* increase from “A” to “B”

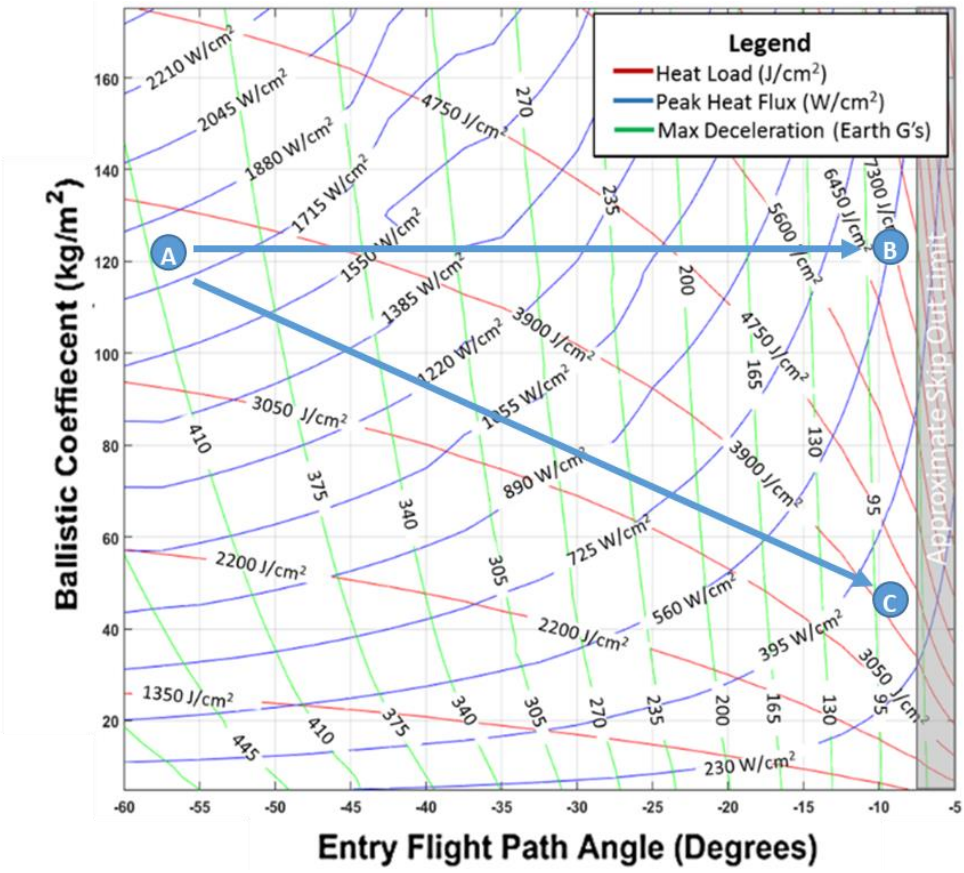

Figure 31 Ballistic coefficient parametric study as a function of entry flight path angle for ballistic entry. Velocity at entry is 10.8 km/s with a vehicle nose radius of 1.125 m

Stable Tensegrity Configuration Selection

When the vehicle reaches an altitude of zero, the flight mechanics code stops and the final velocity of the vehicle is recorded for use in the landing simulation. The landing simulation utilizes an explicit finite element code to simulate the vehicle impacting on a rigid surface. Because the stiffness of a tensegrity structure is closely dependent on its configuration, it is necessary to use a form-finding algorithm before creating the finite element (FE) model to ensure that the structure is in a stable configuration. If the structure is not in an appropriate configuration, the structure will be either be unable to hold a load or will be too stiff resulting in high *g’s* on the payload module.

Tensegrity Equilibrium Equations

In order to discuss the selection of an appropriate equilibrium configuration, it is necessary to discuss the equilibrium equation for tensegrity structures. Figure 32 shows a simple 2D tensegrity structure. The structure is in a state of pretension such that the rods $\overline{ik}$ and $\overline{hj}$ are subjected to a compressive load and the tension members $\overline{hi}, \overline{ij}, \overline{jk}$, and $\overline{kh}$ are in tension. Note that members $\overline{ik}$ and $\overline{hj}$are two separate "two-force members" and do not interact directly with each other.

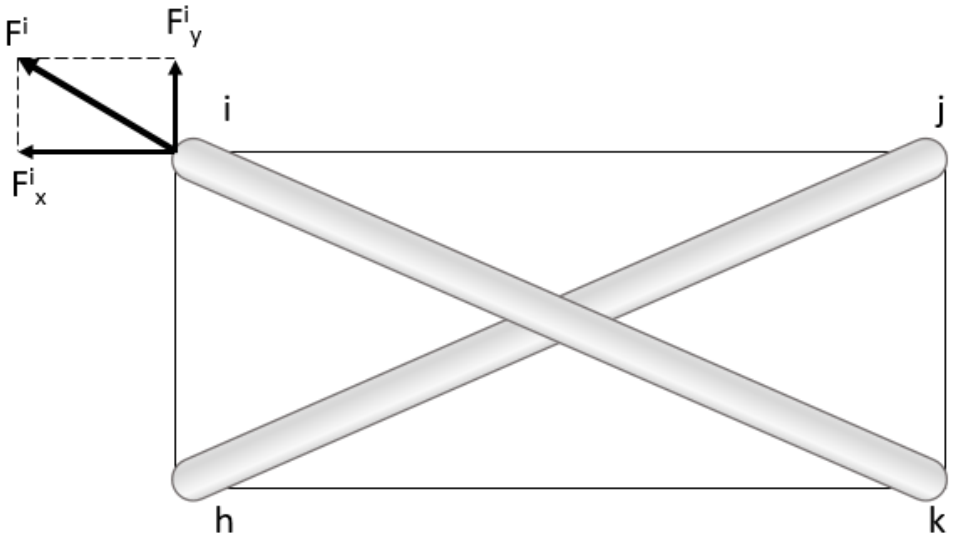

Figure 32 Simplified 2-D tensegrity model for the equilibrium equation example

The equilibrium equations for point i in the 2D system shown above are given in Eq.(14)

$$\begin{aligned} F_x^{(\overline{ih})} + F_x^{(\overline{ij})} + F_x^{(\overline{ik})} - F_x^{(i)} &= \frac{\left(x^{(h)} - \mathrm{x}^{(i)}\right)F^{(\overline{ih})}}{l^{(ih)}} + \frac{\left(x^{(j)} - \mathrm{x}^{(i)}\right)F^{(\overline{ij})}}{l^{(ij)}} + \frac{\left(x^{(k)} - \mathrm{x}^{(i)}\right)F^{(\overline{ik})}}{l^{(ik)}} - F_x^{(i)} = 0 \\ F_y^{(\overline{ih})} + F_y^{(\overline{ij})} + F_y^{(\overline{ik})} - F_y^{(i)} &= \frac{\left(y^{(h)} - \mathrm{y}^{(i)}\right)F^{(\overline{ih})}}{l^{(\overline{ih})}} + \frac{\left(y^{(j)} - \mathrm{y}^{(i)}\right)F^{(\overline{ij})}}{l^{(\overline{ij})}} + \frac{\left(y^{(k)} - \mathrm{y}^{(i)}\right)F^{(\overline{ik})}}{l^{(\overline{ik})}} - F_y^{(i)} = 0 \end{aligned} \tag{14}$$

where $F^{(\overline{ab})}$ is the tensile or compressive force applied on by a member $\overline{ab}$, $l^{(\overline{ab})}$ is the length of a member $\overline{ab}$, $F^i$is an external force applied at node i with x and y components of $F_x^{(i)}$ and $F_y^{(i)}$ respectively, and $x^{(n)}$ and $y^{(n)}$ are the Cartesian location of the nodes n of each member. It is convenient to reduce the quantity $F^{(\overline{ab})}/l^{(\overline{ab})}$ into a single term $q^{(\overline{ab})}$, often referred to as the force density coefficient in tensegrity literature [51,128–130]. To further simplify this case, we will not consider any external load onto the structure. Thus the equilibrium equations at point i can be simplified as seen in Eq. (15).

$$\begin{aligned}\left(x^{(h)}-\mathrm{x}^{(\mathrm{i})}\right)q^{(\bar{\imath}\bar{h})}+\left(x^{(j)}-\mathrm{x}^{(i)}\right)q^{(\bar{\imath}\bar{j})}+\left(x^{(k)}-\mathrm{x}^{(i)}\right)q^{(\bar{\imath}\bar{k})}&=0\\ \left(y^{(h)}-y^{(\mathrm{i})}\right)q^{(\bar{\imath}\bar{h})}+\left(y^{(j)}-\mathrm{y}^{(i)}\right)q^{(\bar{\imath}\bar{j})}+\left(y^{(k)}-\mathrm{y}^{(i)}\right)q^{(\bar{\imath}\bar{k})}&=0\end{aligned} \tag{15}$$

By defining a connectivity matrix, $[C]$, the equilibrium equations can be written in matrix notation for all of the nodes in a structure. The connectivity matrix has one row per member and one column per node with entries of +1 for the initial node, -1 for the terminal node, and 0 if the node is not in the member. In this example the connectivity matrix would be the 6x4 matrix shown in Eq. (16)

$$\begin{array}{c} \\ \bar{h}\bar{\imath} \\ \bar{\imath}\bar{j} \\ j\bar{k} \\ \overline{kh} \\ \bar{\imath}\bar{k} \\ j\bar{h} \end{array}\begin{array}{c} \begin{array}{cccc} h & i & j & k \end{array} \\ \begin{bmatrix} 1 & -1 & 0 & 0 \\ 0 & 1 & -1 & 0 \\ 0 & 0 & 1 & -1 \\ -1 & 0 & 0 & 1 \\ 0 & 1 & 0 & -1 \\ -1 & 0 & 1 & 0 \end{bmatrix} \end{array} = [C] \tag{16}$$

Thus Eq. (14) can be re-written as seen in Eq. (17).

$$A\{t\} = \begin{bmatrix} C^T diag(C\{x\}) \\ C^T diag(C\{y\}) \end{bmatrix}\{t\} = \mathbf{0} \tag{17}$$

where A is the equilibrium equation and t is a vector of normalized forces, known as tension coefficients. It is also helpful to point out the terms Cx and Cy are the projected lengths of each member in the x and y direction respectively. Similarly, Eq. (14) can be factorized as seen in Eq. (18).

$$\begin{aligned}\left(q^{(ih)}+q^{(ij)}+q^{(ik)}\right)x_i-q^{(ih)}x_h-q^{(ij)}x_j-q^{(ik)}x_k&=0\\ \left(q^{(ih)}+q^{(ij)}+q^{(ik)}\right)y_i-q^{(ih)}y_h-q^{(ij)}y_j-q^{(ik)}y_k&=0\end{aligned} \tag{18}$$

While Eq. (14) related the force density to the member length, Eq. (18) relates it to the location of each node. Eq. (18) can also be written in matrix notation

$$D[\{x\}\,\{y\}] = \ [C^T diag(\{t\})C][\{x\}\,\{y\}] = [\mathbf{0}\ \mathbf{0}\ \mathbf{0}] \tag{19}$$

where *D* is known as the Force Density Matrix. Equations (17) and (19) can be related to provide a single equation that relates tension coefficients, length coefficients, and nodal location. For a structure in three dimension the equation can be written as seen in Eq. (20)

$$\boldsymbol{I}_3 \otimes D\begin{Bmatrix} x \\ y \\ z \end{Bmatrix} - \begin{bmatrix} C^T diag(C\{x\}) \\ C^T diag(C\{y\}) \\ C^T diag(C\{z\}) \end{bmatrix} t = \mathbf{0} \tag{20}$$

where $\otimes$ is the kronecker tensor product and $\boldsymbol{I}_3$ is a 3x3 identity matrix. From this expression it can be seen that for tensegrity structures the member length, the configuration geometry, and the member force ratios are all inherently linked. Furthermore it will be shown that if one of these parameters is know the remaining two can be found.

Form-Finding Algorithm

Form-finding algorithms can utilize a variety of numerical methods to find a stable 3D configuration for the tensegrity structure. Tibert and Pellegrino's survey of various methodologies presents a good overview of the most prominent form-finding algorithms [128]. According to that work, there are two basic classifications of form-finding algorithms: statical and kinematic. The latter method uses some method to derive the structure's geometry from the equilibrium equations. The former method iteratively removes "slack" from the structure. Practically speaking, this is done by minimizing the total length of the tension members, or conversely, maximizing the length of the compression members (in turn creating a configuration where the cables are all in tension and the rods are in compression). The kinematic method only requires knowledge about how the structure is build (i.e. the connectivity matrix) and the desired normalized length for all of the tensile elements (i.e. length coefficients). For a given structure, various configuration can be solved for by providing new length coefficients. For this reason the kinematic form-finding method was adopted for this work. This benefit is specifically useful for active tensegrity structures, where the length of various tensile members can be altered and is not as readily available in statical form-finding algorithms. This will be discussed further in Chapter 6.

For regular systems, where much of the structure is known *a priori* via symmetry, this method can be performed analytically by optimizing a single variable. To demonstrate this consider the 6-bar, icosahedron tensegrity structure shown in Fig. 33.

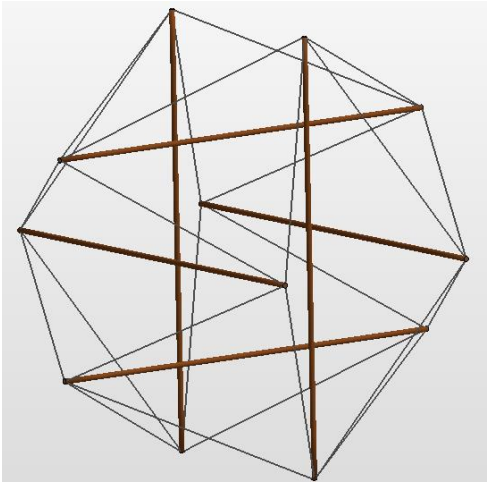

Figure 33 Icosahedron tensegrity structure comprised of 6 rods and 24 cables

The icosahedron is very common in tensegrity research [11,131,132] due to its near spherical shape and low number of structural elements. It is made up of 3 orthogonal sets of parallel bars with 4 cables connecting to each end of every rod, as seen in Fig. 33. By providing the constraint, that each rod must have the length, l_c, and each cable must have a length, l_T, the structure's geometry is constrained to a single degree of freedom. By placing a coordinate system at the centroid and aligning the axes such that they are parallel to one pair of rods, a single symmetric section can be analyzed, as shown in Fig. 34.

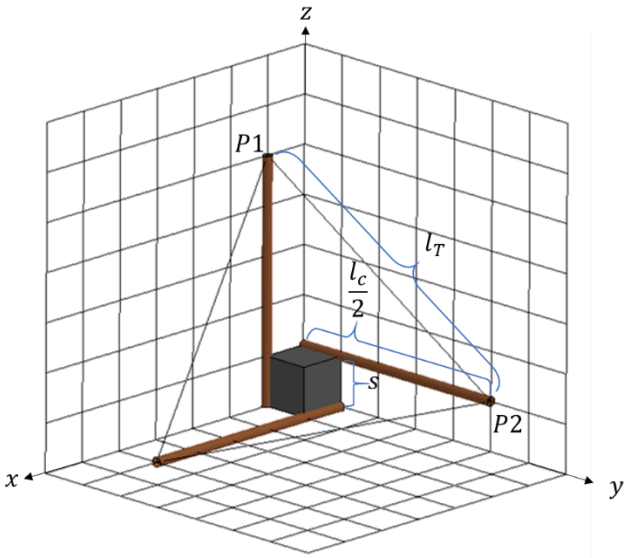

Figure 34 A single symmetric quadrant of the icosahedron structure

Here we can visualize the remaining unconstrained parameter as the normal spacing, s, between any two rods. Thus the length of the cable between *P1* and *P2* at point $(s, 0, {}^{l_c}/_2)$ and $(0, {}^{l_c}/_2, s)$ can be expressed as seen in Eq. (21)

$$l_T = \sqrt{(0-s)^2 + \left({}^{l_c}/_2 - 0\right)^2 + \left(s - {}^{l_c}/_2\right)^2} \tag{21}$$

The minimum length therefore can be solve for by simply setting the derivative of l_T with respect to s to zero as shown in Eq. (22). Thus the remaining unknown degree of freedom is solved for in Eq. (23)

$$\frac{dl_T}{ds} = \frac{2s - {}^{l_c}/_2}{\sqrt{s^2 + {}^{l_c^2}/_4 + \left(s - {}^{l_c}/_2\right)^2}} = 0 \tag{22}$$

$$s = \frac{1}{4} l_c \tag{23}$$

As expected, the equilibrium configuration of the icosahedron is when the space between any two parallel bars is half of the length of a bar, or $2s = l_T/2$. While this analytical solution is straightforward, it was enabled by some limiting assumptions, namely that all rods and cables have a uniform length.

A more general approach of this method using nonlinear programing was proposed by Pellegrino [133]. Given the connectivity matrix of the structure and the length coefficients of the members in the tension network, the nodal coordinates of each member are solved for according to Eq. (24).

$$\begin{aligned} &maximize \quad l_c = f(\mathrm{x},\mathrm{y},\mathrm{z}) \\ &subject\ to \begin{cases} \sqrt{\left(x_i^{(1)} - x_j^{(1)}\right)^2 + \left(y_i^{(1)} - y_j^{(1)}\right)^2 + \left(z_i^{(1)} - z_j^{(1)}\right)^2} - l_T^{(1)} = 0 \\ \sqrt{\left(x_i^{(2)} - x_j^{(2)}\right)^2 + \left(y_i^{(2)} - y_j^{(2)}\right)^2 + \left(z_i^{(2)} - z_j^{(2)}\right)^2} - l_T^{(2)} = 0 \\ \vdots \\ \sqrt{\left(x_i^{(n)} - x_j^{(n)}\right)^2 + \left(y_i^{(n)} - y_j^{(n)}\right)^2 + \left(z_i^{(n)} - z_j^{(n)}\right)^2} - l_T^{(n)} = 0 \end{cases} \end{aligned} \tag{24}$$

For the TANDEM Systems analysis Tool, this was solved using Matlab's constrained optimization routine, fmincon [134]. To increase the efficiency of the solver it is useful to restate the problem as shown in Eq. (25). Note that the formulation in Eq. (25) is the format presented by Pellegrino [133].

$$\begin{aligned} &minimize \quad -l_c^2 \\ &subject\ to \begin{cases} \left(x_i^{(1)} - x_j^{(1)}\right)^2 + \left(y_i^{(1)} - y_j^{(1)}\right)^2 + \left(z_i^{(1)} - z_j^{(1)}\right)^2 - \left(l_T^{(1)}\right)^2 = 0 \\ \left(x_i^{(2)} - x_j^{(2)}\right)^2 + \left(y_i^{(2)} - y_j^{(2)}\right)^2 + \left(z_i^{(2)} - z_j^{(2)}\right)^2 - \left(l_T^{(2)}\right)^2 = 0 \\ \vdots \\ \left(x_i^{(n)} - x_j^{(n)}\right)^2 + \left(y_i^{(n)} - y_j^{(n)}\right)^2 + \left(z_i^{(n)} - z_j^{(n)}\right)^2 - \left(l_T^{(n)}\right)^2 = 0 \end{cases} \end{aligned} \tag{25}$$

The implementation of the form-finding algorithm in the systems analysis tool was left parametric to enable drastic design variations. For example, in the basic design of the TANDEM vehicle there are 6 rotationally symmetric sections. In the systems analysis tool, this parameter can be altered with a single variable. Thus, multiple TANDEM designs can be experimented with, without needing to design an entirely new tensegrity structure. Figure 35 shows three examples of alternative TANDEM designs that may be used for other missions.

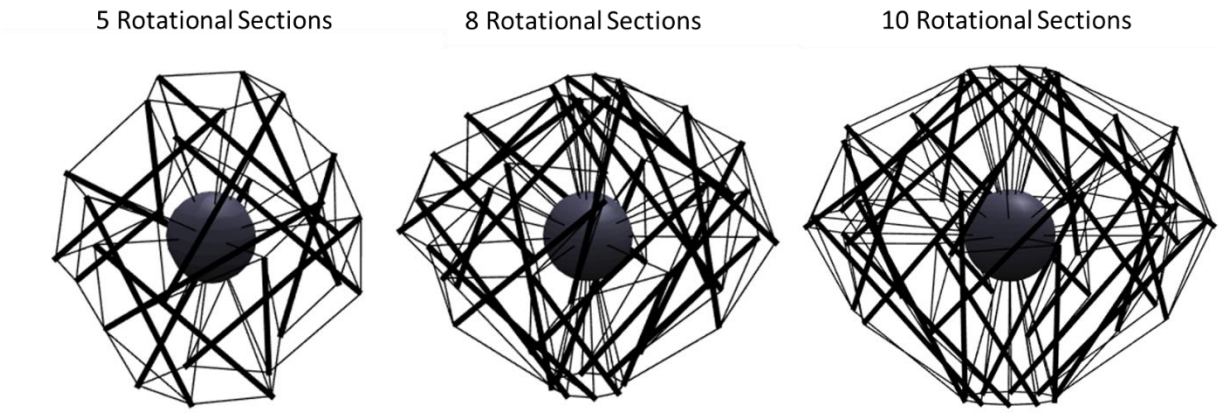

Figure 35 Parametric design control of the systems analysis tool

After the shape has been solved for, the newly configured structure was scaled to the appropriate size for the mission. After this, the tension coefficients can be found for the determined configuration by solving the system shown in Eq. (26) for *t*, where Eq. (26) is simply an expanded form of Eq. (20).

$$\begin{bmatrix} C^T diag(\{t\})C^T & \mathbf{0} & \mathbf{0} \\ \mathbf{0} & C^T diag(\{t\})C^T & \mathbf{0} \\ \mathbf{0} & \mathbf{0} & C^T diag(\{t\})C^T \end{bmatrix} \begin{Bmatrix} x \\ y \\ z \end{Bmatrix} - \begin{bmatrix} C^T diag(C\{x\}) \\ C^T diag(C\{y\}) \\ C^T diag(C\{z\}) \end{bmatrix} \{t\} = \mathbf{0} \qquad (26)$$

This methodology was used to find appropriate configurations for the vehicle at various point in the EDLL sequence. Table 8 reports the lengths and tension coefficient of each tension member for four vehicle configurations.

Table 8 Form-finding input parameters of standard configurations

	Length Coefficient of Each Tensile Member								
Configuration	Member 1	Member 2	Member 3	Member 4	Member 5	Member 6	Member 7	Member 8	Member 9
Stowed	2.40	3.50	1.50	1.50	3.50	2.40	1.00	3.00	1.00
Deployed	2.85	1.00	1.00	1.00	1.00	4.00	1.00	3.00	1.00
Descent	4.00	1.00	1.00	1.00	1.00	2.85	1.00	3.00	1.00
Landing	1.50	1.00	1.00	1.00	1.00	1.50	1.00	1.25	1.00
	Tension Coefficient of Each Tensile Member								
Configuration	Member 1	Member 2	Member 3	Member 4	Member 5	Member 6	Member 7	Member 8	Member 9
Stowed	0.430	0.438	0.587	1.000	0.216	0.318	0.562	0.259	0.535
Deployed	0.388	0.589	0.791	0.982	0.267	0.121	1.000	0.304	0.398
Descent	0.101	0.336	0.658	1.000	0.513	0.335	0.337	0.303	0.888
Landing	0.473	0.634	0.510	1.000	0.360	0.430	0.585	0.597	0.480

Modal Analysis for Launch Simulation

The VITaL and ADEPT-VITaL missions were to be launched on an Atlas V-551 [4,20]. An equivalent TANDEM mission, when the mass savings from the lander, the aeroshell, and the spacecraft propellant are considered, will be substantially lighter. This will enable a smaller (and cheaper) launch vehicle (LV) to be used and may open up the possibility of launching on a 400 series Atlas V. However for the sake of continuity with the other missions, the analysis of the TANDEM vehicle during launch will assume an Atlas V-551.

The launch environment for a spacecraft can be very harsh. Figure 36 shows the load factors for an Atlas V-551 launch. As can been seen, the peak loads can reach over 6 *g's* in magnitude. However, compared to atmospheric entry, the loads seen in launch are, for Venus, nearly an order of magnitude smaller. Thus the design of TANDEM will be driven by the entry and landing loads, not the launch. However, a critical criteria that must still be considered is the compatibility of TANDEM with the Atlas-V LV.

As a rule of thumb, the controls systems of a typical LV operates at a frequency of 7 Hz and below. Therefore, a spacecraft should have a natural frequency above 7 Hz in order to be compatible with the LV. The Atlas V, specifically, states in its User's Guide that spacecraft must maintain its first lateral mode at a minimum frequency of 8 Hz and a first axial mode at 15 Hz [135].

A low order FE model of the stowed vehicle was created. To highlight the assumptions made in the model, a comparison of a CAD rendering of the stowed entry vehicle and the low order FE model was provided in Fig. 37. From Fig. 37(a) it can be seen that when the vehicle is in its stowed configuration, the end of the heat shield ribs are latched to a truss structure. This truss serves as the connection between the entry vehicle and the cruise vehicle. In Fig. 37(b) it can be seen that the tensegrity structure, the rigid sphere-cone nose, and the rib structure of the heat shield are included in the model. The mass from the entry

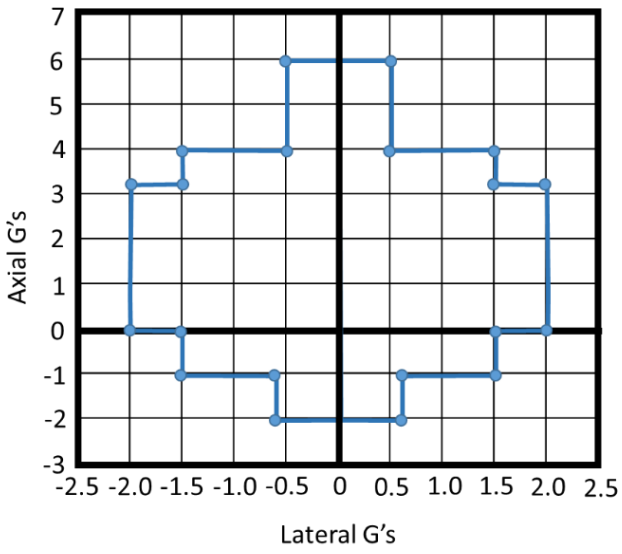

Figure 36 Spacecraft load factors for Atlas V-551 launch [135]

membrane is distributed to the heat shield ribs, but the actual carbon fabric and the mounting truss are not explicitly modeled. Additionally to increase efficiency, the nose was assumed to be rigid.

The dynamic response of the vehicle can be sensitive to changes in the design. This is especially true of the tensegrity structure. If a different stowed configuration is selected or if the length of the ribs are changes a new modal analysis may be required. The work presented below is representative of the Predicted Mass design discussed in detail in Chapter 7. As this design may be altered in future works, the goal of this model was to find the ballpark dynamic response of the vehicle. This will highlight any need for a major redesign.

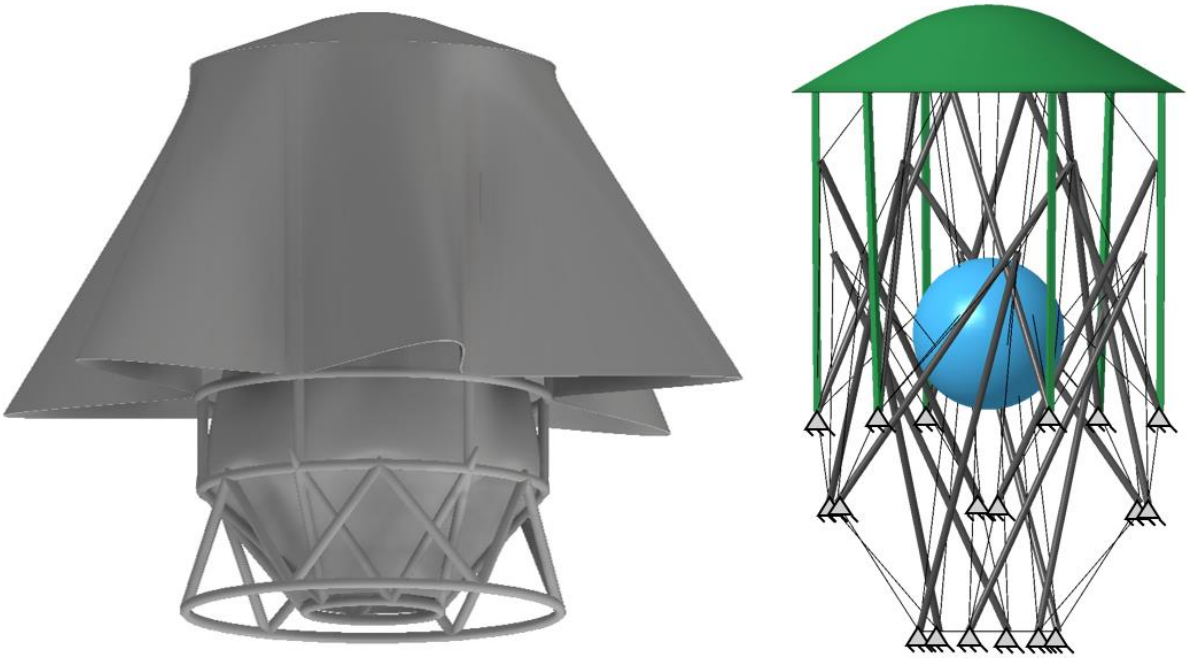

(a) (b)

Figure 37 The stowed TANDEM vehicle (a) computer aided design (CAD) rendering (b) finite element (FE) model with boundary conditions

The FE model used cable elements to represent the tension members. Cable elements are 1D elements similar to truss elements as they can hold no bending or torsional loads, but different as they are incapable of holding a compressive load, unless they are first pretensioned. The element formulation for a cable element is shown in Eq. (27), where A is the cross-sectional area of the element, E is the Young's modulus, and L is the length of the element. The assumptions made for cable elements represent the tension members well, but not perfectly. In reality, the tension members will be able to hold a small bending load. Thus it is expected that the results shown here are conservative, although the inclusion of the carbon fabric may introduce additional low frequency modes. This is not expected as the carbon fabric is reasonably stiff even without being pretensioned. However, if this should occur, additional constraints may be added to the

mounting truss to resist these modes. To ensure that the modal response of the vehicle is reproducible each time the structure is adjusted or disassembled, the pretension in the structure will be monitored by load cells in the structures feedback control system. Keep in mind that these results assume that the tensegrity structure is responsible for providing a large amount of the structural rigidity. If this proves to be problematic in future iterations, the tensegrity structure can be relaxed and an external wrap or case can be applied on the outside of the vehicle to increase its stiffness. An approach similar to this is planned to be used in the ADEPT sounding rocket test scheduled for September 2017 [39].

$$\begin{Bmatrix} F_x^{(1)} \\ F_y^{(1)} \\ M^{(1)} \\ F_x^{(2)} \\ F_y^{(2)} \\ M^{(2)} \end{Bmatrix} = \begin{cases} \dfrac{AE}{L}\begin{bmatrix} 1 & 0 & 0 & -1 & 0 & 0 \\ 0 & 0 & 0 & 0 & 0 & 0 \\ 0 & 0 & 0 & 0 & 0 & 0 \\ -1 & 0 & 0 & 1 & 0 & 0 \\ 0 & 0 & 0 & 0 & 0 & 0 \\ 0 & 0 & 0 & 0 & 0 & 0 \end{bmatrix}\begin{Bmatrix} u_x^{(1)} \\ u_y^{(1)} \\ \phi^{(1)} \\ u_x^{(2)} \\ u_y^{(2)} \\ \phi^{(2)} \end{Bmatrix} & for\ u_x > 0 \\ [\mathbf{0}]\begin{Bmatrix} u_x^{(1)} \\ u_y^{(1)} \\ \phi^{(1)} \\ u_x^{(2)} \\ u_y^{(2)} \\ \phi^{(2)} \end{Bmatrix} & for\ u_x \leq 0 \end{cases} \tag{27}$$

In Chapter 5 it is discussed that pretension was not a significant parameter in impact simulations. This, however, is not the case for the modal analysis. Based on numerical [131,136,137] and experimental work [138], it has been shown that the stiffness of a tensegrity structure increases with pretension. Many of these works discuss the existence of non-positive modes, known as "soft modes" [131,138,139], which can, in many cases, be stiffened by increasing the level of prestress. It was found for the TANDEM vehicle, that in order remove these soft modes, the structure must be pretensioned such that each tension member does not compress beneath its unloaded length, u_x. In the simulation this can be done by adding an intial load step to the vehicle to pretension the members and after the structure has reached equilibrium, run an additional load step for the modal analysis. Alternatively to decrease the run time and still produce the same results, the constitutive relationship in compression can be set to match that of a tensile load and the simulation can be run without pretension. This is numerically the same as defining the initial configuration in a pretension state without having to apply an additional load step. This will not affect the result of the modal analysis because the axial load is decoupled from all other DOFs.

The first five mode shapes are reported in Fig. 38. In Fig. 38(a) the fundamental frequency of the stowed vehicle is shown. Not surprisingly, this mode oscillates the unconstrained nodes of the tensegrity

structure. This is the first lateral mode and as required by ULA, it is above 8 Hz. Three additional lateral modes are encountered in the 19-28 Hz frequency range, as can be seen in Fig. 38(b-d). Then, at a frequency of 30.7 Hz, the first axial mode was encountered. This mode is just over twice the minimum allowable frequency for this mode.

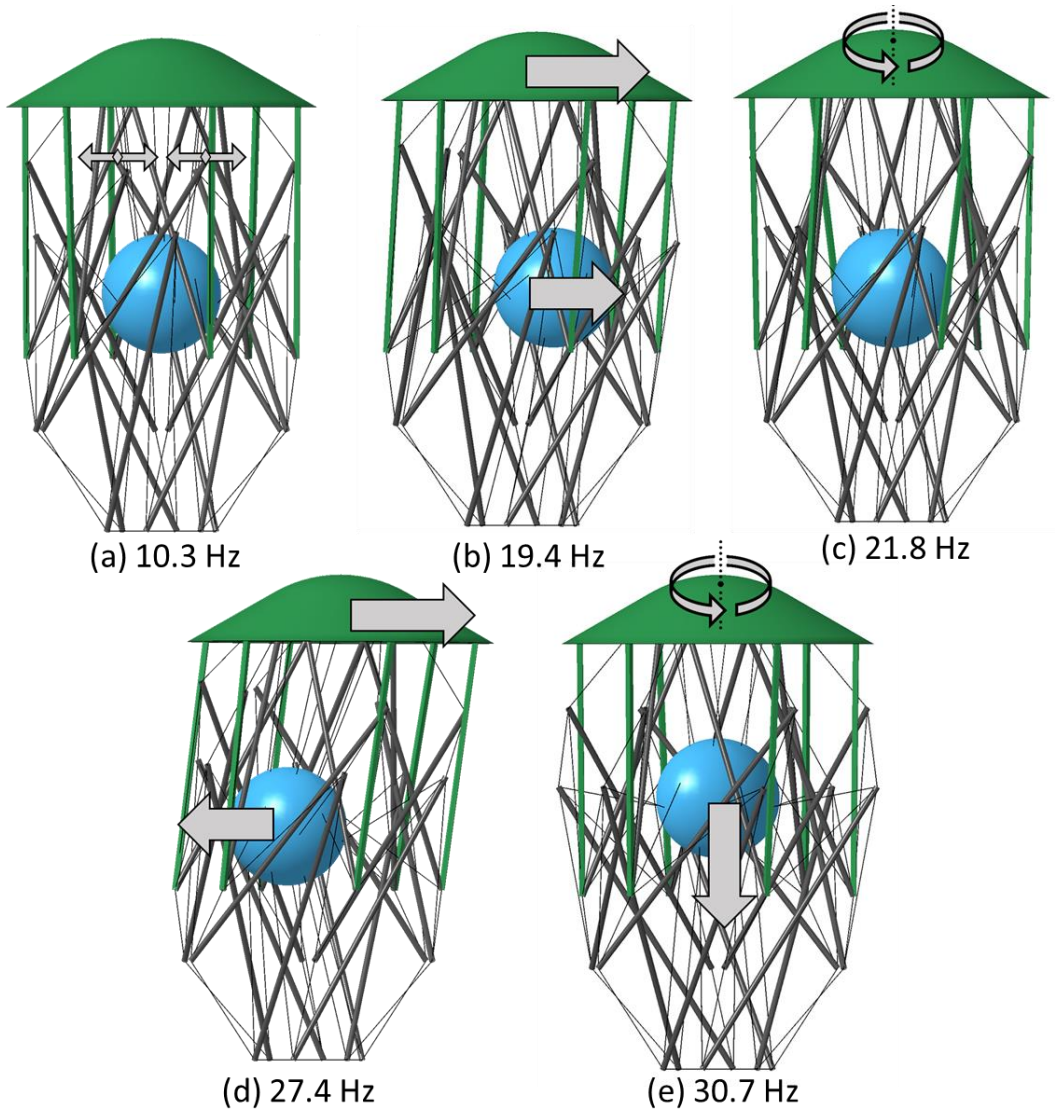

Figure 38 First five mode shapes (a) shows the first lateral mode (e) shows the first axial mode

From this preliminary investigation, it has been shown that the Predicted Mass design of TANDEM is compatible with the Atlas V-551. The first lateral and first axial modes are both above the required limits for a spacecraft. Future work will further investigate the launch environment. The low-frequency quasi-sinusoidal vibration levels of a LV is reported by ULA as being design driver for lightweight structures. A coupled loads analysis will be used to further investigate these loads to assess the margin of safety of TANDEM. As mentioned previously, if destructive resonance is experienced in this analysis, the tensegrity

structure can be relaxed and over-wrap can be applied to the vehicle during launch to provide structural rigidity instead. This alternative packaging approach can be easily used to tune the eigenvalues of the structure such that it can safely endure the launch environment.

Impact Simulation and Locomotion

The results of this algorithm are then exported for use in developing the FE model for impact and locomotion analysis. These analysis will be discussed in in more detail in the subsequent two chapters. The method can also be used to develop the required control strategies for configuration transitions throughout the EDLL sequence as discussed in Chapter 6.

Based on the process described above, the EDL sequence of a sample trajectory can be analyzed in seconds. This enables a variety of different trajectories to be analyzed to fully explore the design space of the EDL sequence of the TANDEM vehicle. Additionally, the tool is designed such that any one of the modules can be removed and replaced with a higher fidelity module if desired. The 3 DOF equations of motion could be replaced with a 6 DOF system, a more robust aerothermodynamic investigation could be performed, or a statistically varying atmospheric model could be implemented to run a Monte Carlo analysis on the trajectory to find the landing ellipse. The analysis tool's ability to rapidly provide reasonable estimations of each leg of EDL.

Chapter 5
Impact Characteristics and Crashworthiness of TANDEM

The first step in analyzing the Crashworthiness of TANDEM is to find the impacting speed, or the terminal velocity, of the vehicle. In the systems analysis tool, this is simply the velocity of the vehicle when the altitude = 0 *km*. From Eqs. (7) and (11), the terminal velocity can be approximated according to Eq. (28) by assuming that $\frac{dV}{dt} = 0$ and $\phi \cong 90°$. Both of these assumptions are reasonable, if the vehicle has been allowed to free fall several meters.

$$V_\infty = \sqrt{\frac{2mg}{C_D S \rho_\infty}} \tag{28}$$

All of the values in Eq. (28) are known, except C_D. In order to find a first order approximation of C_D to be used in systems analysis tool and to estimate the impact velocity of the Predicted Mass Model (discussed in Chapter 7) the low-altitude portion of the atmospheric descent was investigated using computational fluid dynamics (CFD). This work was performed by J. Feaster from Virginia Tech's CRASH Lab. The results of this study are summarized below for the purpose of discussion, but the full methodology and write up is reported in the Phase I NIAC by Bayandor et al. [2]

The vehicle is modeled descending through carbon dioxide with fluid properties at VSC: density (ρ) $64.8\ kg/m^3$, and a dynamic viscosity (μ) of $3.12 \times 10^{-5}\ kg/m - s$ [121,140]. In this analysis, the aerodynamic impact of the cables are assumed to be negligible and were not explicitly modeled. Neglecting the cables yields a more conservative estimate for terminal fall speed and significantly improves computational time.

The free falling TANDEM vehicle was estimated by parametrically varying both fall speed (V_∞) and rotational velocity around the vehicle's axis of rotational symmetry (ω) independently to understand how those parameters affect the drag to weight balance. This present analysis assumes that the drag to weight ratio was a function of purely the fall speed and the angular rotation rate of the vehicle. Parametrically studying the descent envelope allows the creation of analytical equations to describe, approximately, the relationship between drag force and flight velocity, as well as between Z-axis moment and rotational

velocity. For modeling simplicity, it was assumed that the vehicle would only rotate about its axis of symmetry. This assumption may prove to be simplistic upon further analysis but is not expected to dramatically affect the terminal velocity of the lander.

The initial estimate of terminal velocity for an 860 *kg* TANDEM vehicle near the surface of Venus was 26 *m/s*. To estimate the relationship between velocity, drag force and rotational moment, 3 non-rotating simulations were run, at velocities of 10, 20, and 26 *m/s* and an additional two axially rotating simulations were run at rotational velocities of -5 and -10 *rad/s* at a descent rate of 26 *m/s*. The drag force contribution by the compression members and payload are shown in Table 9 for velocities of 10, 20, and 26 *m/s*. The drag force contribution associated with the compression members is roughly seven times that of the payload across all velocities. The disparity in drag force between the compression members and payload is due, in part, to the compression members entraining flow between in the space between the members and payload. The entrainment reduces the effective velocity experienced by the payload, causing a decreased drag force contribution.

Table 9 Force and moment distribution from TANDEM free-fall analysis

$V\infty$ (m/s)	Payload Module		Compression Members	
	F_D (N)	M_Z (N-m)	F_D (N)	M_Z (N-m)
10	132.3	-0.1905	967.8	177.1
20	572.7	-0.5739	3826.6	689.9
26	955.4	-1.2302	6443.2	1164.5

The Z-moment for the payload and compression members were entirely caused by the angle of the compression members relative to the incoming flow. The relative angle and rotational symmetry of the compression members causes a significant moment force while the moment due to the payload is minimal because it is axisymmetric.

Time averaging the drag force and moment, and dividing by the predicted mass from Chapter 7 and the predicted moment of inertia ($405.7\ kg\ m^2$), respectively, yields the drag to weight ratio and rotational acceleration of the system. By using regression fitting, a system of equations was developed which related the angular acceleration, the drag to weight ratio and the descent velocity. By solving this system of equations where the drag to weight ratio was equal to 1 and the angular acceleration was zero, it was found that the terminal velocity of the lander should be around 25.2 *m/s* with a rotational velocity of -3.53 *rad/s*. This coincides with a ballistic coefficient of 2,456 kg/m^2 or a coefficient of drag of 0.45 based on the

projected area of the payload module. Figure 39 shows the iso-surfaces and streamline for the case closest to the steady state conditions.

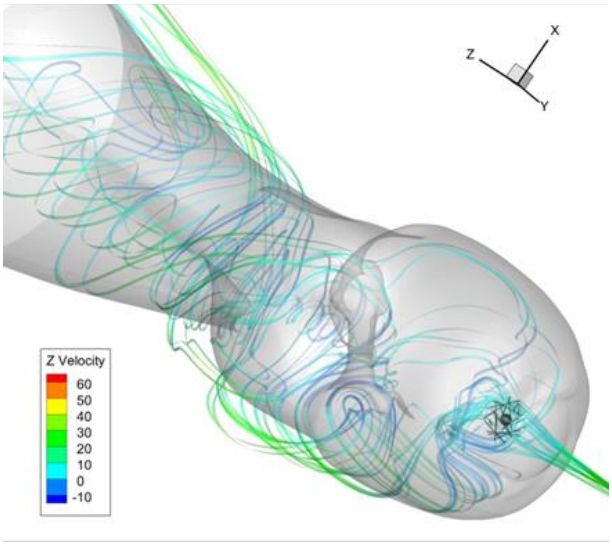

Figure 39 TANDEM vehicle descending at 26 *m/s* with a defined 5 *rad/s* rotation. Iso-surfaces are shown for a velocity of 8 *m/s*.

Development of a Modeling Methodology

A goal of this research was to show that TANDEM is able to provide sufficient impact resistance to enable safe landing in the Tessera region. To this end, a methodology was developed to accurately and efficiently predict the structural response of TANDEM during impact. In the development of this methodology a variety of explicit finite element models of various complexity were developed.

In order to maintain a low computational expense, it is preferable to model the tensegrity structure using only beam or rod elements. As the primary loads acting on the tensegrity structure are in line with each component, a 1D element appears to be a reasonable modeling assumption. In order to verify this modeling assumption a comparison of element formulations was conducted to show if vehicle response was preserved throughout the various modeling methods. Figure 40 shows a comparison of the TANDEM model with the compression members designed with 1D beam elements and 2D shell elements. Both models are identical except the type of element used to model the compression members. For this study all of the tension members were modeled with a 1D cable element. The cable element utilizes a bilinear, elastic constitutive relation; under a tensile loading the cable is perfectly elastic, whereas when the element is place in compression the cable provides no resistance.

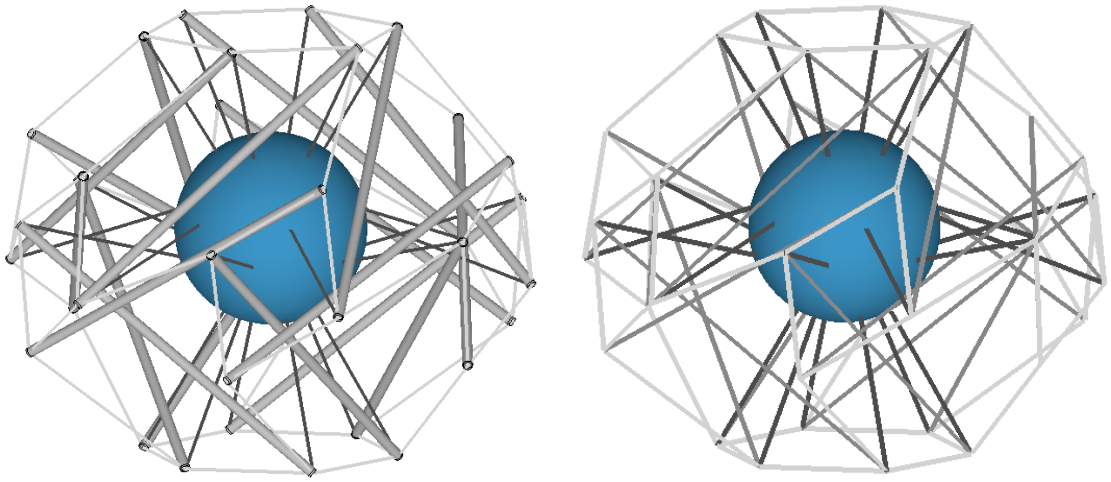

(a) (b)

Figure 40 Identical finite element models of TANDEM using two different modeling methodologies. (a) shell element formulation (b) beam element formulation

Four models were developed for each compression member element formulation type. Two models used rigid elements for the compression members with the other two using deformable elements. The other parameter explored was whether or not a mesh refinement should be used in modeling the tension members. For purely axial loading, with no dynamic effects, a single 1D element can fully capture the deformation of a rod or beam. However, the dynamics of the impact scenario induced a non-axial inertial load on the tension members. A mesh refinement of the cable elements allows them to deform in a transverse direction based on these inertial loads.

In designing a tensegrity structure for impact speeds ranging from 15 *m/s* to 30 *m/s*, it is important to have well-designed compressive members. If they are under-designed, the compressive members may buckle on impact. Fortunately, member buckling (even multi-member yielding) does not always result in mission failure, as the load will be redistributed throughout the tension network. If the compression members are significantly over designed, the resulting structure will be too heavy to be supported. An over designed structure can lead to tension member failure, excessive shock response, and can also result in the payload module impacting the surface. Additionally, it is also important not to put the tensegrity frame in its stiffest configuration. An overly-stiff configuration will result in excessively large *g*-loading. However, if the lander configuration is too compliant, the payload module may contact some of the compressive members or the surface on impact. Both of these contacts can lead to mission failure, as they can cause the pressure vessel to buckle, damaging the scientific equipment inside. All of these considerations must be taken into account during the impact analysis stage in order to produce a viable tensegrity lander.

Utilizing the vehicle terminal velocity from the flight mechanics simulation and landing configuration from the form-finding algorithm, the initial impact of the vehicle is simulated. The simulation is used to verify that the current design and configuration is adequate for the impact conditions (i.e., the tensegrity configuration provides sufficient stiffness but is not overly constrained, no buckling of the compressive members occurs, and payload *g*-loading does not exceed the maximum threshold).

Because the atmosphere is very dense at the surface, it may have a significant contribution on the impact scenario by adding a notable amount of drag and viscous damping to the system. Additionally, the deformation of the ground will add to the energy dissipation. However, neither effect is included due to the significant computational expense they required. Both of these mechanisms add to the energy dissipation on impact, removing them assures that the simulation is a conservative approximation of the landing sequence. A higher fidelity impact simulation can be made by modeling these two effects as a fluid-structure interaction (FSI). A study by Horton et al. investigated explicit fluid solvers available in commercial FEM software [141]. The coupled Lagrangian-Eulerian (CLE) method was shown to be a robust monolithic system that can be implemented into this modeling methodology to better capture the energy dissipated by dense atmosphere or by landing on soft soil.

For the development of a modeling methodology, a sample impact scenario was devised. In this scenario a TANDEM vehicle was designed to impact the surface at 10 *m/s* carrying a 180 *kg* payload module. This vehicle used the landing configuration reported above in Table 8 with a compression member length of 2 *m* and the shortest tension member being 67 *cm*. The compression members have an average diameter of 5 *cm* and wall thickness of 6 *mm*. Figures 41 shows a typical impact sequence for this model.

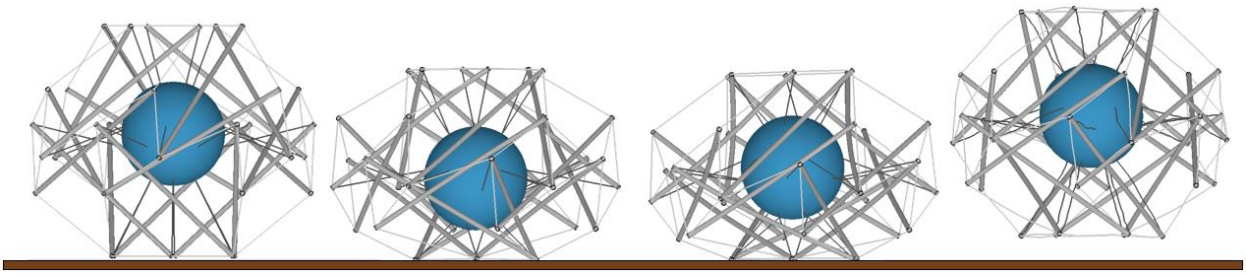

Figure 41 Time-lapse of 0° orientation impact simulation of a 180 *kg* payload model at 10 *m/s*

Pretensioning of the Tensegrity before Impact

From the Equilibrium equations presented in Chapter 2, it is known that the geometry of tensegrity structures dictates the tension coefficient of each member. The true load in each member is found by multiplying the tension coefficient by a scale factor. For structures with a low pretensioning load, gravitational loads (and other external forces) will dominate the load experienced by each member.

Alternatively, when the structure has higher levels of pretensioning, the effects of gravity become negligible and the tension coefficients will be better predicated by Eq. (26). It is noteworthy that while pretensioning the structure increases the stiffness of the structure [131] making it more resistant to quasi-static and vibrational loads, it does not significantly affect the impact characteristics of a structure for impact simulations.

The tension coefficient of each member is a function of the vehicle's geometry. As a result they are, in a way, preprogrammed into the structure. Even in an impact scenario, the relative loads of each member are largely maintained. This is demonstrated in Table 10. The impact simulation in Table 10 does not include any member pretensioning, yet the basic loading on each cable throughout the impact correspond to the analytical tension coefficients for a static structure. It is expected that there would be some deviation between the static solution and the impact simulation due to the dynamics of the members and the deformation of the structure.

Table 10 Comparison of dynamic load paths and static tension coefficients

Member	Coefficient Analytical	Coefficients at 10 *ms*	Coefficients at 25 *ms*	Coefficients at 40 *ms*
1	0.536	0.643	0.694	0.639
2	0.657	0.677	0.668	0.624
3	0.447	0.315	0.307	0.329
4	1.000	1.000	1.000	1.000
5	0.357	0.308	0.301	0.363
6	0.516	0.587	0.595	0.626
7	0.552	0.615	0.641	0.627
8	0.728	0.668	0.654	0.683
9	0.438	0.442	0.408	0.428

Figure 42 contrast two simulations, one with pretensioning and on without. As can be seen the two simulations are virtually the same both for the payload acceleration in Fig 42 (a) as well as the force in a sample member in Fig 42 (b). In Figure 42(b) the initial tension scale factor can be seen to increase by multiple orders of magnitude from the initial scale factor at time=0 to the peak loading approximately 70 milliseconds later. This shows how the typical pretensioning of a structure will be dwarfed by impact loads. Thus the initial tension scale factor is not a significant contributor to the general impact characteristics. To incorporate the scale factor into a FEM simulation the model must undergo a stress initialization. This can

be computationally expensive and does not significantly affect the impact characteristics. For these reason the tension scale factor was not included in the modeling methodology.

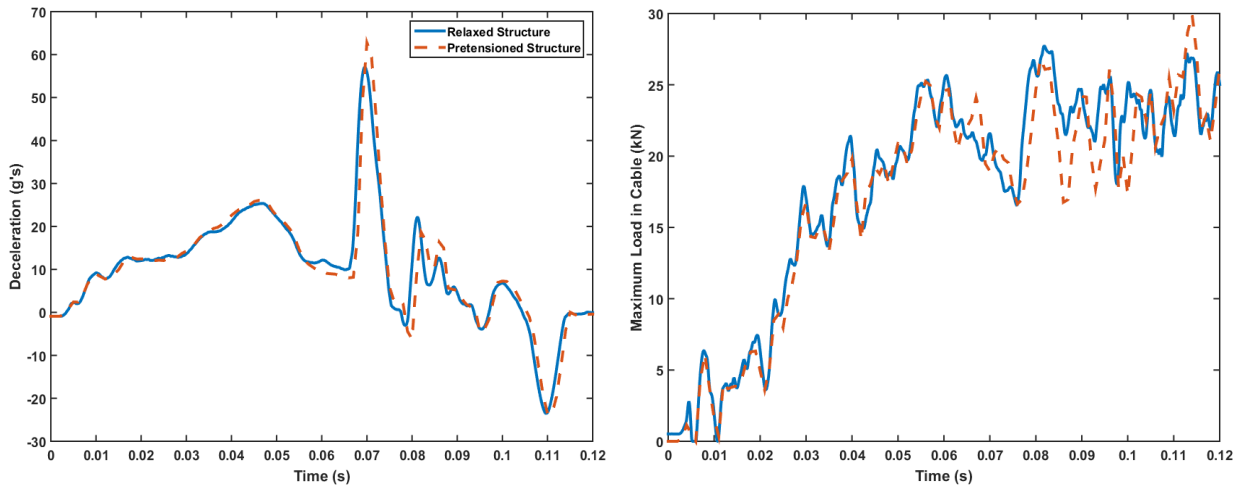

Figure 42 Comparison of response from pretensioned and relaxed structures (a) Payload deceleration (b) peak force in tension member

Modeling the Compression Members with Beam Element Formulation

This investigation found that the introduction of a mesh refinement for the cable elements induced numerical instabilities in the models that utilized beam elements for the compression members. Thus, of the four models developed that utilized beam elements for the compression members, only two models produced results. While the beam element models require minimal computational power, neither model performed exceptionally well. Both models were able to predict similar kinematic response to the higher fidelity simulations. However, they both over predicted the minimum clearance between the payload module and the impacting surface and over predicted the rebounding velocity. Figure 43 shows the *g*-load magnitude on the payload module for the models utilizing beam elements for the compression members. The model that incorporated the rigid compression members more similarly matched the kinematic response of the higher fidelity models, but it was found that the use of rigid 1D elements introduced a significant amount of numerical noise into the payload acceleration data. While the noise could be partially filtered out with a low bypass filter, as seen in Fig. 43, a more preferable solution was found using shell elements to model the compressive members.

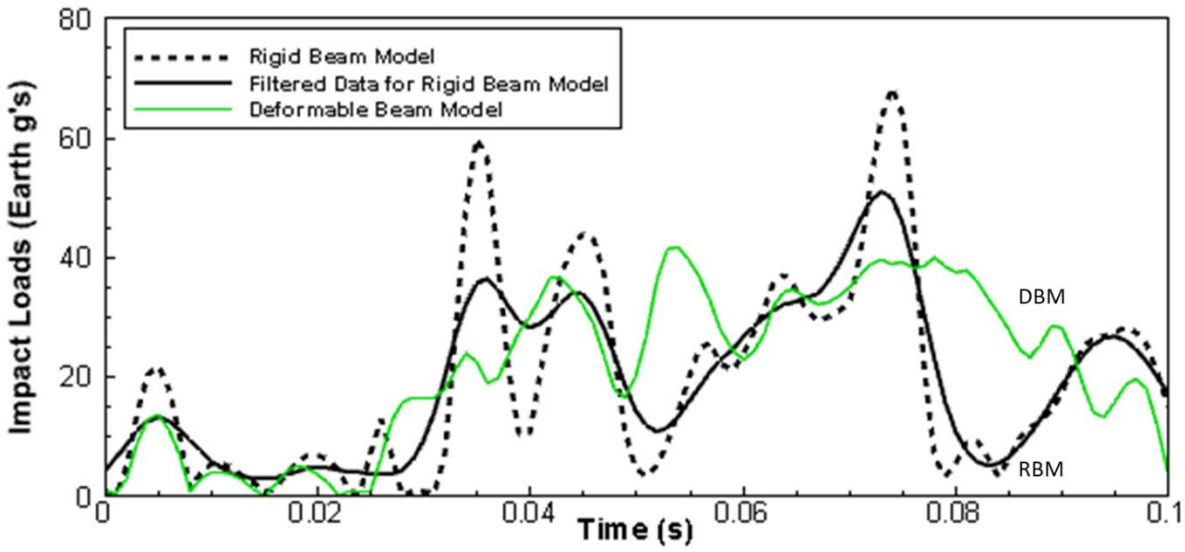

Figure 43 Magnitude of the *g*-load on the payload module for the models utilizing beam elements for the compression members. The rigid beam model was filters at 60 Hz

Modeling the Compression Members with Shell Element Formulation

All four of the models that utilized shell elements correlated very well with each other. All four models brought the payload to zero velocity at approximately the same time, roughly 70 *ms* after impact. Figure 44 shows the position of the payload module for the four models as a function of time. As expected, the minimum clearance between the payload module and impacting surface was notably smaller for the models that utilized rigid element for the compression members. This was because additional energy was dissipated through the deformation of the compression members. It can also be seen that the incorporation of the refined cable mesh resulted in only minor deviations in the kinematic response of the payload between both the rigid models and the deformable models.

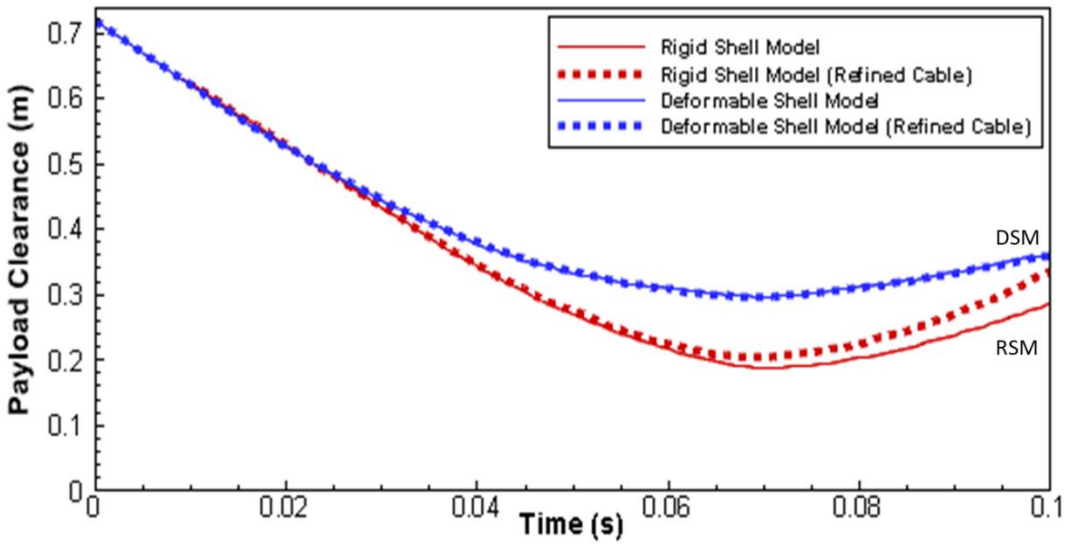

Figure 44 Comparison of the four developed impact model that utilize the shell element formulation for the modeling of the compression members

Because the system has a high number of degrees of freedom, it can be helpful to understand the dynamic response of the vehicle on impact by looking at the velocity of the payload module. For this impact analysis the lateral velocity of the payload was set to 0 *m/s*, thus only the vertical velocity is reported. Figures 45 reports the velocity of the payload module for the four shell element models, as well as the two beam element modules. For communication purposes, the kinematic response of the lander has been broken into three sections, as seen in Fig. 45: Initial contact from impact to 35 *ms*, constant deceleration starting after 35 *ms*, and payload rebound beginning as the payload velocity changes direction.

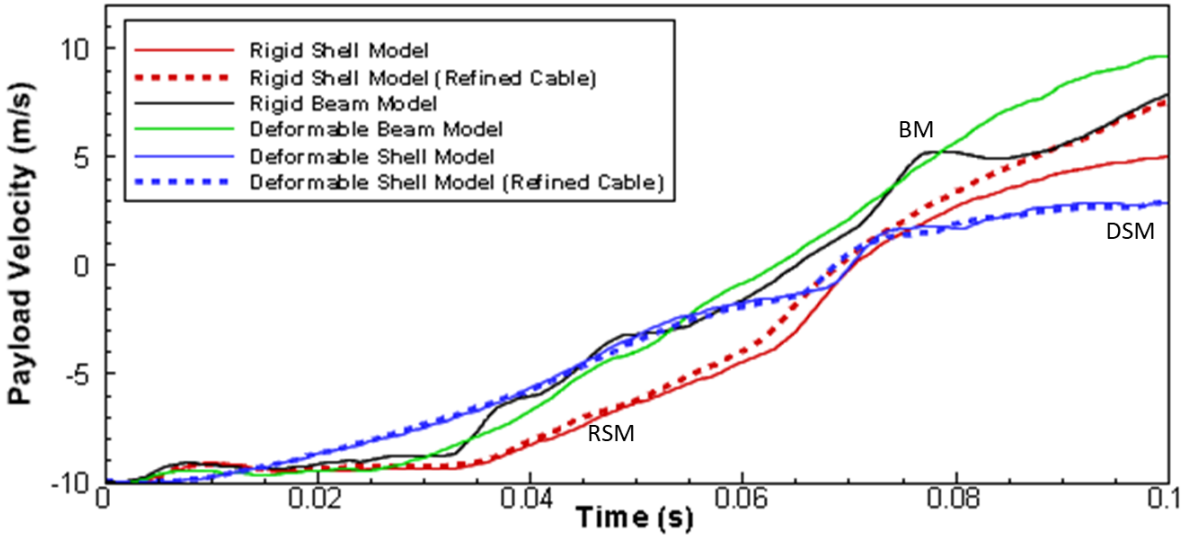

Figure 45 Comparison of all 6 impact model for the development of the modeling methodology

In the first section, initial contact, the expected response of a tensegrity lander during initial contact was captured by the two deformable shell models, which both predicted a smooth deceleration of the payload through the initial contact stage. As the vehicle contacted the surface, the lower compression members began to buckle slightly. Although this minor buckling does not result in any plastic deformation, it acts as a spring, providing a near constant force on the impacting surface.

Alternatively, the beam models and both rigid shell models reported a sudden decrease in velocity and then maintained a constant velocity thought that stage. This unexpected response was a result of the lower compression members recoiling after initial contact. The recoil occurred because the compression members in these model were all restricted from any non-axial deformation, thus preventing them from bending as the deformable shell elements had done. The delay in deceleration is a direct contributor to the larger stroke experienced by these models.

The next stage begins after the initial recoil of the lower members. At this point all of the models behave roughly the same, providing a relatively constant deceleration of the payload module. The constant deceleration is a result of the vehicle landing on a surface normal to its axis of rotational symmetry. Because of the configuration of the structure, the impact shockwave was evenly distributed around the structure, resulting in a near constant loading on the payload. However, as the shockwave was able to travel through rotationally symmetric load paths from the bottom of the lander to the top with very little attenuation, when the shockwave reached the top it was reflected back down into the payload model through the upper inner cables. The reflected shockwave resulted in a sudden velocity change of the payload module, which is evident in most of the model reported in Fig. 45. The constant deceleration stage lasted different lengths of time for the different models, but was terminated by this reflected shock wave. As each of the models arrested the payload, they rebounded with various velocities. The over prediction of the rebound velocity compared to the deformable shell elements, which is the highest fidelity model, can be attributed to numerous causes but an effect common to all of the models is that they were restricted from bending the compressive member. This restriction limited the amount of kinetic energy that could be dissipated in these model, resulting in a rebounding velocity larger than should be expected.

These simulations were developed to verify that a design is able to protect the payload module on impact. The clear connotation is that, for a given velocity and orientation, the tensegrity structure prevents the payload module from contacting the impact surface or any of the structure's own compression members. There is, however, an additional requirement. The tensegrity structure must protect the payload module in a manner that does not subject the payload module and its sensitive on-board equipment to excessive *g*-

loads. One of the many benefits of TANDEM is its implementation of a low ballistic coefficient deployable heat shield, which significantly reduces the entry loads experienced by the payload module compared to traditional entries. However, the benefit of the reduced entry loads is nullified if the landing sequence results in a significantly larger *g*-load. In order to develop an efficient vehicle, it must be designed such that these two primary loads are keep in a similar magnitude. Of course, there are some differences as the entry loads endure over time and the impact loads are impulse loads. Thus, the impact loads can be of a slightly larger magnitude.

The velocity and position plots are useful for understanding the kinematic variance of each developed model. Understanding these differences helps in selecting a model that efficiently balances realistic behavior and low computation expense. Figure 46 shows the acceleration magnitude of the four models that utilized shell elements to represent the structure's compression members. As seen in the velocity and position plots, Figs. 44 and 45 respectively, there is a close similarity between the refined cable models and single element cable models. Both types of models report the same trend, except that refined cable models of both reported notably lower peak loads than their single element counterpart. While this analysis does not reveal which of the four models best represents what would happen in a physical drop test, it does reveal that the use of a single cable element to model each tension member preserves the kinematics of the payload during impact and reports a more conservative peak *g*-load prediction. This modeling methodology was validated against a series of drop test experiments.

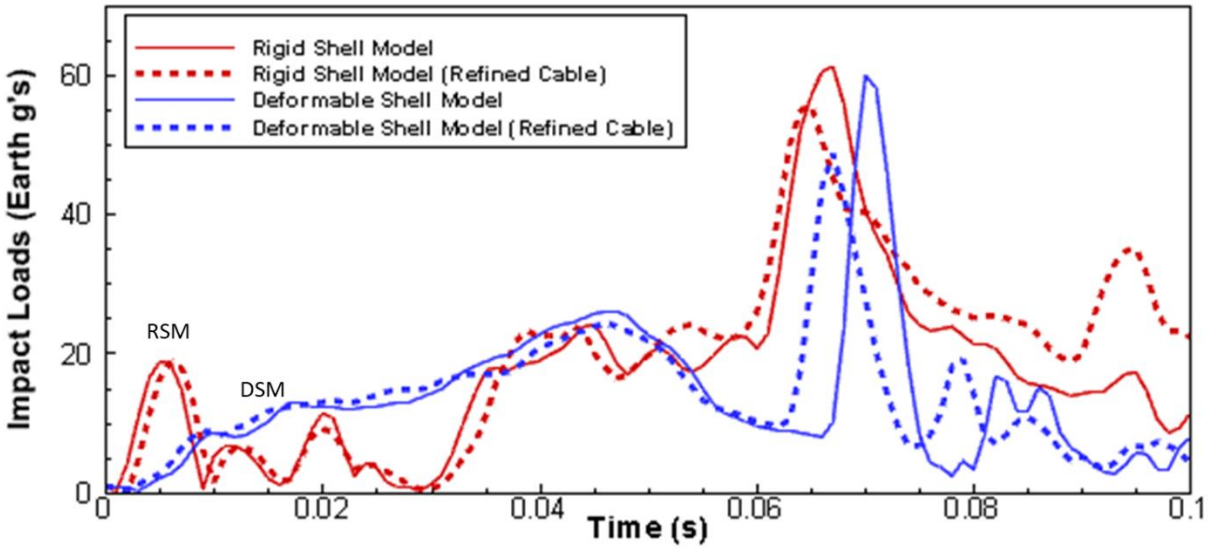

Figure 46 Magnitude of *g*-load on the payload module for the models that utilize shell element formulation

Contrasting the deformable and rigid models, the recoil on first contact experienced in the rigid body model can be seen. From Fig. 46 it is evident that in the rigid models there was not a single recoil but three distinct bounces of the lower compression members. We know from analyzing Figs. 44 and 45 that this bouncing results in a small overall clearance between the bottom of the payload and the impacting surface, but as we see in Fig. 46 it has only a minor effect on impact loads experienced by the payload. After the initial contact stage, all four models report very similar responses.

Notice also that if we are only interested in the max *g's* the payload module experiences, then there is very little difference between the values reported by the rigid compression member model and the deformable compression member model. To show that this result is repeatable, the rigid and deformable single cable element models were run at three additional orientations. Figure 47 contrasts the payload accelerations of the rigid and deformable models when the models have been rotated about the x-axis 30°, 60°, and 90°.

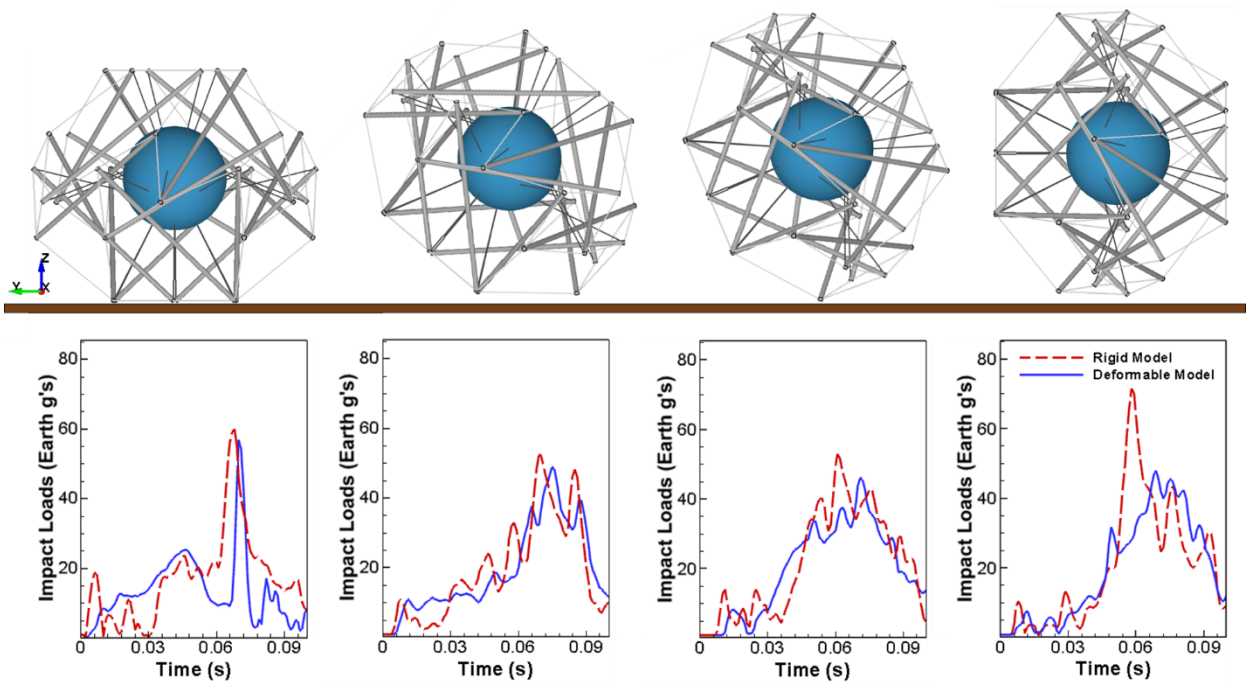

Figure 47 Parametric orientation study (a) baseline impact orientation, (b)baseline rotated 30° about the X axis (c) baseline rotated 60° about the X axis (d) baseline rotated 90° about the X axis

For these impact conditions, it has been shown that the peak deceleration load for the rigid and deformable models are within 12.5% of each other for three of the four orientations. This is a significant

find, as the deformable model takes approximately 4 times the computational power as the rigid model. Thus, for most simulations, the lower computational expense model can be used. There are exceptions where the rigid model does not match well with the deformable model, as seen in Fig. 47 (d). The difference in peak load is a result of the payload module contacting a compression member in the rigid model but not in the deformable model. As discussed previously and shown in Fig. 44, the rigid model over predicts the maximum displacement of the payload module. Additionally, in the deformable model when the compression members bend, they tend to bend outward, away from the payload module. In light of this, the rigid model is a conservative model for impact analysis, provided the compression members are well-designed. Thus, if the rigid body simulation predicts the payload module contacts one or more of the compression members or the impacting surface, a deformable model should be run to confirm that conclusion. In many cases, when the rigid body model predicts a contact, the deformable body shows a large clearance as seen in Fig. 48.

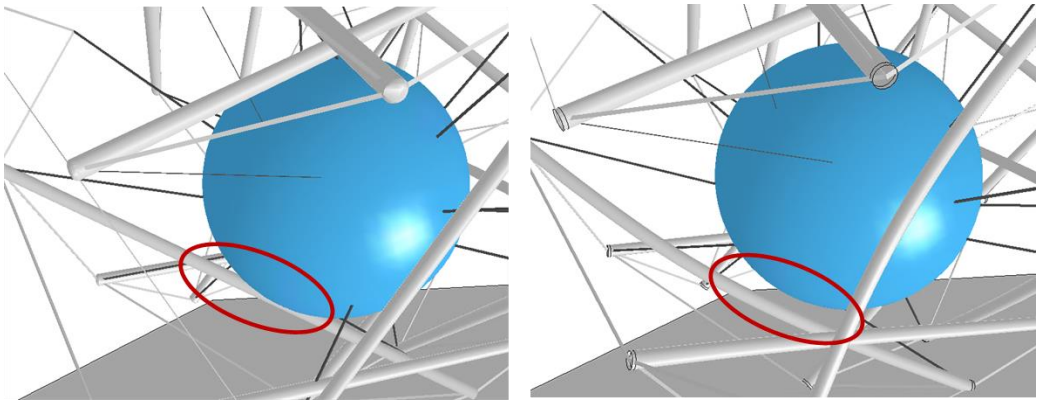

(a) (b)

Figure 48 Comparison of rigid (a) and deformable (b) compression members models shows that the rigid model predicts false collisions

From this analysis of various modeling methodologies, it was found that the use of beam elements to represent the compression members of a tensegrity lander, in the method described, is not feasible. The beam elements resulted in inaccurate kinematics and excessive numerical noise in acceleration data. An alternative method of using beam elements, proposed by Rimoli [142], may yield more favorable results, but this methodology was not attempted in this study. The next section of this chapter aims to validate the describe modeling methodology be contracting it with a physical drop test experiment.

Drop Test Validation

A TANDEM lander was built at roughly one-third the size of the 180 *kg* vehicle and designed to impact at one-quarter the impact velocity. The prototype is show in Fig. 49. Unlike the full scale vehicle,

the drop test model was not designed to be an active structure. Instead of implementing stepper motors to adjust the length of each tension member, the design was simplified to incorporate turnbuckles which could be manually adjust to the desired member length. As this prototype was not to be used for control strategy validation, this alteration was appropriate and drastically reduced cost as well as design and manufacturing time. The prototype was designed as described in Table 11.

Table 11 TANDEM design parameters for drop test prototype

		SI	English
Rod Length	(cm | in)	76.2	30
Rod Mean Diameter	(cm | in)	1.9	0.75
Rod Wall Thickness	(cm | in)	0.159	0.0625
Rod Mass	(kg | lbs)	0.52	1.15
Total Vehicle Mass	(kg | lbs)	21.14	46.5
Mass w/o Payload	(kg | lbs)	13.64	30

Figure 49 TANDEM prototype for drop test

The tension members were pretensioned sufficiently such that gravitational effects did not place a significant role in the internal force of each member. Recall from Chapter 2, that the equilibrium equations do not include temperature, gravity or external forces. This approximation is appropriate only when the pretensioning is significantly larger than the contributions from those forces. In practice, this is each to

determine as the structure will sag if sufficient pretensioning is not applied. When the structure is rested on its various faces, the operator will notice that the overall geometry of the structure adjusts as its weight is shifted. Whereas when the structure is properly tensioned, the structure will maintain a constant shape regardless its orientation.

For completeness the level of tensioning in each tension member was measured using Micro-Measurements 250BF-350 strain gages [143]. A gage was applied to the turnbuckle of each tension member in a rotational section. A correlation factor was measured to convert the strain of the turnbuckle into pounds of applied load. Based on strain gage measurements the tension scale factor was 400 *N* (90 *lbs*). Due to manufacturing constraints, the same tension member length coefficients could not be maintained in the drop test prototype as was used in the remainder of this dissertation. The following table provides the contrast the length and tension coefficients of the two geometries.

Table 12 Form-Finding Input Parameters of Standard Configurations

Length	Member	Member	Member	Member	Member	Member	Member	Member	Member
Coefficients	1	2	3	4	5	6	7	8	9
Prototype	1.25	1.00	1.00	1.00	1.00	1.25	1.00	1.00	1.00
Full Scale	1.50	1.00	1.00	1.00	1.00	1.50	1.00	1.25	1.00
Tension	Member	Member	Member	Member	Member	Member	Member	Member	Member
Coefficient	1	2	3	4	5	6	7	8	9
Prototype	0.536	0.657	0.447	1.000	0.357	0.516	0.552	0.728	0.438
Full Scale	0.473	0.634	0.510	1.000	0.360	0.530	0.585	0.597	0.480

The drop test model was capable of being run tethered or untethered depending on the scale of the drop. Tethered drops were able to record at a sampling rate of 5.12 *kHz* using a PCB Piezotronics shear accelerometer Model# 352C03 [144]. This was ideal for small drops. For larger drops, the vehicle could run untethered, where an onboard Raspberry Pi 3b [145] was used to record acceleration data at a frequency of 3.2 *kHz* with a maximum range of +/- 200 *g's* using an Analog Devices ADXL375 digital MEMS Accelerometer [146]. The prototype was dropped onto a flat cement surface at an impact velocity of approximately 2.45 *m/s*, corresponding to a 1 *ft* free fall drop. An example of the raw vertical acceleration data from one of the 6 drops is provided in Fig. 50.

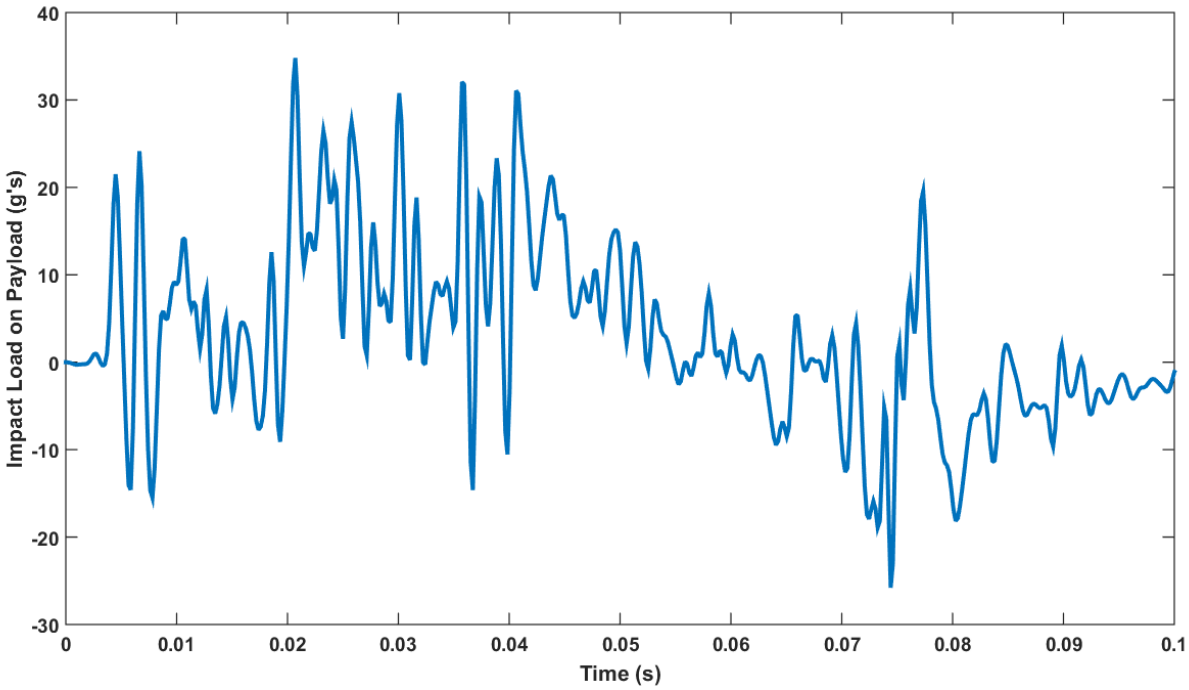

Figure 50 Payload acceleration data from drop test #2

The payload acceleration measured in the FEM simulation is a rigid body acceleration, which measures the kinematics of the payload module on impact. On the other hand, the acceleration data from the physical drop test measured the acceleration of a specific point, on a deformable body. As a result, it can be seen in Fig. 50 that there is more high frequency data in the drop test than has been seen previously in the FEM simulations. This high frequency data was expected due to the different methods of measuring acceleration data in the real world versus a virtual environment. The high frequency data obscures the overall trend of the payload on impact. However, it is hard to know which frequencies should be filtered out of the data to remove excess noise without compromising or over simplifying the complex dynamics of the payload on impact.

Much of this noise is thought to have been introduced from various component of the payload module which are not explicitly modeled in FEM simulations. For example, in the FEM simulation the inner cables were perfectly bonded to the payload module whereas in the physical model they are connect via chain links. This loose contact may induce vibrations to the payload module under highly dynamic loadings. Additionally, the accelerometer was mounted on to a steel plate which will also vibrate on impact. In order to identify the frequency range that contains the most important data, an equivalent FEM model was developed, using the same methodology as described above. The FEM model does not contain the same mechanisms that induce the high frequency data and as such it will help to highlight which frequency range is most crucial to analysis and what frequencies should be filtered out in order to accurately analyze

the impact. The vertical payload acceleration from the FEM simulation and the data from all six drop test were feed into a Fast Fourier Transformation (FFT). The two FFT plots are shown in Fig. 51.

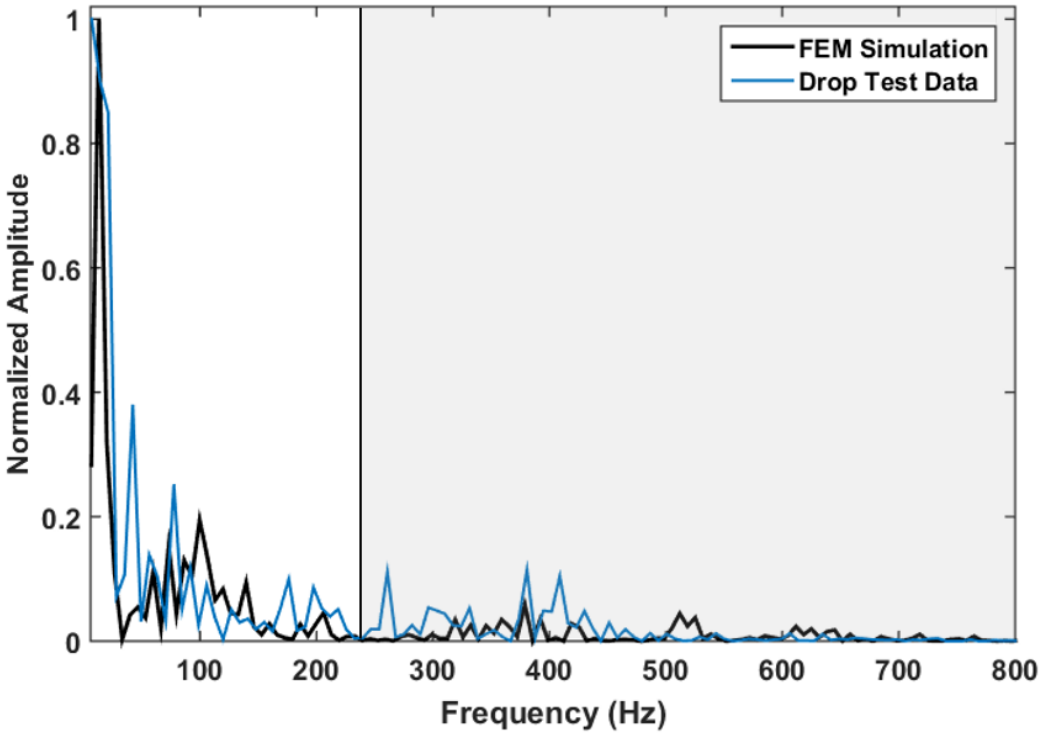

Figure 51 Fast Fourier Transformation (FFT) for FEM simulation and drop test experiment

From the FFT, it can be seen that both the drop test and the simulation have a similar initial peak frequency. This adds confidence to the modeling methodology by showing that both models behave similarly. It can also be seen that, for the simulation, most of the high amplitude data occurs before 240 Hz. In the physical drop test there are at least three significant peaks that occur after 240 Hz, two of which are not seen at all in the simulation. Thus, a cutoff frequency of 240 Hz was selected as it does not significantly alter the data from the simulation but still removes much of the high frequency data that is unique to the physical test.

The acceleration data from the six drop test and the corresponding simulation are presented in Fig. 52. This data was passed through a low-bypass filter with a cut off frequency of 240 Hz. Notice that a fair amount of variability from the physical drop test is seen, yet the overall trend remains constant. This was expected due to the slight variations in the drop conditions. Each drop landed approximately in the baseline impact orientation, where the impact surface normal is parallel with the vehicle's centerline or axis of rotational symmetry. However, the numerical precision that was obtained in the simulation is not achievable in practice. In order to maintain consistency between drops, an effort was made to insure that the coning

angle error (the maximum angle between the surface normal and the vehicle's centerline) was not greater than ±5° for any drop. However, Drop Test 3 and 6 may have been outside of this range. Although their basic loading and unloading trend is of a similar magnitude as the other cases, it lacks some of the key markers predicted by the simulation that are present in the other 4 drops.

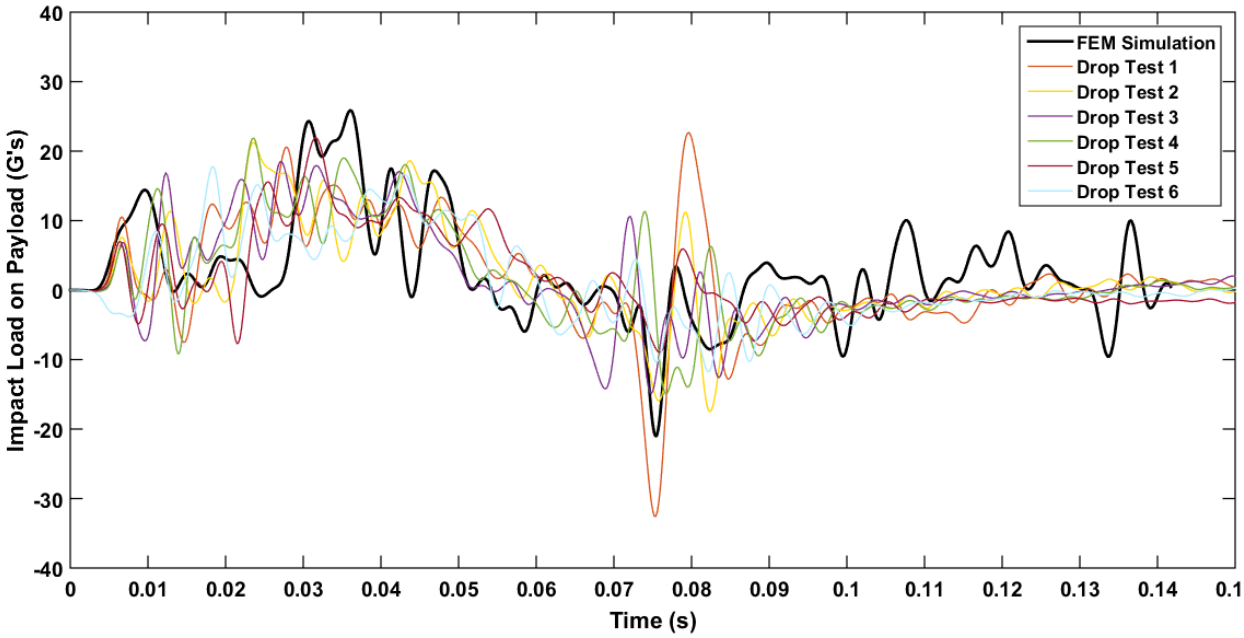

Figure 52 Payload acceleration data from all 6 drop tests and FEM simulation, all acceleration data was filtered at 240 Hz

Although there remains some variation in amplitude and frequency in the first 5 drops, the general trend shown the simulation data was also captured by all of them. In each of these drop test an initial acceleration spike can be seem, followed by a short lull where the acceleration drop back to nearly zero. The lull is followed by a sharp increase in acceleration where the maximum *g's* are encountered. Although each of the drops experiences the peak at a slightly different time, the peak *g's* seems remains consistent especially for the first five drops. Table 13 shows the peak acceleration seen in each drop as well as the percent difference compared to the simulation. As can be seen most of the drop test experience approximately 4-5 *g's* lower than the simulation predicts. This was satisfactory as the modeling methodology was designed to a rapid, low-fidelity, conservative impact model. Keep in mind therefore, that the acceleration values reported in the upcoming sections will also be conservative and may be as much as 15-20% over the actual impact scenario.

Following the peak *g*, the load decreases until the vehicle rebounds off of the surface. This rebounding occurs for all drop test at 75 ms and is marked by a sharp negative acceleration. It is interesting

that the rebounding *g's* can in some cases be approach the *g's* experience during max loading while in other cases it is much more benign. It is unclear what causes this variance and will be explored to see if it occurs in other cases. The largest discrepancy between the physical cases and the simulation is in the section after the rebound. In this time range, the simulation predicts an oscillating payload acceleration of ±10 g's while all of the physical cases converge down to a nearly constant value. This difference could be simply explained by the fact that there is no damping in the simulation, so the payload will continue to oscillate after the vehicle rebounds off the impact surface. In the physical drop test these vibrations were damped out by the structure and the air around it.

Table 13 Peak acceleration data from drop test compared to FEM simulation

	Peak Load (*g's*)	Max Difference	Percent Difference
Drop Test 1	20.6	5.3	20.5%
Drop Test 2	21.2	4.7	18.1%
Drop Test 3	18.5	7.4	28.6%
Drop Test 4	21.9	4.0	15.4%
Drop Test 5	21.9	4.0	15.4%
Drop Test 6	17.8	8.1	31.3%
FEM Simulation	25.9	N/A	N/A

Drop Test 3 and 6 experienced a noticeably lower peak *g* than the other drop tests. Both test reported a variance in peak acceleration around 30%. While there is a fair amount of variability in the drop test models, these cases also yielded some noticeable changes to the impact response especially in the initial impact to peak loading time range. Due to this, it is believed that these two drops may not have been performed under the assumed drop conditions. It is possible that these drops were released of axis, at a lower drop height, or a combination of the two. From the orientation study done above, results in Fig. 47, it is known that landing off axis may result in a decreased peak loading as well as a less pronounced lull between the initial contact and the maximum loading. Both of these characteristic are present in data from drop tests 3 and 6. Figure 53 compares these two off nominal cases from the physical drop test with a simulation of the drop tilted 5° of axis.

The purpose of the simulation in Fig. 53 is not to match the trend of the two different drops but to demonstrate how an off axis error can affect maximum deceleration of the payload. By varying the orientation of the off-axis simulation, it is believed that the general trend seen in drop tests 3 and 6 can be

captured, even the initial negative acceleration seen in drop test 3, which has been seen for some orientations. Given the variance in the test conditions, the conservative approach of the modeling strategy, and the low level of complexity in the FEM simulation; there is a great correlation between maximum *g*-load predicted in the virtual drop test and what actually occurs physically.

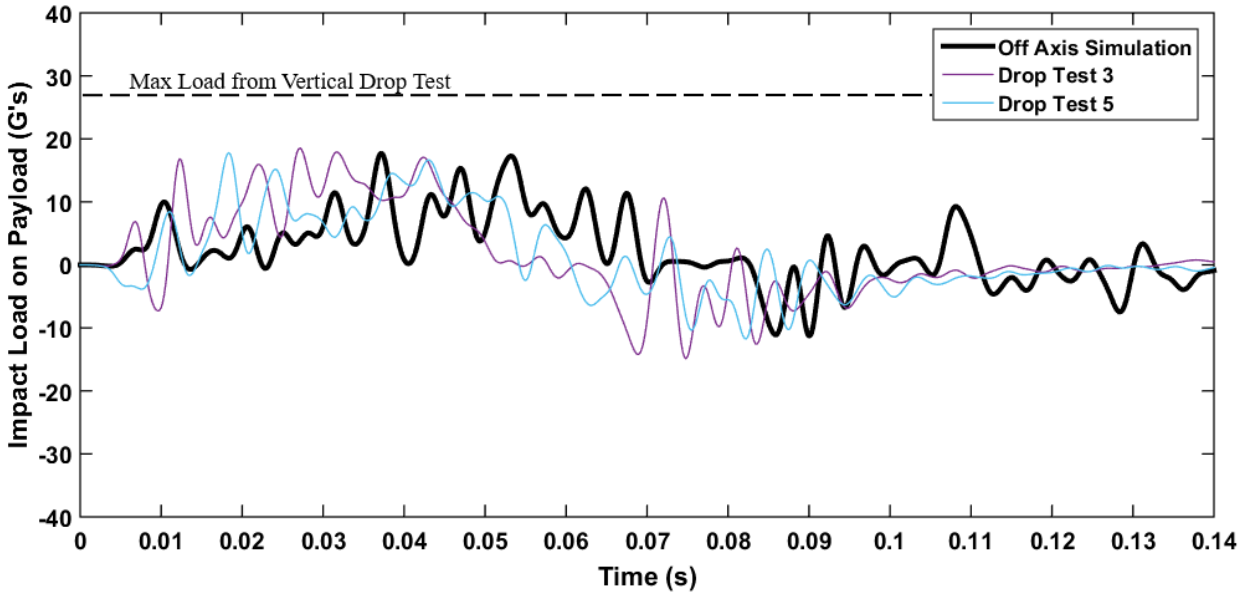

Figure 53 Comparison of 5° off axis drop test simulation with physical drop test outliers

While the over overall trend of the drop test experiment was captured by the simulation and the maximum deceleration seen by the payload module was predicted within 5 g's for most cases, the percent difference reported in Table 13 is deceptively high. To better show how well the simulation was able to capture the impact response of the vehicle the Power Spectral Density (PSD) of all 6 drops and the FEM simulation were compared, as shown in Fig. 54. Before being transformed into the frequency domain, the acceleration data was passed through a 150 Hz low by-pass filter so that only the data correlating to the impulse loading on the was considered.

Qualitatively the PSD of the simulation correlates well with the physical results, as it can be seen in Fig. 54 that the response from simulation is within the range of responses from the physical drop test. Quantitatively, it is generally accepted that the primary response of the structure has been captured if the PSD of the simulation is with 3 *dB* of the experiment. Based on the data shown in Fig. 54 the maximum difference between the physical experiment and the simulation for the peak response was less than 2 *dB*.

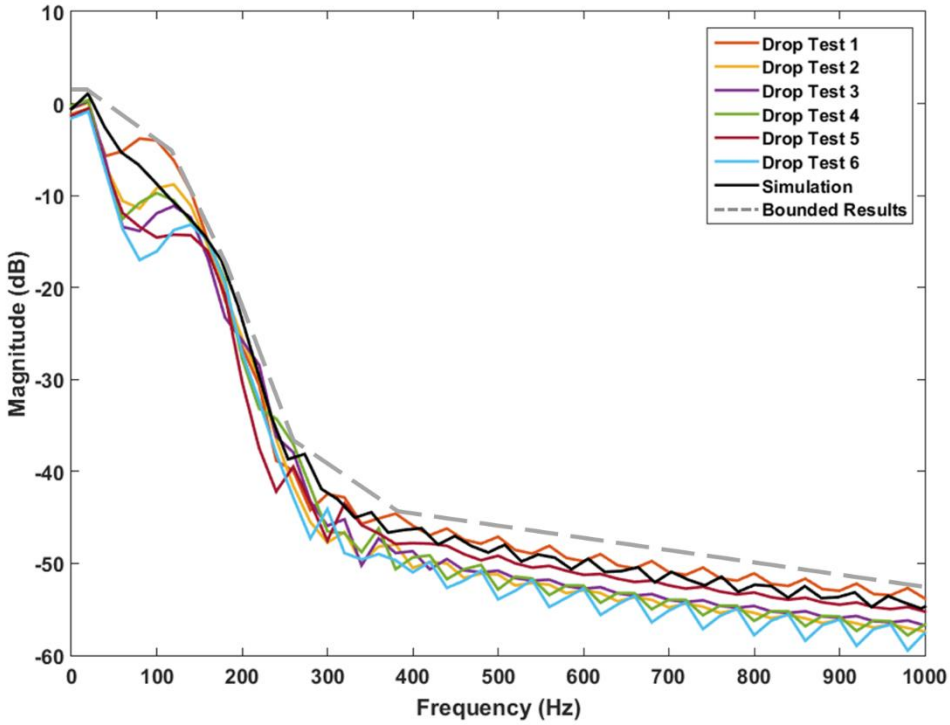

Figure 54 Power Spectral Density of the 6 drop test and the FEM simulation

Parametric Impact Study

Using the developed modeling methodology, as series of landers were developed to find any trends that may exist. Two 1 *m* diameter payload modules were used, one weighing 180 *kg* in total and the other weighing 260 *kg.* Various efficient, but not optimized, lander designs were developed based on three different impact velocities: 10, 20 and 30 *m/s*. Table 14 reports the dimension and masses of each vehicle design.

Table 14 Parametric TANDEM designs based on payload mass and impact velocity

		180 *kg* Payload Module			260 *kg* Payload Module		
		10 *m/s*	20 *m/s*	30 *m/s*	10 *m/s*	20 *m/s*	30 *m/s*
Rod Length	(*m*)	2.0	2.5	3.0	2.0	2.8	3.0
Rod Mean Diameter	(*cm*)	5.0	7.8	11.5	5.0	8.5	11.5
Rod Wall Thickness	(*cm*)	0.6	0.6	0.6	0.6	0.6	0.6
Rod Mass	(*kg*)	11.0	186.0	33.6	11.1	22.8	33.6
Total Vehicle Mass	(*kg*)	338.3	531.0	696.7	463.0	672.0	889.4
Mass w/o Payload	(*kg*)	158.3	351.0	516.7	203.0	412.0	629.4
Maximum *G*-load on Payload		59.9	96.9	224.4	35.3	87.0	192.9

The total lander masses from Table 14 were plotted and fitted to a trend line, as shown in Fig. 55. As can be seen, that there appears to be a linear relationship between impact velocity and total mass of the vehicle for a given payload module mass. This is complementary to the finding reported by Agogino et al. in their NIAC report that the mass of a tensegrity structure grows linearly with compression member length, unlike airbags which grow with the square of the radius [59]. This statement was made in the context of small, low mass tensegrity structures impacting at a constant velocity. The work presented in this study shows how the design will scale as the impact velocity increases. Furthermore, as the tensegrity vehicle increases in size, the compression members are more susceptible to buckling, due to a longer rod length. Thus, as a tensegrity structure is scaled up, the radius of the compression members must be increased, as well as its length. Our analysis takes all of this into account and still shows that the linear scaling relationship appears to hold up.

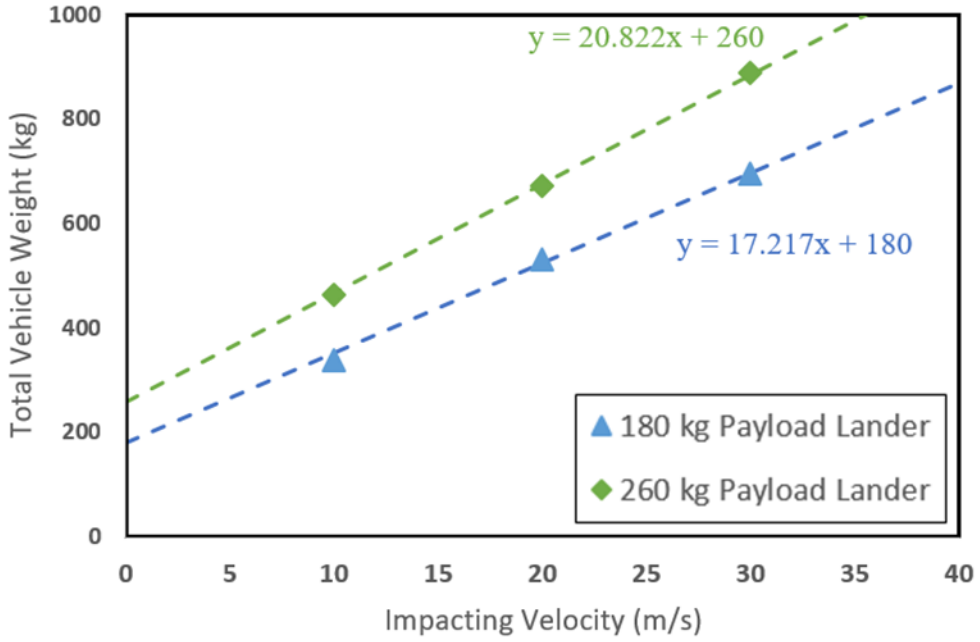

Figure 55 Scalability of TANDEM vehicle mass has a linearly relationship with impact velocity

Impact Globe

In order to demonstrate omnidirectional protection provided by TANDEM, a large parametric study was performed to impact the TANDEM model at various orientations. Each orientation was systematically selected to ensure an even sampling distribution across all possible orientations. Two models were selected for this analysis: the 180 *kg* payload model impacting at 10 *m/s* and the 260 *kg* payload module impacting at 20 *m/s*.

This parametric impact study resulted in a "globe" broken up into the latitudes and longitudes correlating to each impact simulation. Each point on this map represents the peak *g*-load experience by the payload for a given orientation. The south and north polar regions, in Fig. 56, correlate to the bottom and top face of the TANDEM vehicle respectively.

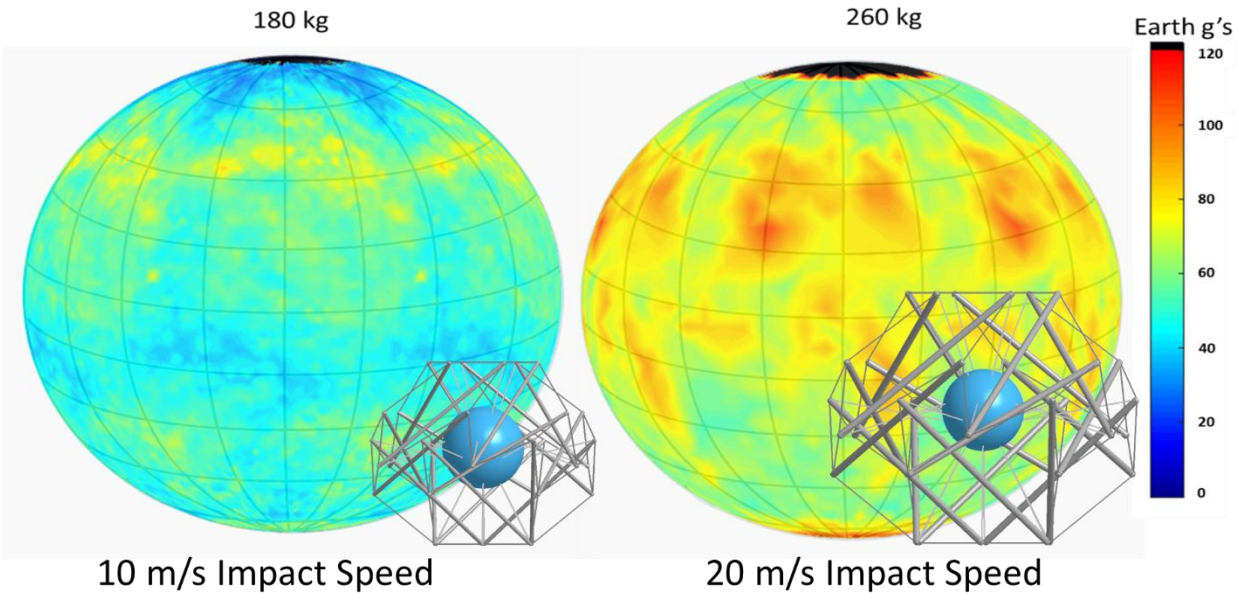

(a) (b)

Figure 56 Impact globes of two TANDEM models, (a) the 180 *kg* payload impacting at 10 *m/s* (b) 260 *kg* payload impacting at 20 *m/s*

The biggest takeaway from Fig. 56 is that an impact simulation has been run and analyzed for nearly every possible impact orientation. Furthermore, nearly all of the tested impact cases report a peak *g*-load on the payload module less than 120 *g's*. When the vehicle was completely inverted, however, this analysis predicted that the payload module would come into contact with the surface, shown in black on the northern poles of Fig. 56. While the impact occurred at a low velocity (approximately 2 *m/s*), it revealed a potential gap in the omnidirectional protection provided by TANDEM

Investigations of this weak point in the otherwise fully protective outer tension network revealed the cause of the weak point was in the selection of the impact configuration and not a problem inherent to the concept itself. By consulting the schematic of a rotational section of TANDEM, seen in Fig. 57, it was noticed that for some loading conditions, Bar 3 will attempt to apply a compressive load on Cable 3. Given that Cable 3 cannot hold a compressive load, the structure will produce a less stiff response. In the case of a high speed impact, this decreased stiffness will result in an increase in the payload module stroke, which can cause it to impact on the surface.

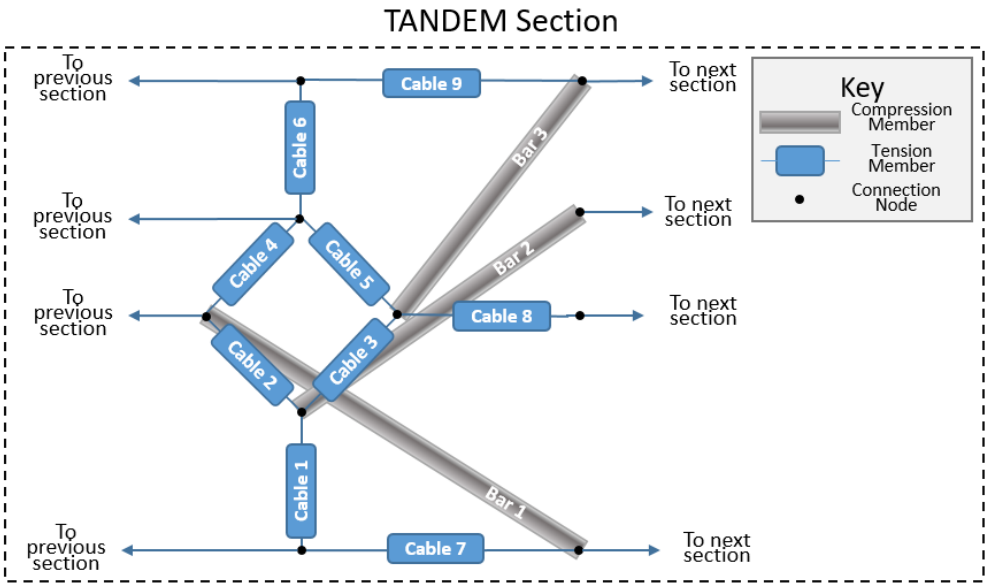

Figure 57 Schematic view of a single rotational section of TANDEM's tension network

While it is likely that this can be avoided by adjusting the landing configuration, it was decided that this weak point should be removed entirely by a small alteration in the connectivity matrix. Bar 3 was reoriented such that Bar 3's top node goes the "previous" rotational section, or the section to the right. This is shown as an alternative TANDEM section in Fig. 58.

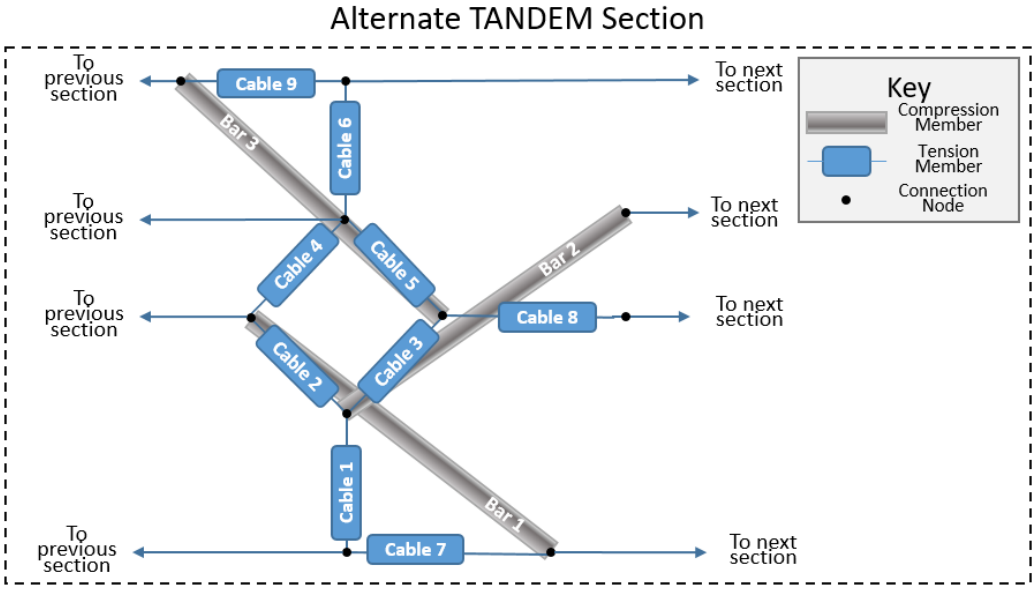

Figure 58 Schematic view of an alternative rotational section of TANDEM's tension network

The alternative TANDEM connectivity matrix was incorporated into the form-finding algorithm from Chapter 4 and a new FE model was developed based on the 260 kg design. The alternative design was

run through the parametric impact study to demonstrate that this correction will alleviate the landing risk seen previously the “northern pole” of the impact globe.

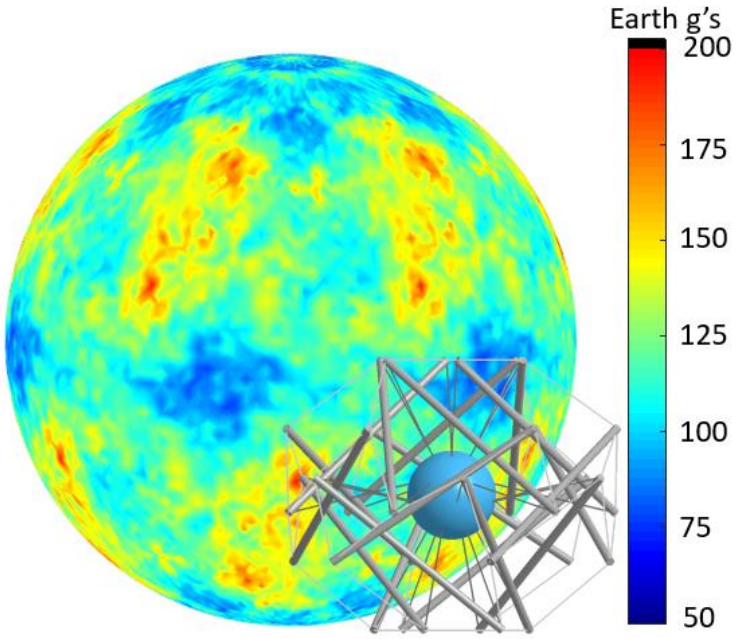

Figure 59 Impact globe of the 260 kg payload module TANDEM models for a 20 *m/s* impact

As seen in Fig. 59, the gap in the omnidirectional protection was removed by this small alteration. It can be seen that the average loading on the structure did increase, but the acceleration loads are still within a reasonable range with a maximum deceleration of under 200 *g’s*. In the alternate design a vertical symmetry was added to the tensegrity structure. This functionally reduces the number of simulations that must be run by half. The alternative design may be used in future work but to maintain continuity with the physical drop test, the remaining simulations in this dissertation will continue to use the original design shown in Fig. 57.

Obstacle Impact

As a primary goal of this investigation was to explore the feasibility of preforming landed science in the Tessera regions of Venus, it is important to explore very unfavorable landing conditions. Thus a boulder impact investigation was performed for two of the developed vehicle models: the 180 *kg* payload model impacting at 10 *m/s* and the 260 *kg* payload module impacting at 20 *m/s*. An investigation of radar reflectivity from Magellan and the Arecibo observatory suggest that Tessera regions can have surface roughness on the order of 10 to 50 *cm* [35] while the VITaL mission concept was designed to land on a

boulder as larger as 1.3 *m* tall [20]. So for this investigation, the two TANDEM vehicles were impacted on a 1 *m* tall rigid obstacle.

For the smaller vehicle an example impact was simulated where 3 of the 6 lower compression members were above the obstacle. Because the vehicle is held in a constant state of tension, even though only half of the lower compression members made contact with the impacting surface, the shape of the vehicle at its maximum stroke was nearly same its shape when it impacted a flat surface. However, because the landing was not level surface, the minimum clearance between the payload model and the impacting surface was reduced from 30 *cm* in the level impact case to 12 *cm* when landing on an obstacle, as shown on Fig. 60.

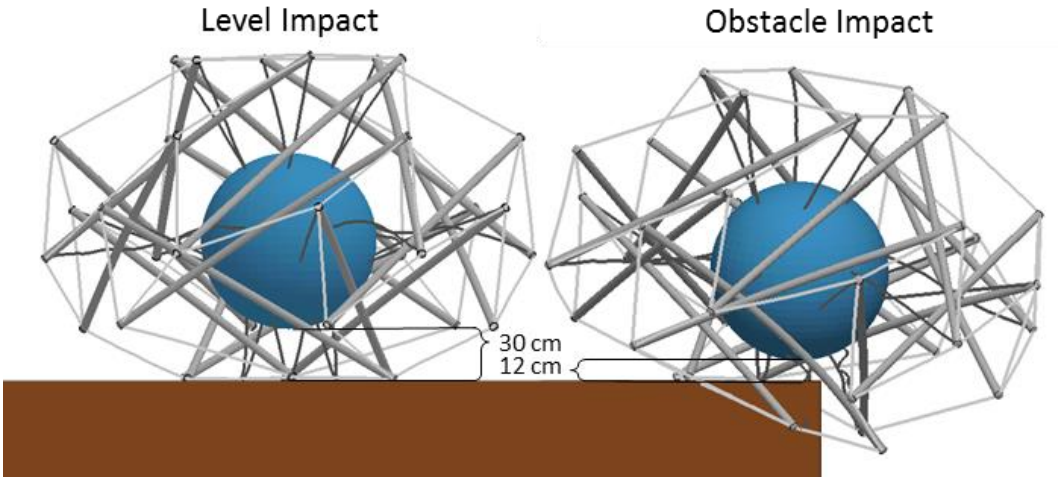

Figure 60 Comparison between impacting on a level surface versus impacting on an obstacle

Although the payload clearance was reduced, the impact load on the payload module were also reduced significantly as a result of impact on a non-level surface. As discussed above, in the level impact case, the impact shockwave is reflected off the top of the vehicle down into the payload module through the upper inner cables. However, because the landing surface in this case was non-level, the shockwave was not transmitted through axisymmetric load paths. Thus, when the shockwave reached the top face it had largely dissipated. As a result, the peak *g*-loading on the payload module was reduced by over 15 *g's*. Figure 61 shows a comparison of the impact loads for the level impact case and the boulder impact case. Note that the results in Fig. 61 were obtained using the vehicle model which incorporates deformable compression members and a cable element refinement.

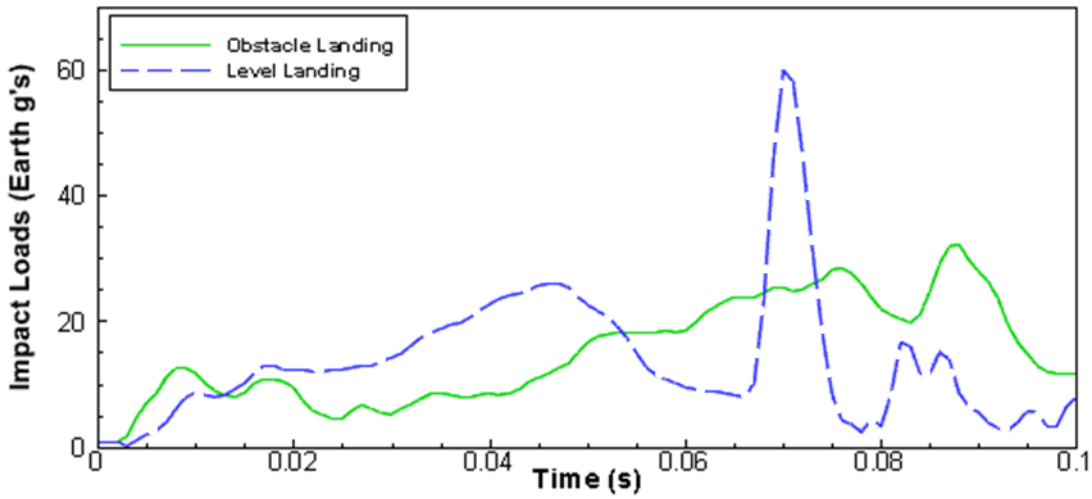

Figure 61 Comparison of the deceleration load related to impacting on a level surface and a non-level surface given a 180 *kg*

For the case where the larger lander impacted the surface, a scenario was selected where only two of the lower six compression rods contacted the impacting surface. As in the previous example, the uneven impact surface resulted in a significant reduction of impact loads. The payload module in this analysis saw a decrease of nearly 16 *g's* compared to the level impact case. However, in this case, when the vehicle impacted the surface one of the lower compression members struck the edge of the boulder. With the end points of the compression member constrained by the tension network, this non-axial load created a large bending load on the member, resulting the permanent deformation and local buckling of the beam. Figure 62 (a) shows the Von Mises stress on the vehicle as it impacts the boulder and Fig. 62 (b) shows the post impact deformation of the buckled compression member.

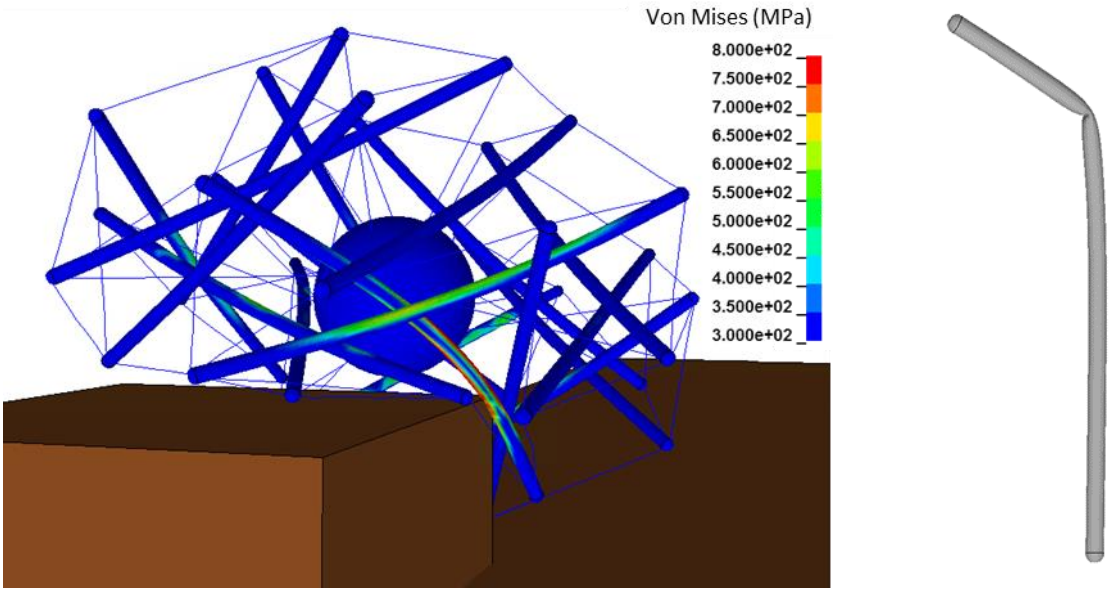

(a) (b)

Figure 62 Buckling of one compression member as a result of landing on an obstacle (a) Von Mises stress just before rod buckling occurred (b) post buckling shape of compression member

It is important to notice that even with the failure of a compression member, the stability of the tensegrity structure remained largely unaffected, and the payload module remained isolated and protected. As shown in Fig. 63, after the bounce, when the vehicle impacted the surface again, no negative impact characteristics were noticed due to the buckled compression member. This is due to the redundancy inherent in the tension network. Even when one component is damaged or removed, the loads are redistributed through the tension network so that the payload is protected.

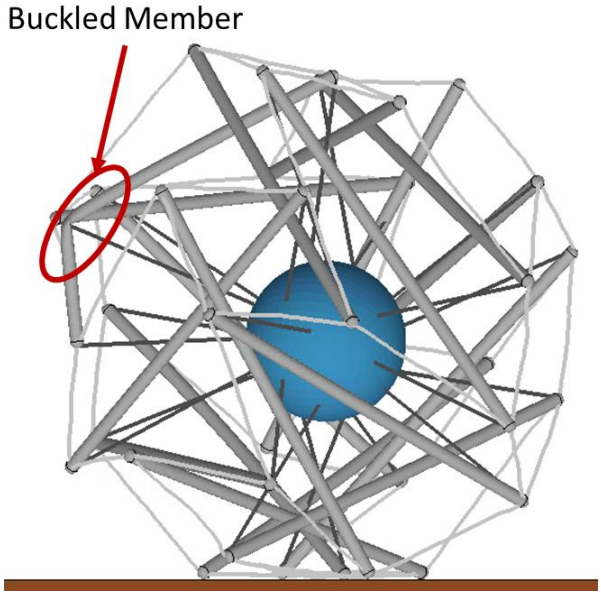

Figure 63 TANDEM protects the payload even with the failure of a compression member

Chapter 6

Control and Locomotion Investigation

Because TANDEM is designed around a tension network, control is a nonlinear problem. The length of each tension member in TANDEM is controlled by a stepper motor, but the position and orientation of the cable is dependent on the position and orientation of the tension and compression members connected to it as discussed in Chapter 4. The TANDEM structure is rotationally symmetric about its vertical-axis, as can be seen in Fig. 64. In this study it was decided that the baseline model of TANDEM would be comprised of six sections. However, alternate versions of TANDEM can be developed by increasing or decreasing the number of rotational sections based on the mission requirements. Three types of control strategies were developed in this work in order to change the configuration of the vehicle throughout a given mission. Each of these strategies is used for different maneuvers throughout the EDLL sequence. The control strategies were classified into categories based on the type of configuration change desired. These classifications were titled: CG offset, symmetric, and non-symmetric.

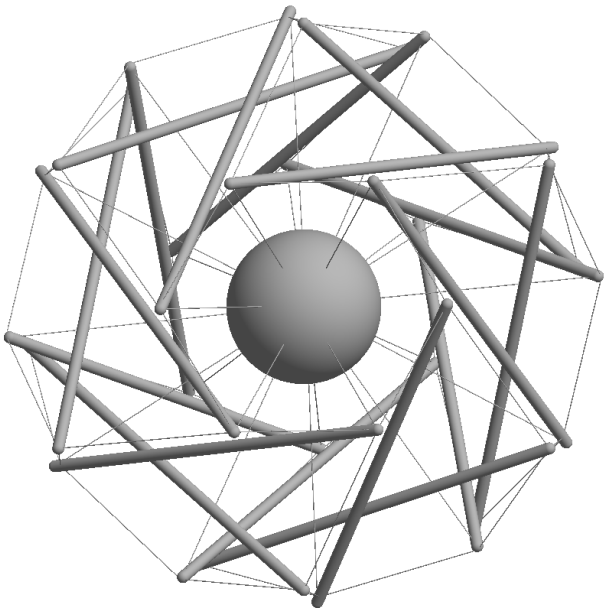

Figure 64 Top view of TANDEM vehicle reveals that it is rotationally symmetric

CG offset

The CG offset maneuver can be used on entry to create a non-zero lift to drag ratio. Additionally, it can be used on descent to steer the vehicle in various directions. The CG offset maneuver is mechanically the simplest of the available control strategies, because it does not require reconfiguration of the outer tensegrity structure. Because the outer structure is already a stable tensegrity structure in itself, the inner cables can be adjusted independently of the outer cables. This enables direct control of the position of the payload module, and thus the CG of the entire system, by controlling only the inner cables.

For these control methods, dynamic stability is a crucial parameter. If a non-zero L/D is desired for entry, the vehicle can no longer be spin stabilized. This will require further analysis to ensure static and dynamic stability, however, direct control of the vehicles CG suggest that stability can be achieved by simply decreasing the distance between the payload module and the nose cone. Additionally, it has been shown previously that blunt-body and open-backed geometry of deployable entry vehicles may provide a better dynamic stability at low Mach numbers than traditional entry vehicles. This is suggested by the IRVE flight tests [147] and discussed by Yount et al. [148].

At subsonic velocities, after the heat shield is dropped, the CG offset is used guide the vehicle to a specific target. In conjunction with the descent imager, the CG offset maneuver will enable the vehicle to perform some simple hazard avoidance. As was shown in the CFD discussion of Chapter 4, in free fall, the vehicle has a tendency to spin at angular velocities up to 3.53 *rad/s*. That spin rate is a function of the inclination of the rods in the structure. So it follows that the spin rate can be cancelled out by tuning the vehicle's geometry to a configuration that does not induce excessive angular rates. If that rate of spinning is maintained with the drag-plate on it will make to descent stage largely uncontrollable. Such a high spin rate will also render the descent camera unusable which will hinder the scientific return of the mission.

Additional CFD investigations should be performed to understand how the vehicle behaves on descent and identify any configurations that can be used to negate or maintain a low spin rate. However, if no such configuration can be found, the TANDEM concept will still be viable by replacing the flexible drag-plate with a parachute. Even in this situation, the descent may still be able to be guided by integrating the cables of the parachute in to the tension membrane. This will enable the vehicle to steer the parachute similar to how a skydiver can pull on different side of a parachute to navigate towards a desired location.

Symmetric control

Symmetric control strategies are slightly more difficult. Symmetric configurations are used in transitional stages of the EDLL sequence, e.g. the deployment of the heat shield or the transition from the deployed configuration to the descent configuration. In these transitions, each rotational section of the

structure must go through the same configuration change. This significantly reduces the number of degrees of freedom available in the system. There are 3 rods, 9 outer cables, and 4 inner cables in each periodic section. Figure 57 shows a single section of the tensegrity structure. For simplicity of the diagram, the cables connecting the payload module to the outer tensegrity structure (i.e. the inner cables) were omitted.

For symmetric configuration changes, the primary goal is to transition the vehicle's shape to prepare for the next stage of the EDLL sequence. Assuming that the vehicle's current configuration and its desired configuration are known, the input required of each stepper motor can be calculated using the form-finding algorithm, discussed in Chapter 4. The form-finding algorithm uses the length ratio of each tension member in a rotational section as input and delivers the tension member's position, orientation, and actual length. By linearly varying the input parameters from the initial configuration to the final configuration, the form-finding algorithm provides nonlinear changes in tension member lengths. This provides the input parameters required for each actuator in order to control the shape of the structure from one stable configuration to another. Figure 65 shows the change in length of each tension member for the symmetric transition from the stowed configuration to the deployed configuration. Each bar in Fig. 65 shows the transition of an individual tension member from the initial configuration to the final configuration. As can be seen in Fig. 65, the length of each cable varies nonlinearly as the configuration of the vehicle changes.

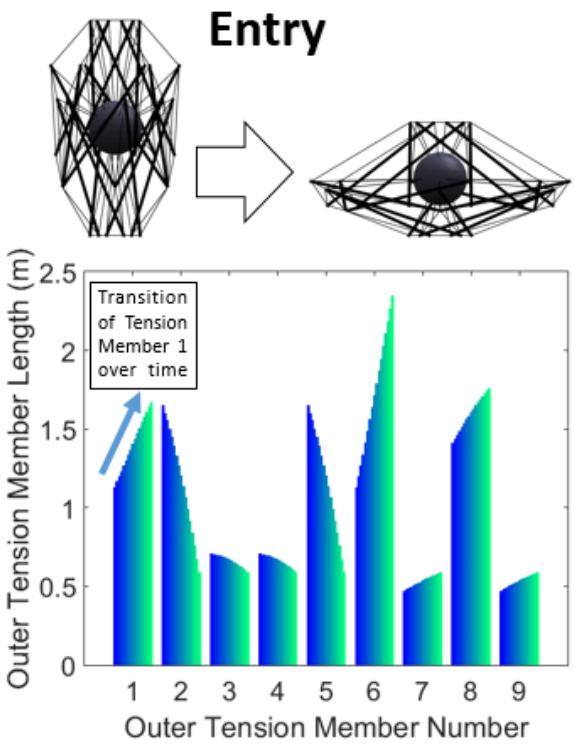

Figure 65 Nonlinear transition of cable length from the stowed to the deployed configuration

Figure 66 shows the change in tension member length for two other symmetric configuration changes. The configuration change of TANDEM before entry, descent, and landing make up the three primary uses of the symmetric control strategy.

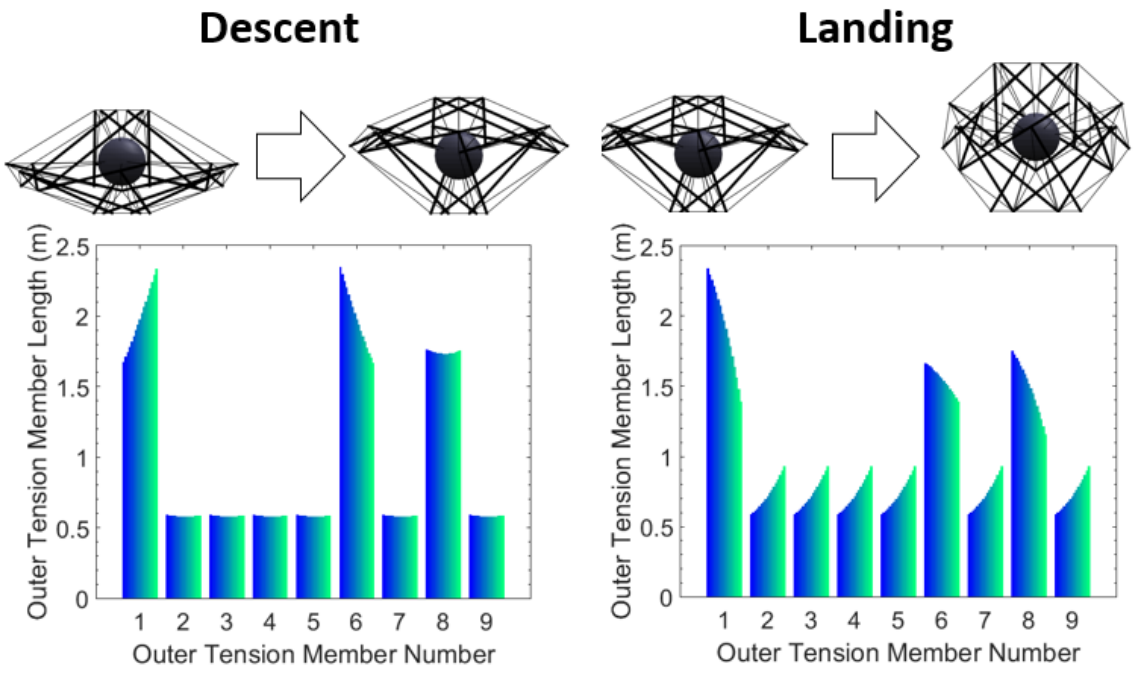

(a) (b)

Figure 66 Variation of cable lengths used in the symmetric configuration change before (a) descent and (b) landing

Non-symmetric control

Non-symmetric control is the most challenging. Lastly, non-symmetric configuration changes are predominantly used in on-the-ground locomotion. Unlike the symmetric configuration changes, the non-symmetric control strategies must account for the dynamics of the configuration change. The typical goal of non-symmetric configuration changes is for the implementation of surface locomotion through a variety of gaits. For gait development and simulation, the NASA Tensegrity Robotics Toolkit (NTRT) simulator was used[149,150]. NTRT was developed largely by the Dynamic Tensegrity Robotics Lab at NASA Ames for research on the design and control of tensegrity robots. NTRT is a tensegrity simulator built to run in the Bullet Physics Engine, version 2.82. While fully developed control system and advanced gait study are outside of the scope of this work, a gait development methodology was selected and discussed below. Additionally, a demonstration of a simple rolling gait is presented as proof of concept for surface locomotion.

As a preliminary investigation, an icosahedron tensegrity structure was considered. As each cable in the structure is a single degree of freedom, the icosahedron structure only had 24 DOF compared to the 78 DOF in the baseline TANDEM structure. Both of these structures are, however, too complex for a classical revers kinematics approach. By linearly varying various cables on the icosahedron structure, a simple gait was developed for forward motion, as shown in Fig. 67. Figure 68 shows which cables were varied and in which order.

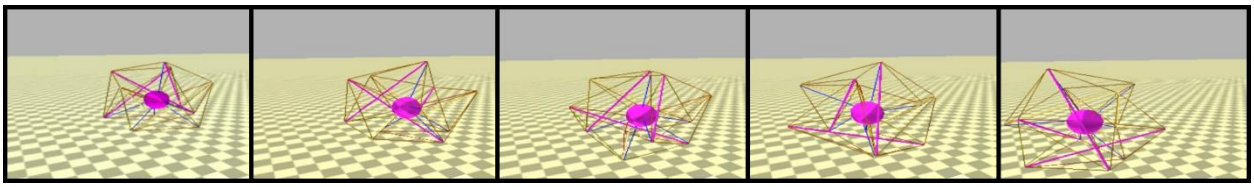

Figure 67 Example gait of straight forward motion for the icosahedron structure

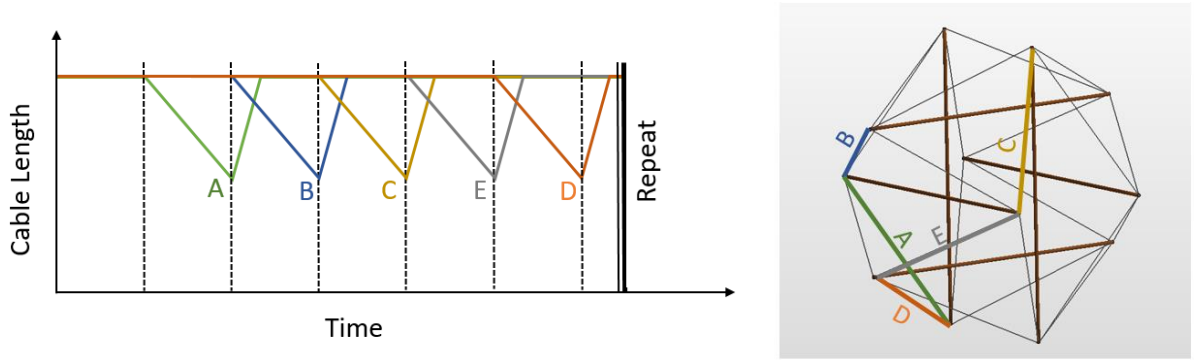

(a) (b)

Figure 68 A simple gait for forward motion of the icosahedron structure (a) basic pattern of how the cable lengths were varied (b) legend for which members were varied

This same approach was used to develop a preliminary gait for TANDEM. The preliminary locomotion kinematics are shown in Fig. 69. The rolling gait demonstrates simple locomotion for traversing flat surfaces. There are three steps in the rolling gait. The first step is to raise the CG of the vehicle by reeling in the upper inner cable and unspooling the lower inner cables (frame 1). Next, the inner lateral cables are used to shift the payload module a small amount in the desired direction of locomotion. The shift in the vehicle's CG causes the rover to begin to fall over (frame 2). After the vehicle had rolled onto its side, the bottom circumferential cables were extended, allowing the vehicle to roll further (frame 3). As a result of this maneuver, the vehicle rolls 180° such that it rests on its top face (frame 4). The procedure can then be repeated by reversing the roles of the upper and lower cables.

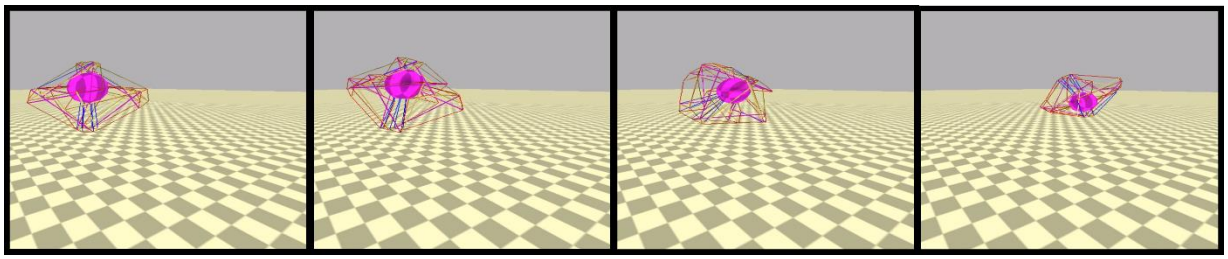

Figure 69 Time-lapse of preliminary locomotion study

The locomotion gait presented above is sufficient for this work, however future development will require more advanced methods for developing gaits. Ongoing work focuses on utilizing NTRTs controller libraries to implement Central Pattern Generators and machine learning frameworks to develop advanced locomotion gaits.

Gait Development for Advanced Locomotion using Neural Networks and Central Pattern Generators

Central Pattern Generators, or CPG's, are neurons involved in motor control, which are used to create a rhythmic pattern. These rhythmic patterns express some of the ways that a basic process can be repeated over time. Examples of these rhythmic patterns are seen in nature for various types of locomotion include walking, swimming, or flapping flight. In most living organisms, neurons in the central nervous system act as the CPG to engage in these movements [151]. These same rhythmic patterns are of great interest as a method to control autonomous vehicles, such as our TANDEM tensegrity structure.

For the TANDEM application model, a central circuit generates the rhythmic patterns for each motor neurons to excite the muscles (or actuate the tension members) and produce movement. Each CPG node corresponds to each actuator within the structure. In this configuration, the CPG generates gaits based on the connectivity of each node and the differences in phase between the compression members and the supporting tension members. The governing equations for each CPG node, i, in this system are listed below as a function of its relationship to each of its neighboring nodes, j.

$$\dot{\theta}_i = 2\pi v_i + \sum_j r_j w_{ij} \sin(\theta_j - \theta_i - \varphi_{ij}) \tag{29}$$

$$\ddot{r}_i = a_i \left[\frac{a_i}{4} (R_i - r_i) - \dot{r}_i \right] \tag{30}$$

$$v_i = r_i(\cos(\theta_i)) \tag{31}$$

Equation (29) is used to determine the phase of the CPG and Eq. (30) determines the amplitude. The overall velocity of the impedance controller is determined by Eq. (31). In these equations v_i is a

frequency term, r_j represents the amplitude of the coupled node, w_{ij} is the coupling weight and φ_{ij} is the phase offset. Furthermore, R_i is a set point for amplitude, a_i is a positive constant, R_i and v_i are each one parameter, or represent the combination of an offset, a gain, and the command itself [152].

In order to select these CPG constants, a Monte Carlo simulation will be used to vary the CPG constants over a predefined range. The effectiveness of each set of constants will be measured by the overall displacement of the center of mass of the structure over a finite length of time. The energy imparted to the system may also be considered in the selection of the most effective gait developed by the Monte Carlo run. After the design space is explored by the Monte Carlo simulation, a genetic algorithm will be used to iterate on the best result from the Monte Carlo, to see if a better set of constants can be found.

Locomotion in rough terrain using tensegrity robotics is a field of active research. Any larger scale exploration in the Ovda Regio or other tessera region using tensegrity structures would increase the complexity of the mission. It is likely that a library of rhythmic gaits will be implemented into a motion planning algorithm for most situations. A more controlled approach, like inverse kinematics, may be utilized if the terrain is especially challenging. However, a short mission, like the one proposed in the following chapter, may only require basic gaits, such as forward rolling and turning as it is not expected that a large verity of landscapes will be crossed in a few 2-4 hour mission.

Chapter 7

Conceptual Mission to Venus

This work resulted in a detail design of the TANDEM vehicle which was compared to the VITaL, ADEPT-VITaL and the baseline Venera Class Lander from Chapter 2.The design of a TANDEM vehicle, like many EDL concepts, is an iterative process. There are two sections in the EDL sequence where the vehicle is exposed to a high *g*-loading: during entry and on landing. In order to achieve an efficient design, it is important that neither the entry vehicle nor the lander/rover be over-designed. Thus, the vehicle should be designed such that both of these *g*-loadings should be approximately equal to each other.

For a ballistic entry, it is important to notice that the trajectory functions provided in Eq. (7) are functions of the ballistic coefficient (β_{entry}) and not a detailed design of the vehicle. Thus, a preliminary flight mechanics analysis is performed with β_{entry}=47 *kg/m*^{2}. Given an entry velocity of 10.8 *km/s* and an entry flight path angle (EFPA) of 8.5°, the FMC predicted a trajectory with an entry *g*-loading of 25 Earth-*g's*. Approximate ballistic coefficients of $\beta_{descent}$=45 *kg/m*^{2} and β_{lander}=1900 *kg/m*^{2} are assumed to calculate the terminal velocity of the vehicle at various stages of the descent to the surface. Due to the very low ballistic coefficient of the descent stage, it could reach terminal velocity as low as 3.5 *m/s*, but when the backshell is released the lander will accelerate to a velocity of 23 *m/s*. Figure 70 shows the details of vehicle trajectory.

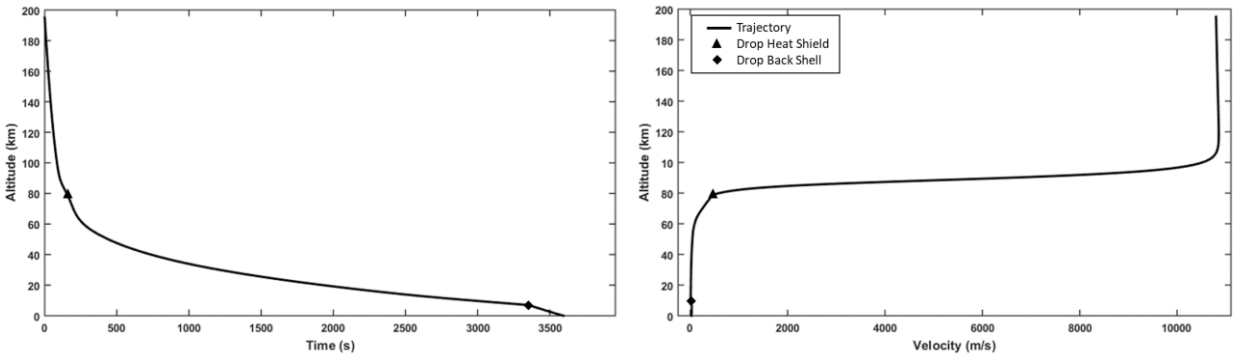

(a) (b)

Figure 70 The descent history of the detailed vehicle concept (a) altitude versus time (b) altitude versus velocity

Scientific Instruments and Payload Module

The payload module selected for this mission was the same design as used for the VITaL mission concept [20]. This payload module was selected for a number of reasons. The included instrument suite was carefully selected to answer as many Decadal Survey question as possible. Furthermore, the uses of the same payload module enable a direct comparison to be made between the VITaL concept and TANDEM. All of the instruments, except Raman/LIBS, currently exist at a high TRL and can be designed to survive an extended exposure to 200 *g's*, the load expected during entry in the VITaL mission.

Part of the reason that the Raman/LIBS is at a lower TRL than the other instruments is because it was expected to measure surface composition from 2.5 *m* away. This distance combined with the high entry loads of the VITaL entry, create a substantial design problem. The VITaL cost estimate set $20M for technology development, with most of this cost being attributed to the development of the Raman/LIBS [20]. The use of TANDEM can substantially simplify the design requirement surrounding the Raman/LIBS. Firstly, as the entry loads with TANDEM are 30 *g's*. Furthermore, because TANDEM can move on the surface, the Raman/LIBS will not need to make measurement from 2.5 *m* in order to get a wide sampling distribution. These two aspects of TANDEM greatly reduces the sensitivity required for that instrument's operation and will thus accelerate the elevation of its TRL. Figure 71 shows a section cut of the payload module. As it was designed in the VITaL mission, each of the shelves contain a phase changing material, that is used to absorb and thermal waste created by the electronic inside.

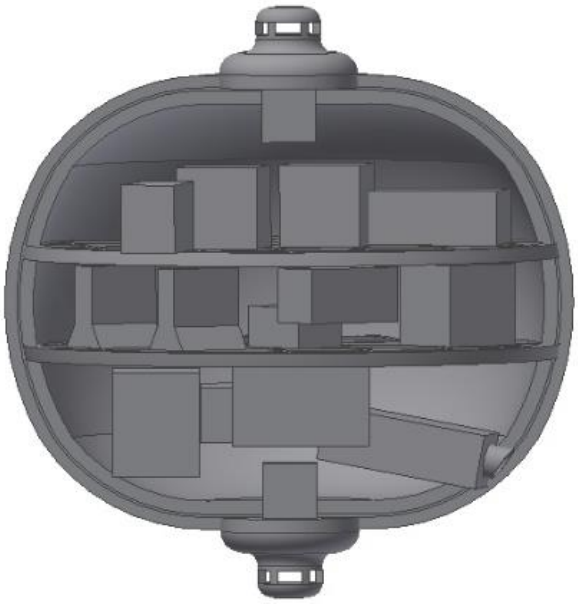

Figure 71 Section cut of the payload module based on [20]

Vehicle Design

As the terminal velocity and payload module for this first iteration was similar to that of model developed for the 20 *m/s* impact with a 260 in Chapter 5, the same lander design was used. With the design of the lander fully defined, the entry vehicle was developed. Many of the values used to define the TANDEM aeroshell were based on the similarly designed heat shield from the ADEPT-Vital mission [4]. The length of the heat shield ribs and the diameter of the entry vehicle were scaled in order to match the ballistic coefficient of the preliminary run. The final diameter of the deployed heat shield was 4.5 *m* with a cone angle of 70° and rib lengths of 2 *m*. Table 15 contains a mass breakdown of the whole TANDEM vehicle. The "Overall Deployment System" is an additional motor-driven cable system for the pretensioning of the heat shield. This deployment should be entirely covered by the locomotion system. However, the system was included in the design of TANDEM as an additional margin if the locomotion motors do not produce sufficient torque to fully pretension the heat shield to the required tension.

Table 15 TANDEM's master equipment list. Many values relating to the aeroshell were based off of values from the ADEPT-VITaL concept[4]

	TANDEM		
	CBE	Growth	Predicted Mass
Mass List	**1007 kg**		**1300 kg**
Aeroshell	**338**		**432**
Heat Shield	134		174
Nose Cap & Lock Ring	61	0.3	79
Ribs & Bearings	23	0.3	30
Joint Hardware	10	0.3	13
Carbon Cloth	40	0.3	52
Rigid Nose TPS	71		85
Nose TPS	50	0.2	60
Ribs TPS	12	0.2	14
Aft Cover TPS	9	0.2	11
Backshell	30	0.3	39
Mechanisms & Separation	86		112
Overall Deployment System	60	0.3	78
Stowed/Deployed Latched	19	0.3	25
Avionics & Power	17		22
Avionic Unit	4	0.3	5
Harness	5	0.3	7
Power Unit	8	0.3	10
Lander	**669**		**868**
Scientific Payload	37	0.3	48
Thermal	66	0.3	85
Power	12	0.3	16
Comm, Avionics & Electronics	24	0.3	32
Structure	120	0.3	154
Landing System	410	0.3	533

A common practice in concept design work is to add a 30% growth margin to the original design as seen done in Table 15. This added margin will affect the ballistic coefficients of the vehicle. To insure that the aerothermodynamic fluxes and loads are not excessively increased the radius of the deployed heat shield was increased by 10 *cm* to return the entry vehicle back to a ballistic coefficient 47 kg/m^2. With the TANDEM vehicle fully developed, the flight mechanics code was run using the predicted masses from Table 15. During entry, the modified Newtonian method was used to calculate the aerodynamic loads on the heat shield. Figure 72 (a) shows that the entry membrane needs to be able to withstand at least 35 *kPa* on entry. While Fig. 72 (b) shows a peak heat flux of 275 W/cm^2 and a total heat load of 8000 J/cm^2.

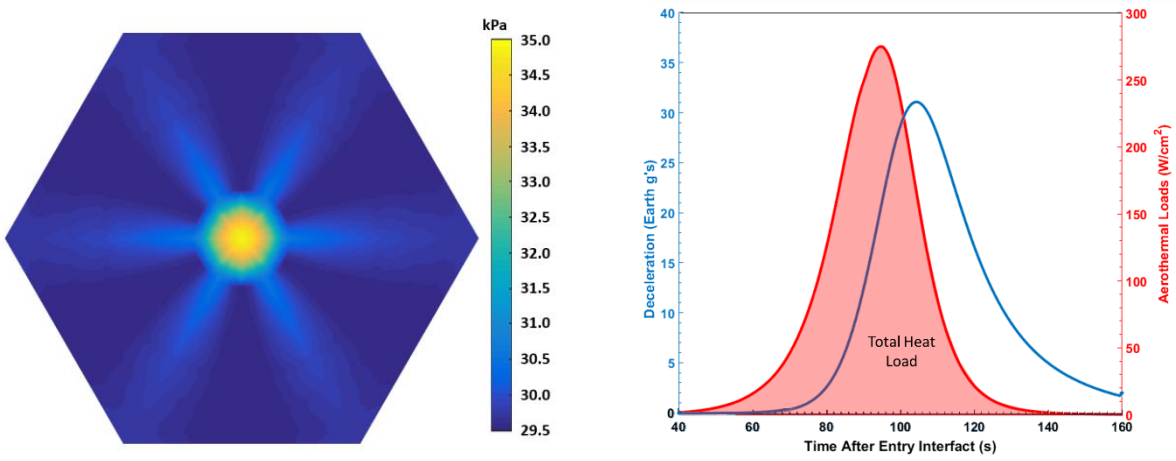

(a) (b)

Figure 72 Results from the flight mechanics code (a) maximum aeroloads at peak deceleration. (b) *g*-loading and aerothermal loads

The 30% mass margin did increase the terminal velocity of the vehicle to *25 m/s* as predicted in Chapter 6 using CFD. With the added mass margin and the new terminal velocity, a new impact analysis was performed. Figure 73 show the Von Mises stress plot of the compression members at the time of max stress. The maximum stress in the compression members was 800 *MPa*.

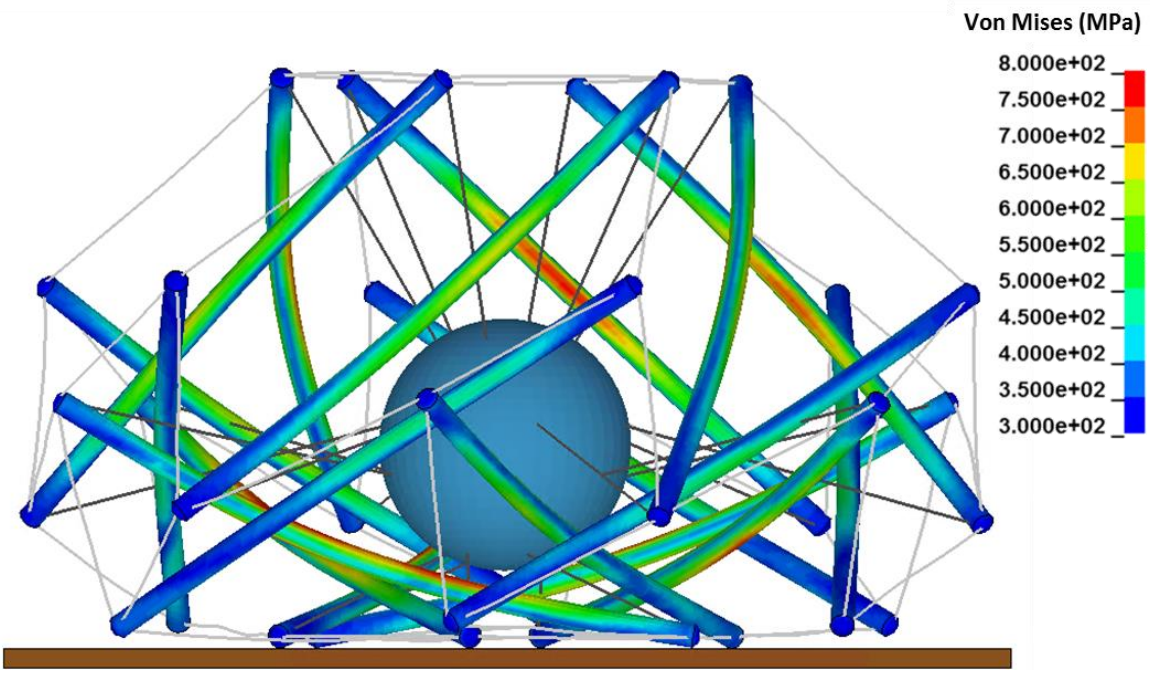

Figure 73 Von Mises stress on compression members for the impact of predicted mass model

Figure 74 show the magnitude of the impact loads experienced by the payload module. The max *g*-load on the payload was 129 *g's*. While this is nearly double the max deceleration experienced on entry, its duration is significantly shorter that the loads experienced in launch and entry. Due to the brevity of the

impulse no damage is expected to be inflicted on the scientific payload. Additionally, it is known that this is a conservative prediction. Based on a correlation from the physical drop test experiment the actual peak loading may be as low as 105 *g's*.

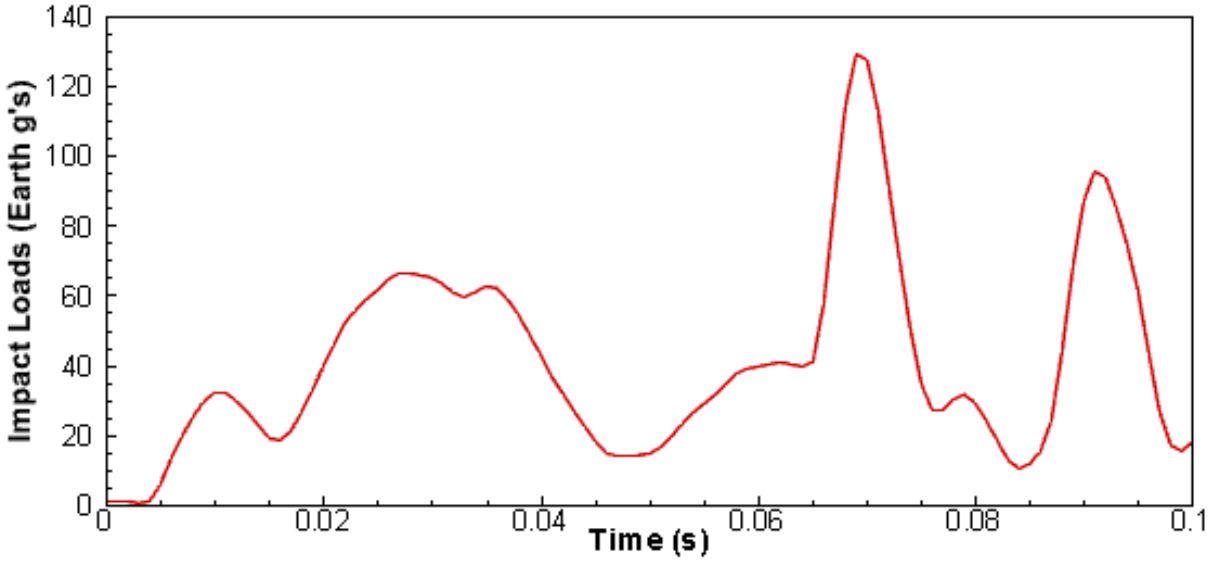

Figure 74 Deceleration of the payload module of the predicted mass vehicle at 25 m/s

As discussed previously, the landing environment of the Ovda Regio was the primary risk of the VITaL mission. This was not primarily due to the macro-scale slopes, but due to the steep and abrupt ribbon structures as well as any undetectable small scale formations such as large boulders. These structure present a substantial risk and typically will lead to mission failure for a mission using a classical lander design. However, it has been shown that the TANDEM vehicle is capable of safely landing despite these structures, although these structures do still present some risk and should be avoided during landing.

Even if TANDEM were to land in a crevice, hole, or small crater, this will not necessarily lead to mission failure as it would with most other concepts. For a mission using TANDEM, the tensegrity structure should be able to protect the scientific payload. This event may limit the locomotion capabilities of the vehicle, and communication with the cruise stage or orbiter may be blocked by the landscape for some orientations, but the probe should be able to continue its scientific experiments like normal and in some cases, the vehicle maybe even be able to climb out of the hole.

Comparison of the TANDEM lander to Venera Class Landers

In order to show the merit of the TANDEM concept a direct comparison was made between TANDEM and a state of the art Venera Class Lander for the same mission. For missions with a flat expected landing surface, it has been shown that the mass of a Venera-class lander can be reduced to approximately

500 *kg* [1] given the same 260 *kg* payload module as used in this study. For missions to the Tessera regions with heavily deformed terrain, the Venera Class Lander design will approach the significantly heavier VITaL lander design. This is because additional mass is required to maintain a low center of gravity and prevent the lander from tipping over. In these uneven and steep landing environments, the tensegrity landers become more mass efficient than Venera Class Landers. A comparison of TANDEM to three different Venera Class Landers is provided in Table 16. The data shown in Table 16 represents the CBE data for all cases.

Table 16 Comparison of TANDEM to various Venera Class landers

	TANDEM (CBE)	Venera Class Baseline [1]	ADEPT-VITaL [4]	VITaL [20]
Payload Module**	150 *kg*	150 *kg*	149.2 *kg*	174 *kg*
Structure	110 *kg*	240.5 *kg*	212.3 *kg*	283 *kg*
Landing System	410 *kg*	105 *kg*	452.3 *kg*	603 *kg*
Total	670 *kg*	495.5 *kg*	813.8 *kg*	1060 *kg*
Terminal Velocity	23 *m/s*	7.87 *m/s*	Not Reported	9.0 *m/s*
G-Loading	96 *g's*	92 *g's*	Not Reported	83 *g's*

*** Note: The payload module mass is comprised of scientific experiments, communications, insulation, phase changing materials and power. Unlike other locations in this dissertation, the mass of the pressure vessel is included in the structures section and is not included in the mass of the Payload Module.*

The benefit of using deployable heat shield is clearly demonstrated by Smith et al. [4], which was able to reduce the landed mass of a Venera Class Lander by nearly 250 *kg*. TANDEM preserves the benefits that was provide by ADEPT while reducing the landed mass by an additional 144 *kg*. This mass savings is a direct response of replacing the Venera Class lander design with the tensegrity lander design that is used by TANDEM.

Notice that the tensegrity design is not always the lowest mass option. The Venera Class Baseline design was more than 170 *kg* lighter than the TANDEM design for the same payload. This is because TANDEM is designed to have excellent crashworthiness in the most extreme landing cases, whereas the baseline design was designed to show the minimum mass required to land on a flat surface. The mass of the TANDEM vehicle is driven by its impact velocity. All of the Venera Class landers shown in Table 16 were equipped with drag-plates and have a touchdown velocity of approximately below 10 *m/s*. TANDEM, on the other hand, impacts at 23 *m/s* for the CBE design, resulting in roughly the same *g*-load for both concepts (depending on vehicle orientation and landing surface slope).

As shown in Chapter 5, the mass of the lander will decrease linearly with landing velocity. One method of decreasing the landing velocity is by keeping the backshell on during touchdown. Because the

descent stage has such a low terminal velocity (as low as 3 *m/s*), it is not expected that the backshell will interfere with the landing sequence. The backshell can then be removed afterwards as the rover begins to roll on the surface. As the current vehicle design was driven primarily by the impact speed, if the landing speed of the rover is decreased, the vehicle mass could be reduced by 45% or more. This design would not be as robust as the original TANDEM design, but it may prove to be a valuable concept for destinations with fewer terrain risks.

Given that the TANDEM lander is in the same range of mass efficiency as the traditional Venera-type design, though noticeably lighter for rougher terrains, the next figure of merit to discuss is locomotion. The capability for locomotion expands the scientific exploration even for short-term missions. TANDEM eliminates the risk associated with immobility while enabling the lander to fully investigate the landing site, resulting in a more complete picture of the area. It enables scientists to remotely interact with the environment and select regions of interest for focused investigation.

Comparison of TANDEM to ADEPT and VITaL

Although TANDEM and ADEPT use fundamentally the same heat shield, the full aeroshell design is very different. Because TANDEM's tensegrity structure provides the frame for the heat shield, a number of component in the ADEPT design are eliminated. Table 17 compares the mass breakdown of both TANDEM and ADEPT to highlight the differences between the two. What makes TANDEM unique is the integration of the landing and locomotion systems into the entry and descent stages of the EDLL sequence. This is where the biggest benefits can be found.

Table 17 Comparison of mass breakdown for TANDEM, ADEPT-VITaL [4]**, and VITaL** [20]

	TANDEM			ADEPT-VITaL [2]			VITaL [3]		
	CBE	Growth	Predicted Mass	CBE	Growth	Predicted Mass	CBE	Growth	Predicted Mass
Total Mass	**1007 kg**		**1300 kg**	**1621 kg**		**2100 kg**	**2102 kg**		**2746 kg**
Aeroshell	**338**		**432**	**807**		**1042**	**1051**		**1366**
Heat Shield	134		174	484		629	718		933
Main Body	-	0.3	-	233	0.3	303	233	0.3	303
Nose Cap & Lock Ring	61	0.3	79	61	0.3	79	-	0.3	-
Ribs & Bearings	23	0.3	30	46	0.3	60	-	0.3	-
Struts & End Fit	-	0.3	-	42	0.3	55	-	0.3	-
Joint Hardware	10	0.3	13	10	0.3	13	-	0.3	-
Carbon Cloth	40	0.3	52	92	0.3	120	-	0.3	-
Rigid Nose TPS	71		85	71		85	-		-
Nose TPS	50	0.2	60	50	0.2	60	-	0.2	-
Ribs TPS	12	0.2	14	12	0.2	14	-	0.2	-
Aft Cover TPS	9	0.2	11	9	0.2	11	-	0.2	-
Backshell	30	0.3	39	30	0.3	39	293	0.3	381
Mechanisms & Separation	86		112	205		267	40		52
Overall Deployment System	60	0.3	78	54	0.3	70	-	0.3	-
Stowed/Deployed Latched	19	0.3	25	19	0.3	25	-	0.3	-
Aeroshell Separation Ring	-	0.3	-	30	0.3	39	30	0.3	30
Separation Guild Rails	-	0.3	-	45	0.3	59	45	0.3	45
Backshell Sep	7	0.3	9	7	0.3	9	7	0.3	7
Parachute System	-	0.3	-	50	0.3	65	50	0.3	50
Avionics & Power	17		22	17		22	-		-
Avionic Unit	4	0.3	5	4	0.3	5	-	0.3	-
Harness	5	0.3	7	5	0.3	7	-	0.3	-
Power Unit	8	0.3	10	8	0.3	10	-	0.3	-
Lander	**669**		**868**	**813.7**		**1058**	**1061**		**1379**
Scientific Payload	37	0.3	48	37	0.3	48	49	0.3	64
Thermal	66	0.3	85	65.5	0.3	85	77	0.3	100
Power	12	0.3	16	12.3	0.3	16	12	0.3	16
Comm, Avionics & Electronics	24	0.3	32	24.3	0.3	32	27	0.3	35
Structure	120	0.3	154	222.3	0.3	289	293	0.3	381
Landing System	410	0.3	533	452.3	0.3	588.0	603	0.3	783.9

The predicted mass of the mission is reduced by approximately 800 *kg* after switching from the ADEPT VITaL design to the TANDEM design (for the predicted mass estimate). Of this mass savings, only about 100 *kg* was contributed by the decrease in heat shield diameter. The heat shield diameter was reduced in this mission concept to ensure that the TANDEM design and the ADEPT-VITaL design maintained the same entry ballistic coefficient, despite the TANDEM lander being significantly lighter than the VITaL lander. The change of lander designs resulted in a predicted mass reduction of 190 *kg*. This 290 kg mass reduction is what would be expected for some mission that just uses a tensegrity lander and the ADEPT entry vehicle without integrating the two vehicles into a single vehicle as TANDEM does. Such a mission would likely have similar crashworthiness for landing but would not be able to provide the numerous benefit that TANDEM does for entry and descent. In addition to the maneuverability that comes

as a direct result of integrating the lander into the entry vehicle design, TANDEM is an additional 510 *kg* lighter than the expected mass of such an unintegrated tensegrity-ADEPT mission. This dramatic mass reduction comes directly from combining these two vehicles together and highlights the unique feature of TANDEM.

Conclusion and Contributions

The proposed TANDEM concept provides a high level of adaptability and controllability, which can be utilized throughout the EDLL sequence. This opens the door to a whole world of new maneuvering options during EDLL, including lifting/guided entry, guided descent, and hazard avoidance. Beyond the controllability and maneuverability that TANDEM displays on entry and descent, it is designed to land at any orientation and can traverse significantly rougher terrain then previous rovers. This means new landing sites can be reached. Instead of landing in low risk areas then traveling to the closest area of scientific interest, missions using TANDEM can land directly in the region of interest.

As part of these investigations, a system capable of performing landed science in the Tessera region has been developed. Through impact analyses and physical drop test experiments the crashworthiness of the TANDEM structure has been established. It has been demonstrated that even in the worst landing conditions, if TANDEM is damaged, the tension network is still able to protect the scientific payload. These are promising results that indicate TANDEM can safely enable landed science in the Tessera regions.

Furthermore, it has been demonstrated that the TANDEM concept, provide a substantially larger payload to mass ratio compared to other VISE mission concepts. As a result, the mass of a mission utilizing the TANDEM vehicle can be drastically reduced and as a direct result so can the overall cost of the mission. With cheaper flight cost and a highly versatile design, the TANDEM architecture can be leveraged for rapid, robust, and efficient exploration of the Solar System.

The added functionality plus the mass efficiency of the TANDEM concept is balanced with an increase in complexity. The numerous benefits of linking all of EDLL together with a single multifunctional vehicle has been expounded on throughout this dissertation, however, this also strongly links the design process required for each of these mission segments. This can be a challenge for mission development. Furthermore, the complexity and low TRL of tensegrity locomotion does not lend itself well to long exploration missions in the near-term, but may prove to be a viable option for mid to far-term missions after the required technologies have been more fully explored.

For these reasons, TANDEM is most applicable for mission where landing is a primary mission risk. This may be the case when the local surface roughness is unknown because the celestial body has not been fully explored by previous missions or due to a thick atmosphere (as is the case for Venus or Titan).

Alternatively, the local surface roughness may be known to be too severe for traditional landers (such as when landing near large geological structures). TANDEM may also be a viable option for mission destinations that require a high touchdown velocity. This is expected, for example, in missions to the southern hemisphere of Mars, where the altitude is high and the atmosphere is too thin to fully decelerate.

For missions where the landing environment is not as severe, TANDEM may still be used to achieve a lightweight mission design. However, in these benign situations, little is gained by having a lander design that can land at terminal velocity for any orientation. Mission concepts with flight heritage may be more desirable in this case, as they will be at a higher initial TRL and will likely reduce the complexity of the mission development.

Contributions to the State of the Art

The unique multifunctional infrastructure is an innovative design that sets TANDEM apart from the current state of the art, but on top of the concepts functionality it has displayed a significant mass saving compared to other contemporary concepts. It was shown that the Predicted Mass of the TANDEM lander was 190 *kg* less that the Predicted Mass of the ADEPT-VITaL lander. Additionally, there was an 800 *kg* mass reduction of the whole entry vehicle compared to the ADEPT-VITaL mission. This body of work represents a successful hybridization of two new and promising technologies: Mechanically deployable entry vehicles and tensegrity robotics. The merging of these two technologies provides a significant step forward in the field of in-situ exploration of celestial bodies

As a result of this work:

1. A new class of lightweight, multifunctional planetary probes has been conceived and explored
2. TANDEM has shown that while it preserves the same benefits as ADEPT, it also enables multiple additional benefits including guided entry and descent, omnidirectional impact protection and surface locomotion at little to no added mass penalty
3. The detailed design of TANDEM a has shown a reduction of mission mass by 38% (800 *kg*) compared to the ADEPT-VITaL mission [4,3] and a 52% (1445 *kg*) mass reduction from the original VITaL mission [20]
4. It was demonstrated that the design of tensegrity structures, and TANDEM specifically, is linearly dependent on the impact velocity of the vehicle, with an offset equal to the mass of the payload module. This was previously unknown.
5. Investigation of surface impact revealed a promising results that suggest a properly configured TANDEM vehicle can safely land and preform science in the Tessera regions, which was previously labeled by the Decadal Survey as, “largely inaccessible” despite its high scientific interest [14].

6. The developed modeling methodology for simulating the high velocity impact of TANDEM was validated against drop test experiments of a quarter scale TANDEM prototype

Future Work

The work in this dissertation was focused on the low computation expense predictions and simulations, to rapidly analysis the proposed concept. Research and development on the TANDEM concept will continue, with an aim of refining the processes that were described in this work to increasing their fidelity and to increase the TRL of the vehicle. Four areas of research from this dissertation require additional research: launch, aerodynamics on entry and descent, vehicle control and gait development, and the development of mission critical high-temperature components. From these areas of interest five key tasks have been set for future investigation and is to be proposed to be accomplished in part the NIAC Phase II work. These tasks are as follows:

- A coupled loads analysis of the launch environment on an Atlas V-551
- In-depth investigation of hypersonic and subsonic aerodynamics through the use of high fidelity Computational Fluid Dynamics (CFD)
- Detailed mechanical design and small scale prototyping of entry vehicle
- Development of advance locomotion gaits through the use of Central Pattern Generators (CPGs) and machine learning and implementation in to a small scale prototype
- Development of radio transmitter/receiver capable of operating in Venus surface conditions (VSC) to enable wireless control of cable motors.

While TANDEM is a new concept with several avenues of exploration ahead of it, its foundation is firmly rooted in two established technologies currently being developed by NASA. Both tensegrity robots and semi-flexible deployable heat shields have been thoroughly investigated for their use in space exploration. Research in the ADEPT concept has resulted in a high technology readiness level (TRL) 3D woven heat shield, which can easily be adapted to TANDEM, while the up and coming field of tensegrity robotics has shown the efficiency and practicality of tensegrity landers. Altogether, the numerous benefits presented by this concept as well as the foundation of research that already exists for these two fields makes TANDEM a low-risk/high-reward research opportunity.

References

[1] Schroeder, K., Bayandor, J., and Samareh, J., 2017, "Sizing and Synthesis of Venera Class Landers," Submitt. to J. Spacecr. Rocket.

[2] Bayandor, J., Schroeder, K., and Samareh, J. A., 2016, "Lightweight Multifunctional Planetary Probe for Extreme Environment Exploration and Locomotion," NASA Innov. Adv. Concepts Phase I.

[3] Schroeder, K., Bayandor, J., and Samareh, J., 2017, "TANDEM, Tension Adjustable Network for Deploying Entry Membrane," Submitt. to J. Spacecr. Rocket.

[4] Smith, B., Venkatapathy, E., Wercinski, P., Yount, B., Prabhu, D., Gage, P., Glaze, L., and Baker, C., 2013, "Venus In Situ Explorer Mission Design Using a Mechanically Deployed Aerodynamic Decelerator," 2013 IEEE Aerospace Conference, IEEE, pp. 1–18.

[5] Venkatapathy, E., Arnold, J., Fernandez, I., Hamm, K. R., Kinney, D., Laub, B., Makino, A., McGuire, M. K., Peterson, K., and Prabhu, D., 2011, "Adaptive Deployable Entry and Placement Technology (ADEPT): A Feasibility Study for Human Missions to Mars," 21st AIAA Aerodynamic Decelerator Systems Technology Conference and Seminar, Dublin, Ireland, AIAA Paper.

[6] Stern, E., Barnhardt, M., Venkatapathy, E., Candler, G., and Prabhu, D., 2012, "Investigation of Transonic Wake Dynamics for Mechanically Deployable Entry Systems," Aerospace Conference, 2012 IEEE, IEEE, pp. 1–10.

[7] Smith, B. P., Yount, B. C., Venkatapathy, E., Stern, E. C., Prabhu, D. K., and Litton, D. K., 2013, "Progress in Payload Separation Risk Mitigation for a Deployable Venus Heat Shield," AIAA Aerodynamic Decelerator Systems Conference, Daytona Beach, FL.

[8] Smith, B., Cassell, A., Kruger, C., Venkatapathy, E., Kazemba, C., and Simonis, K., 2015, "Nano-ADEPT: An Entry System for Secondary Payloads," 2015 IEEE Aerospace Conference, IEEE, pp. 1–11.

[9] Skelton, R. E., 2002, "Structural Systems: A Marriage of Structural Engineering and System Science," J. Struct. Control, **9**(2), pp. 113–133.

[10] Chopra, S. D., Teodorescu, M., Lessard, S., Agogino, A., and SunSpiral, V., 2016, "Tensegrity Heat Shield for Atmospheric Entry Through Celestial Bodies," ASME 2016 Int. Des. Eng. Tech.

Conf. Comput. Inf. Eng. Conf.

[11] SunSpiral, V., Gorospe, G., Bruce, J., Iscen, A., Korbel, G., Milam, S., Agogino, A., and Atkinson, D., 2013, "Tensegrity Based Probes for Planetary Exploration: Entry, Descent and Landing (EDL) and Surface Mobility Analysis," Int. J. Planet. Probes.

[12] Hustig-Schultz, D., SunSpiral, V., and Teodorescu, M., 2016, "Morphological Design for Controlled Tensegrity Quadruped Locomotion," Intelligent Robots and Systems (IROS), 2016 IEEE/RSJ International Conference on, IEEE, pp. 4714–4719.

[13] Tietz, B. R., Carnahan, R. W., Bachmann, R. J., Quinn, R. D., and SunSpiral, V., 2013, "Tetraspine: Robust Terrain Handling on a Tensegrity Robot using Central Pattern Generators," Advanced Intelligent Mechatronics (AIM), 2013 IEEE/ASME International Conference on, IEEE, pp. 261–267.

[14] Squyres, S., and et al., 2012, Vision and Voyages for Planetary Science in the Decade 2013-2022, National Academies Press.

[15] Hunten, D. M., 1983, Venus, University of Arizona Press.

[16] Herrick, R. R., Stahlke, D. L., and Sharpton, V. L., 2010, "A New Data Set for Venus: Stereo-derived Topography for 20% of the Planet at km-scale Horizontal Resolution," Lunar and Planetary Science Conference, p. 1622.

[17] NASA/JPL, 1996, "PIA00085: Venus - Lineated Plains in Lakshmi Region" [Online]. Available: https://photojournal.jpl.nasa.gov/catalog/PIA00085. [Accessed: 11-Jul-2017].

[18] Lang, K. R., 2011, The Cambridge Guide to the Solar System, Cambridge University Press.

[19] NASA/JPL, 1996, "PIA00258: Venus - False Color of Eistla Regio" [Online]. Available: https://photojournal.jpl.nasa.gov/catalog/PIA00258. [Accessed: 11-Jul-2017].

[20] Gilmore, M., and Glaze, L., 2010, "Venus Intrepid Tessera Lander."

[21] Dolgopolov, V. P., Pichkhadze, K. M., and Sukhanov, K. G., 2012, "The Vega project: A space mission to Venus and Halley's Comet," Sol. Syst. Res., **46**(7), pp. 568–577.

[22] Ball, A., Garry, J., Lorenz, R., and Kerzhanovich, V., 2007, Planetary Landers and Entry Probes, Cambridge University Press.

[23] Oertel, D., Spänkuch, D., Jahn, H., Becker-Ross, H., Stadthaus, W., Nopirakowski, J., Döhler, W., Schäfer, K., Güldner, J., and Dubois, R., 1985, "Infrared spectrometry of Venus from 'Venera-15' and 'Venera-16,'" Adv. Sp. Res., **5**(9), pp. 25–36.

[24] Marov, M. I., and Grinspoon, D. H., 1998, The Planet Venus, Yale University Press.

[25] Bond, P., 2012, Exploring the Solar System, John Wiley & Sons.

[26] Soediono, B., and Kolawa, E., 2007, Extreme Environment Technologies for Future Space Science Missions, National Aeronautics and Space Administration, Jet Propulsion Laboratory, California Institute of Technology.

[27] Keldysh, M. V, 1977, "Venus Exploration with the Venera 9 and Venera 10 Spacecraft," Icarus, **30**(4), pp. 605–625.

[28] Kargel, J. S., Komatsu, G., Baker, V. R., and Strom, R. G., 1993, "The Volcanology of Venera and VEGA Landing Sites and the Geochemistry of Venus," Icarus, **103**(2), pp. 253–275.

[29] Garvin, J. B., Head, J. W., Zuber, M. T., and Helfenstein, P., 1984, "Venus: The Nature of the Surface from Venera Panoramas," J. Geophys. Res. Solid Earth, **89**(B5), pp. 3381–3399.

[30] Saunders, R. S., and Arvidson, R. E., 1991, "An Overview of Venus Geology," Science (80-.)., **252**(5003), p. 249.

[31] Marov, M. Y., 1978, "Results of Venus Missions," Annu. Rev. Astron. Astrophys., **16**(1), pp. 141–169.

[32] Ford, P. G., and Pettengill, G. H., 1992, "Venus Topography and Kilometer-Scale Slopes," J. Geophys. Res. Planets, **97**(E8), pp. 13103–13114.

[33] Ivanov, M. A., 2009, "Comparison of RMS Slopes of Terrestrial Examples and Tessera Terrain," Venus, 50th Brown Vernadsky Microsymp. Moscow, Russ.

[34] Connors, C., and Suppe, J., 2001, "Constraints on magnitudes of extension on Venus from slope measurements," J. Geophys. Res. Planets, **106**(E2), pp. 3237–3260.

[35] Campbell, B. A., and Campbell, D. B., 1992, "Analysis of Volcanic Surface Morphology on Venus from Comparison of Arecibo, Magellan, and Cerrestrial Airborne radar data," J. Geophys. Res. Planets, **97**(E10), pp. 16293–16314.

[36] Ghent, R., and Hansen, V., 1999, “Structural and Kinematic Analysis of Eastern Ovda Regio, Venus: Implications for Crustal Plateau Formation,” Icarus, **139**(1), pp. 116–136.

[37] Arnold, J. O., Laub, B., Chen, Y. K., Prabhu, D. K., Bittner, M. E., and Venkatpathy, E., 2013, “Arcjet Testing of Woven Carbon Cloth for Use on Adaptive Deployable Entry Placement Technology,” International Planetary Probe Workshop, pp. 17–21.

[38] Arnold, J. O., Peterson, K. H., Yount, B. C., Schneider, N., and Chavez-Garcia, J., 2013, “Thermal and Structural Performance of Woven Carbon Cloth for Adaptive Deployable Entry and Placement Technology,” 22nd AIAA Aerodynamic Decelerator Systems Technology Conference, pp. 25–28.

[39] Wercinski, P. F., Smith, B., Yount, B., Kruger, C., Brivkalns, C., Makino, A., Cassell, A., Dutta, S., Ghassemieh, S., and Wu, S., 2017, “ADEPT sounding rocket (SR-1) flight experiment overview,” Aerospace Conference, 2017 IEEE, IEEE, pp. 1–7.

[40] Dutta, S., Smith, B., Prabhu, D., and Venkatapathy, E., 2012, “Mission Sizing and Trade Studies for Low Ballistic Coefficient Entry Systems to Venus,” Aerospace Conference, 2012 IEEE, IEEE, pp. 1–14.

[41] Venkatapathy, E., and Ellerby, D., 2014, “Heat Shield for Extreme Entry Environment Technology for Near-Term Robotic Science Missions and Longer Term Human Missions,” LPI Contrib., **1795**, p. 8101.

[42] Fuller, R. B., 1962, Tensile-Integrity Structures US Patent: 3 063 521, 1962~ 11—13 [2013 ─ O4—01].

[43] Motro, R., 1992, “Tensegrity Systems: the State of the Art,” Int. J. Sp. Struct., **7**(2), pp. 75–83.

[44] Pellegrino, S., 1992, “A Class of Tensegrity Domes,” Int. J. Sp. Struct., **7**(2), pp. 127–142.

[45] Kawaguchi, M., Tatemichi, I., and Chen, P. S., 1999, “Optimum Shapes of a Cable Dome Structure,” Eng. Struct., **21**(8), pp. 719–725.

[46] Schaich, M., 2004, “The Messeturm in Rostock: A Tensegrity Tower,” J. Int. Assoc. Shell Spat. Struct., **45**(2), pp. 93–98.

[47] de Oliveira, M. C., and Skelton, R. E., 2005, “A New Topology of Tensegrity Towers with Uniform Force Distribution,” Smart Structures and Materials, International Society for Optics and

Photonics, pp. 198–208.

[48] Rhode-Barbarigos, L., Ali, N. B. H., Motro, R., and Smith, I. F. C., 2010, "Designing Tensegrity Modules for Pedestrian Bridges," Eng. Struct., **32**(4), pp. 1158–1167.

[49] De Boeck, J., 2013, "Tensegrity Bridges: Concept Design of Pedestrian Bridges using Tensegrity as Load Carrying System."

[50] Arup, 2010, "Kurilpa Bridge Case Study."

[51] Motro, R., 2003, Tensegrity: Structural Systems for the Future, Elsevier.

[52] Skelton, R. E., and de Oliveira, M., 2009, Tensegrity Systems, Springer Science & Business Media.

[53] Sultan, C., and Skelton, R., 2003, "Deployment of Tensegrity Structures," Int. J. Solids Struct., **40**(18), pp. 4637–4657.

[54] Warden, R. M., 1987, "Folding, Articulated, Square Truss."

[55] Belvin, W. K., Herstrom, C. L., and Edighoffer, H. H., 1989, "Quasistatic Shape Adjustment of a 15-meter-Diameter Space Antenna," J. Spacecr. Rockets, **26**(3), pp. 129–136.

[56] Tibert, G., 2002, Deployable Tensegrity Structures for Space Applications, Citeseer.

[57] Mirletz, B. T., Park, I.-W., Flemons, T. E., Agogino, A. K., Quinn, R. D., and SunSpiral, V., 2014, "Design and Control of Modular Spine-like Tensegrity Structures," The 6th World Conference of the International Association for Structural Control and Monitoring (6WCSCM).

[58] Friesen, J., Pogue, A., Bewley, T., de Oliveira, M., Skelton, R., and Sunspiral, V., 2014, "DuCTT: A Tensegrity Robot for Exploring Duct Systems," 2014 IEEE International Conference on Robotics and Automation (ICRA), IEEE, pp. 4222–4228.

[59] Agogino, A., SunSpiral, V., and Atkinson, D., 2013, "Super Ball Bot-Structures for Planetary Landing and Exploration," NASA Innov. Adv. Concepts Program, Final Rep.

[60] SunSpiral, V., Agogino, A., and Atkinson, D., 2015, "Super Ball Bot-Structures for Planetary Landing and Exploration, NIAC Phase 2 Final Report."

[61] Zurek, R. W., and Smrekar, S. E., 2007, "An Overview of the Mars Reconnaissance Orbiter (MRO) Science Mission," J. Geophys. Res. Planets, **112**(E5).

[62] Saunders, R. S., Arvidson, R. E., Badhwar, G. D., Boynton, W. V, Christensen, P. R., Cucinotta, F. A., Feldman, W. C., Gibbs, R. G., Kloss, C., and Landano, M. R., 2004, "2001 Mars Odyssey Mission Summary," Space Sci. Rev., **110**(1), pp. 1–36.

[63] Chicarro, A., Martin, P., and Trautner, R., 2004, "The Mars Express Mission: an Overview," Mars Express: The Scientific Payload, pp. 3–13.

[64] Klein, H. P., 1979, "The Viking Mission and the Search for Life on Mars," Rev. Geophys., **17**(7), pp. 1655–1662.

[65] Smith, P. H., 2004, "The Phoenix Mission to Mars," Aerospace Conference, 2004. Proceedings. 2004 IEEE, IEEE.

[66] Manara, A., Pareschi, G., and Trinchieri, G., 2014, "Updates on the Project: Schiaparelli for ExoMars," Mem. della Soc. Astron. Ital. Suppl., **26**, p. 143.

[67] Muirhead, B. K., 2004, "Mars Rovers, Past and Future," Aerospace Conference, 2004. Proceedings. 2004 IEEE, IEEE.

[68] Nakamura, M., Imamura, T., Ishii, N., Abe, T., Satoh, T., Suzuki, M., Ueno, M., Yamazaki, A., Iwagami, N., and Watanabe, S., 2011, "Overview of Venus Orbiter, Akatsuki," Earth, Planets Sp., **63**(5), p. 443.

[69] Saunders, R. S., Pettengill, G. H., Arvidson, R. E., Sjogren, W. L., Johnson, W. T. K., and Pieri, L., 1990, "The Magellan Venus Radar Mapping Mission," J. Geophys. Res. Solid Earth, **95**(B6), pp. 8339–8355.

[70] Svedhem, H., Titov, D., Taylor, F., and Witasse, O., 2009, "Venus Express Mission," J. Geophys. Res. Planets, **114**(E5).

[71] Schmidt, G. R., Landis, G. A., and Oleson, S. R., 2011, "HERRO missions to Mars and Venus using Telerobotic Surface Exploration from Orbit," International Astronautical Congress, Cape Town, South Africa.

[72] Landis, G. A., Dyson, R., Oleson, S. J., Warner, J. D., Colozza, A. J., and Schmitz, P. C., 2011, "Venus Rover Design Study," Pap. AIAA, **7268**, pp. 26–29.

[73] Sagdeev, R. Z., Linkin, V. M., Blamont, J. E., and Preston, R. A., 1986, "The VEGA Venus Balloon Experiment," Science (80-.)., **231**, pp. 1407–1409.

[74] Hall, J. L., Fairbrother, D., Frederickson, T., Kerzhanovich, V. V, Said, M., Sandy, C., Ware, J., Willey, C., and Yavrouian, A. H., 2008, "Prototype Design and Testing of a Venus Long Duration, High Altitude Balloon," Adv. Sp. Res., **42**(10), pp. 1648–1655.

[75] Nishimura, J., Hinada, M., Yajima, N., and Fujii, M., 1994, "Venus Balloons at Low Altitudes," Adv. Sp. Res., **14**(2), pp. 61–71.

[76] de Jong, M. L., 2015, "Venus Altitude Cycling Balloon," Venus Science Priorities for Laboratory Measurements, p. 4030.

[77] DiCicco, A. G., Nock, K. T., and Powell, G. E., 1995, "Balloon Experiment at Venus (BEV)," 11th AIAA Lighter Than Air Systems Technology Conference, Clearwater Beach, Fl.(USA), pp. 144–154.

[78] Chassefière, E., Korablev, O., Imamura, T., Baines, K. H., Wilson, C. F., Titov, D. V, Aplin, K. L., Balint, T., Blamont, J. E., and Cochrane, C. G., 2009, "European Venus Explorer: An in-situ Mission to Venus using a Balloon Platform," Adv. Sp. Res., **44**(1), pp. 106–115.

[79] Glaze, L. S., Baker, C., Adams, M., Amato, M., Balint, T., Jones, A. L., Karpati, G., Marr, G., Tompkins, S., and Venkatapathy, E., 2010, "Venus Mobile Explorer (VME): a Mission Concept Study for the National Research Council Planetary Decacal Survey," 7th International Planetary Probe Workshop, Barcelona, Spain, June 14À18.

[80] Kerzhanovich, V. V, Hall, J. L., Yavrouian, A. H., and Cutts, J. A., 2005, Dual balloon concept for Lifting Payloads from the Surface of Venus, Pasadena, CA: Jet Propulsion Laboratory, National Aeronautics and Space Administration.

[81] Samuele, R., Lee, G., Sokol, D., Polidan, R., Griffin, K., Bolisay, L., Michi, Y., and Barnes, N., 2014, "A Unique Approach for Studying Venus's Atmosphere: Technology Development for the Venus Atmospheric Maneuverable Platform (VAMP)," AAS/Division for Planetary Sciences Meeting Abstracts.

[82] Landis, G. A., Colozza, A. J., and LaMarre, C. M., 2002, Atmospheric Flight on Venus, National Aeronautics and Space Administration, John H. Glenn Research Center at Lewis Field.

[83] Usui, M., Jacob, J. D., Smith, S. W., Scarborough, S., and Cadogan, D., 2005, "Second Generation Inflatable/rigidizable Wings for Low-density Flight Applications," Proc. 46th AIAA/ASME/ASCE/AHS/ASC Structures, Structural Dynamics & Materials Conference, pp. 18–

21.

[84] Landis, G., 2012, “A Landsailing Rover for Venus Mobility,” J. Br. Interplanet. Soc., **65**, pp. 373–377.

[85] Seiff, A., Kirk, D. B., Young, R. E., Blanchard, R. C., Findlay, J. T., Kelly, G. M., and Sommer, S. C., 1980, “Measurements of Thermal Structure and Thermal Contrasts in the Atmosphere of Venus and Related Dynamical Observations: Results from the Four Pioneer Venus Probes,” J. Geophys. Res. Sp. Phys., **85**(A13), pp. 7903–7933.

[86] Hajos, G. A., Jones, J. A., Behar, A., and Dodd, M., 2005, “An Overview of Wind-driven Rovers for Planetary Exploration,” Proceedings of the 43rd AIAA Aerospace Sciences Meeting and Exhibit, Reno, NV, Jan, pp. 10–13.

[87] Balint, T., Cutts, J., Bullock, M., Garvin, J., Gorevan, S., Hall, J., Hughes, P., Hunter, G., Khanna, S., and Kolawa, E., 2009, “Technologies for Future Venus Exploration,” White Pap. Submitt. to NRC Decad. Surv. Inn. Planets Sub-Panel.

[88] Hall, J. L., Bullock, M., Senske, D. A., Cutts, J. A., and Grammier, R., 2012, “Venus Flagship Mission Study, Final Report of the Venus Science and Technology Definition Team,” Jet Propuls. Lab [online database], URL[cited 15 May 1993].

[89] Dyson, R. W., Schmitz, P. G., Penswick, L. B., and Bruder, G. A., 2009, “Long-lived Venus Lander Conceptual Design: How to Keep it Cool,” 7th Int. Energy Convers. Eng. Conf., **4631**, pp. 2–5.

[90] Vorontsov, V. A., Lokhmatova, M. G., Martynov, M. B., Pichkhadze, K. M., Simonov, A. V, Khartov, V. V, Zasova, L. V, Zelenyi, L. M., and Korablev, O. I., 2011, “Prospective Spacecraft for Venus Research: Venera-D Design,” Sol. Syst. Res., **45**(7), pp. 710–714.

[91] Boll, N. J., Salazar, D., Stelter, C. J., Landis, G. A., and Colozza, A. J., 2015, “Venus High Temperature Atmospheric Dropsonde and Extreme-Environment Seismometer (HADES),” Acta Astronaut., **111**, pp. 146–159.

[92] Boiko, A. S., Kariagin, V. P., Kovtunenko, V. M., Kremnev, R. S., Pichkhadze, K. M., Ryzhov, Y. A., Terterashvili, A. V, Khololov, S. M., and Shteier, V. I., 1983, “Analysis of the Results of Areodynamic Investigations of the Descent Stages of Venera 13 and 14,” Kosm. Issled., **21**, pp. 379–385.

[93] Masursky, H., Eliason, E., Ford, P. G., McGill, G. E., Pettengill, G. H., Schaber, G. G., Schubert, G., Eliason, E., Ford, P. G., Loriot, G. B., Masursky, H., and McGill, G. E., 1980, "Pioneer Venus Radar Results, Altimetry, and Surface Properties," J. Geophys. Res. Sp. Phys., **85**(A13), pp. 8261–8270.

[94] Avduevskii, V. S., Godnev, A. G., Zakharov, Y. V, Petrosyan, L. V, Semenchenko, V. V, Suklyshkin, I. I., Uspenskii, G. R., and Cheremukhina, Z. P., 1983, "An Estimate of the Physical and Mechanical Characteristics of the Soil of Venus from Measurements of the Impact Overloads during the Landings of the Venera 13 and Venera 14 Automatic Interplanetary Stations," Kosm. Issled, **21**(3), pp. 331–339.

[95] Doengi, F., Dornier, D. A., Gmbh, S., Sa, A. T., Burnage, S. T., Cottard, H., and Roumeas, R., 1998, "Lander Shock-alleviation Techniques," ESA Bull., **93**, p. 2.

[96] Rogers, W. F., Center, M. S., Hyle, C. T., Foggatt, C. E., and Weber, B. D., 1972, Apollo Experience Report: Lunar Module Landing Gear Subsystem, National Aeronautics and Space Administration.

[97] Achenbach, E., 1972, "Experiments on the Flow Past Spheres at Very High Reynolds Numbers," J. Fluid Mech., **54**(3), pp. 565–575.

[98] Wieselsberger, C., 1922, Further Information on the Laws of Fluid Resistance, National Advisory Committee for Aeronautics.

[99] Hoerner, S., 1965, Fluid Dynamic Drag-theoretical, experimental and statistical information, Great Britain.

[100] Kariagin, V. P., Kremnev, R. S., Pichkhadze, K. M., Sklovskaia, A. I., and Iaroshevskii, V. A., 1977, "Investigation of Aerodynamics and Dynamics of Venera 9 and Venera 10 during Motion in the Atmosphere," Cosm. Res., **14**, pp. 741–747.

[101] Zoelly, R., 1915, "Ueber ein Knickungsproblem an der Kugelschale."

[102] Deka, L. J., Bartus, S. D., and Vaidya, U. K., 2008, "Damage Evolution and Energy Absorption of E-glass/Polypropylene Laminates Subjected to Ballistic Impact," J. Mater. Sci., **43**(13), pp. 4399–4410.

[103] Harvey, B., 2007, "The High Summer of Soviet Planetary Exploration, 1975–1986," Russ. Planet. Explor. Hist. Dev. Legacy, Prospect., pp. 171–237.

[104] Mitchell, D. P., 2003, “Plumbing the Atmosphere of Venus,” Ment. Landsc. [Online]. Available: http://mentallandscape.com/V_Lavochkin1.htm. [Accessed: 31-Jan-2017].

[105] Limaye, S., Smrekar, S., and Committee, V. E., 2009, “Venus White Paper for Planetary Sciences Decadal Survey Inner-Planets Panel Venus Exploration Goals, Objectives, Investigations, and Priorities.”

[106] Corfield, R., 2007, Lives of the Planets: A Natural History of the Solar System, Basic Books.

[107] Honeybee Robotics Ltd., 2013, “Motor for High Temperature Applications.”

[108] Rebello, N. S., Shoucair, F. S., and Palmour, J. W., 1996, “6H Silicon Carbide MOSFET Modelling for High Temperature Analogue Integrated Circuits (25-500° C),” IEE Proceedings-Circuits, Devices Syst., **143**(2), pp. 115–122.

[109] Akarvardar, K., Mercha, A., Simoen, E., Subramanian, V., Claeys, C., Gentil, P., and Cristoloveanu, S., 2007, “High-temperature Performance of State-of-the-art Triple-gate Transistors,” Microelectron. Reliab., **47**(12), pp. 2065–2069.

[110] Landis, G. A., and Harrison, R., 2010, “Batteries for Venus Surface Operation,” J. Propuls. Power, **26**(4), pp. 649–654.

[111] Hunter, G. W., Okojie, R. S., Krasowski, M. J., Beheim, G. M., Fralick, G. C., Wrbanek, J. D., Greenberg, P. S., and Xu, J., 2007, “Microsystems, Space Qualified Electronics and Mobile Sensor Platforms for Harsh Environment Applications and Planetary Exploration.”

[112] Salem, J. M., and Ha, D. S., 2016, “A High Temperature Active GaN-HEMT Down-conversion Mixer for Downhole Communications,” Addit. Pap. Present., **2016**(HiTEC), pp. 946–949.

[113] Salem, J. M., and Ha, D. S., 2016, “A Resistive GaN-HEMT Mixer for a Cable Modem Operable up to 250 oC for Downhole Communications,” to Appear J. Microelectron. Electron. Packag.

[114] Ehteshamuddin, M., Salem, J. M., and Ha, D. S., 2016, “Design of High Temperature Combline Band-pass Filters for Downhole Communications,” Addit. Pap. Present., **2016**(HiTEC), pp. 312–317.

[115] Cunningham, M. L., Ha, D. S., and Koh, K.-J., 2016, “A High Temperature Wideband Low Noise Amplifier for Downhole Applications,” Circuits and Systems (ISCAS), 2016 IEEE International Symposium on, IEEE, pp. 938–941.

[116] Schlumberger, “Surface Systems: Data Delivery,” Wireline Serv. Cat. ed Houston, Texas Schlumberger, pp. 12–13.

[117] Shampine, L. F., and Reichelt, M. W., 1997, “The Matlab ODE Suite,” SIAM J. Sci. Comput., **18**(1), pp. 1–22.

[118] Samareh, J. A., 2009, “A Multidisciplinary Tool for Systems Analysis of Planetary Entry, Descent, and Landing (SAPE).”

[119] Anderson, J. D., 2000, Hypersonic and High Temperature Gas Dynamics, Aiaa.

[120] Justus, C. G., and Braun, R. D., 2007, “Atmospheric Environments for Entry, Descent and Landing (EDL).”

[121] Petropoulos, B., 1988, “Physical Parameters of the Atmosphere of Venus,” Earth. Moon. Planets, **42**(1), pp. 29–40.

[122] Sutton, K., and Graves Jr, R. A., 1971, “A General Stagnation-point Convective Heating Equation for Arbitrary Gas Mixtures.”

[123] Scott, C. D., Ried, R. C., Maraia, R. J., Li, C.-P., and Derry, S. M., 1984, “An AOTV Aeroheating and Thermal Protection Study.”

[124] Tauber, M. E., Bowles, J. V, and Yang, L., 1989, “Atmospheric Environment During Maneuvering Descent from Martian Orbit,” J. Spacecr. Rockets, **26**(5), pp. 330–337.

[125] Park, C., and Ahn, H.-K., 1999, “Stagnation-point Heat Transfer Rates for Pioneer-Venus Probes,” J. Thermophys. heat Transf., **13**(1), pp. 33–41.

[126] Craig, S., and Lyne, J. E., 2005, “Parametric Study of Aerocapture for Missions to Venus,” J. Spacecr. Rockets, **42**(6), pp. 1035–1038.

[127] Tauber, M. E., Palmer, G. E., and Prabhu, D. K., 2012, “Stagnation Point Radiative Heating Relations for Venus Entry.”

[128] Tibert, A. G., and Pellegrino, S., 2011, “Review of Form-finding Methods for Tensegrity Structures,” Int. J. Sp. Struct., **26**(3), pp. 241–255.

[129] Schek, H.-J., 1974, “The Force Density Method for Form Finding and Computation of General Networks,” Comput. Methods Appl. Mech. Eng., **3**(1), pp. 115–134.

[130] Zhang, J. Y., and Ohsaki, M., 2006, "Adaptive Force Density Method for Form-Finding Problem of Tensegrity Structures," Int. J. Solids Struct., **43**(18), pp. 5658–5673.

[131] Guest, S. D., 2010, "The Stiffness of Tensegrity Structures," IMA J. Appl. Math., **76**(1), pp. 57–66.

[132] Tran, H. C., and Lee, J., 2010, "Advanced Form-Finding of Tensegrity Structures," Comput. Struct., **88**(3), pp. 237–246.

[133] Pellegrino, S., 1986, "Mechanics of Kinematically Indeterminate Structures."

[134] The Mathworks, 2015, "Matlab Optimization Toolbox User's Guide."

[135] United Launch Alliance, 2010, "Atlas V Launch Services User's Guide," Lockheed Martin Commer. Launch Serv.

[136] Furuya, H., 1992, "Concept of Deployable Tensegrity Structures in Space Application," Int. J. Sp. Struct., **7**(2), pp. 143–151.

[137] Ali, N. B. H., and Smith, I. F. C., 2010, "Dynamic Behavior and Vibration Control of a Tensegrity Structure," Int. J. Solids Struct., **47**(9), pp. 1285–1296.

[138] Bossens, F., de Callafon, R. A., and Skelton, R. E., 2007, "Modal Analysis of a Tensegrity Structure–an Experimental Study," Dep. Mech. Aerosp. Eng. Dyn. Syst. Control Group, Univ. California, San Diego, USA.

[139] Calladine, C. R., and Pellegrino, S., 1991, "First-order Infinitesimal Mechanisms," Int. J. Solids Struct., **27**(4), pp. 505–515.

[140] Heidaryan, E., Hatami, T., Rahimi, M., and Moghadasi, J., 2011, "Viscosity of Pure Carbon Dioxide at Supercritical Region: Measurement and Correlation Approach," J. Supercrit. Fluids, **56**(2), pp. 144–151.

[141] Horton, B., Song, Y., Feaster, J., and Bayandor, J., "Benchmarking of Computational Fluid Methodologies in Resolving Shear Driven Flow Fields," J. Fluids Eng.

[142] Rimoli, J. J., 2016, "On the Impact Tolerance of Tensegrity-based Planetary Landers," 57th AIAA/ASCE/AHS/ASC Structures, Structural Dynamics, and Materials Conference, p. 1511.

[143] Micro-Measurements, 2016, "Precision Strain Gages and Sensors Databook."

[144] PCB Piezotronics Inc., “Installation and Operating Manual Model 352C03.”

[145] Raspberry Pi Fondation, “Raspberry Pi Documentation” [Online]. Available: https://www.raspberrypi.org/documentation/. [Accessed: 20-Jul-2007].

[146] Analog Devices, 2014, “3-Axis, ±200 g Digital MEMS Accelerometer ADXL375.”

[147] O’Keefe, S. A., and Bose, D. M., 2010, “IRVE-II Post-Flight Trajectory Reconstruction.”

[148] Yount, B., Prabhu, D., Kruger, C., Gage, P., Squire, T., and Mockelman, J. A., 2013, “Structures and Mechanisms Design Concepts for Adaptive Deployable Entry Placement Technology,” AIAA Aerodynamic Decelerator Systems (ADS) Conference, AIAA-2013-1369.

[149] Caluwaerts, K., Despraz, J., Işçen, A., Sabelhaus, A. P., Bruce, J., Schrauwen, B., and SunSpiral, V., 2014, “Design and Control of Compliant Tensegrity Robots through Simulation and Hardware Validation,” J. R. Soc. Interface, **11**(98), p. 20140520.

[150] National Aeronautics and Space Administration, “NASA Tensegrity Robotics Toolkit (NTRT)” [Online]. Available: https://ti.arc.nasa.gov/tech/asr/intelligent-robotics/tensegrity/ntrt/. [Accessed: 21-Jul-2017].

[151] Grillner, S., 1985, “Neurobiological Bases of Rhythmic Motor Acts in Vertebrates,” Science (80-.)., **228**, pp. 143–150.

[152] Ijspeert, A. J., Crespi, A., Ryczko, D., and Cabelguen, J.-M., 2007, “From Swimming to Walking with a Salamander Robot Driven by a Spinal Sord Model,” Science (80-.)., **315**(5817), pp. 1416–1420.